

**PHOTOACOUSTIC COMPUTED TOMOGRAPHY IN BIOLOGICAL TISSUES:  
ALGORITHMS AND BREAST IMAGING**

A Dissertation

by

MINGHUA XU

Submitted to the Office of Graduate Studies of  
Texas A&M University  
in partial fulfillment of the requirements for the degree of  
DOCTOR OF PHILOSOPHY

August 2004

Major Subject: Biomedical Engineering

**PHOTOACOUSTIC COMPUTED TOMOGRAPHY IN BIOLOGICAL TISSUES:  
ALGORITHMS AND BREAST IMAGING**

A Dissertation

by

MINGHUA XU

Submitted to Texas A&M University  
in partial fulfillment of the requirements  
for the degree of

DOCTOR OF PHILOSOPHY

Approved as to style and content by:

---

Lihong Wang  
(Chair of Committee)

---

Hsin-i Wu  
(Member)

---

Gerard L. Côté  
(Member)

---

Peter Kuchment  
(Member)

---

William Hyman  
(Head of Department)

August 2004

Major Subject: Biomedical Engineering

## ABSTRACT

Photoacoustic Computed Tomography in Biological Tissues:

Algorithms and Breast Imaging. (August 2004)

Minghua Xu, B.S., Qingdao University of Oceanography;

M.S., Nanjing University

Chair of Advisory Committee: Dr. Lihong Wang

Photoacoustic computed tomography (PAT) has great potential for application in the biomedical field. It best combines the high contrast of electromagnetic absorption and the high resolution of ultrasonic waves in biological tissues.

In Chapter II, we present time-domain reconstruction algorithms for PAT. First, a formal reconstruction formula for arbitrary measurement geometry is presented. Then, we derive a universal and exact back-projection formula for three commonly used measurement geometries, including spherical, planar and cylindrical surfaces. We also find this back-projection formula can be extended to arbitrary measurement surfaces under certain conditions. A method to implement the back-projection algorithm is also given. Finally, numerical simulations are performed to demonstrate the performance of the back-projection formula.

In Chapter III, we present a theoretical analysis of the spatial resolution of PAT for the first time. The three common geometries as well as other general cases are investigated. The point-spread functions (PSF's) related to the bandwidth and the

sensing aperture of the detector are derived. Both the full-width-at-half-maximum of the PSF and the Rayleigh criterion are used to define the spatial resolution.

In Chapter IV, we first present a theoretical analysis of spatial sampling in the PA measurement for three common geometries. Then, based on the sampling theorem, we propose an optimal sampling strategy for the PA measurement. Optimal spatial sampling periods for different geometries are derived. The aliasing effects on the PAT images are also discussed. Finally, we conduct numerical simulations to test the proposed optimal sampling strategy and also to demonstrate how the aliasing related to spatially discrete sampling affects the PAT image.

In Chapter V, we first describe a prototype of the RF-induced PAT imaging system that we have built. Then, we present experiments of phantom samples as well as a preliminary study of breast imaging for cancer detection.

To my family.

## **ACKNOWLEDGEMENTS**

I would like to express my appreciation to Dr. Lihong Wang for his help and guidance throughout all my years of research and life as a graduate student.

I would like to express my gratitude also to my advisory committee: Dr. Hsin-i Wu, Dr. Gerard L. Coté, and Dr. Peter Kuchment.

Thanks to Geng Ku, Shuliang Jiao, and all the members of Dr. Wang's Optical Imaging Laboratory, for their help.

## TABLE OF CONTENTS

	Page
ABSTRACT .....	iii
DEDICATION .....	v
ACKNOWLEDGEMENTS .....	vi
TABLE OF CONTENTS .....	vii
LIST OF FIGURES .....	x
 CHAPTER	
I INTRODUCTION .....	1
A. Overview .....	1
B. Photoacoustic generation theory .....	2
C. Absorption contrast and penetration .....	5
1. RF properties .....	6
2. Optical properties .....	7
3. Ultrasonic properties .....	8
4. Safety .....	9
D. Photoacoustic tomography .....	11
E. Outline .....	15
II RECONSTRUCTION ALGORITHMS .....	16
A. Introduction .....	16
B. Fourier-domain algorithms .....	17
1. Spherical geometry .....	19
2. Planar geometry .....	21
3. Cylindrical geometry .....	25
C. Universal time-domain algorithm .....	26
1. Back-projection formula .....	26
2. Implementation method .....	35
3. Numerical simulations .....	38
(a). Spherical geometry .....	40
(b). Planar geometry .....	41
(c). Cylindrical geometry .....	41
(d). Low resolution .....	43
D. Summary .....	44

CHAPTER	Page
III	SPATIAL RESOLUTION .....45
	A. Introduction .....45
	B. Bandwidth-limited PSF .....46
	1. Space-invariance .....46
	2. Diffraction-limited resolution .....50
	C. Effect of detector aperture .....53
	1. Spherical geometry .....55
	(a). Special spherical aperture .....58
	(b). Small flat aperture .....59
	2. Planar geometry .....63
	3. Cylindrical geometry .....65
	(a). Special cylindrical aperture .....65
	(b). Small rectangular aperture .....68
	4. Combined effects .....71
	D. Summary .....73
IV	SAMPLING STRATEGY .....75
	A. Introduction .....75
	B. Optimal sampling strategy .....77
	1. Planar geometry .....79
	2. Cylindrical geometry .....82
	3. Spherical geometry .....85
	4. Summary and discussions .....89
	C. Aliasing artifacts .....92
	1. Linear scan .....92
	2. Circular scan .....94
	D. Summary .....97
V	BREAST IMAGING .....98
	A. Introduction .....98
	B. Measurement method .....102
	C. Phantom experiments .....103
	1. Image contrast .....103
	2. Spatial resolution .....105
	3. Images of thick samples .....108
	D. Breast cancer imaging .....110
	E. Summary .....113
VI	SUMMARY AND CONCLUSIONS .....114



	Page
REFERENCES .....	116
VITA .....	124

## LIST OF FIGURES

	Page
FIG. 2.1. (a) In the measurement, an ultrasonic detector at position $\mathbf{r}_0$ on a surface $S_0$ receives PA signals emitted from source $p_0(\mathbf{r}')$ . In the reconstruction, a quantity related to the measurement at position $\mathbf{r}_0$ projects backward on a spherical surface with respect to position $\mathbf{r}_0$ . (b) In the planar geometry, assume there is another surface $S'_0$ at infinity and that the combination of $S_0$ and $S'_0$ encloses the source inside. ....	18
FIG. 2.2. Schematic of measurement geometries: (a) spherical geometry, (b) planar geometry, and (c) cylindrical geometry. ....	19
FIG. 2.3. Original sample: (a) a cross-sectional image, (b) a profile along the horizontal center line. ....	38
FIG. 2.4. Reconstructed image from spherical measurement geometry using 3600 detector positions with high cutoff frequency 4 MHz: (a) a cross-sectional image at the $z = 12$ mm plane, (b) comparison of the original and reconstructed absorption profiles along the horizontal center line. ....	40
FIG. 2.5. Reconstructed image from planar measurement geometry using 3600 detector positions with high cutoff frequency 4 MHz: (a) a cross-sectional image at the $z = 30$ mm plane, (b) comparison of the original and reconstructed absorption profiles along the horizontal center line. ....	41
FIG. 2.6. Reconstructed image from cylindrical geometry using 3600 detector positions with high cutoff frequency 4 MHz: (a) a cross-sectional image at the $z = 0$ mm plane, (b) comparison of the original and reconstructed absorption profiles along the horizontal center line. ....	42
FIG. 2.7. Reconstructed image from spherical measurement geometry using 3600 detector positions with high cutoff frequency 1.5 MHz: (a) a cross-sectional image at the $z = 12$ mm plane, (b) comparison of the original and reconstructed absorption profiles along the horizontal center line. ....	43
FIG. 3.1. Diagram of the measurement geometry: a measurement surface $S_1$ completely encloses another measurement surface $S$ ; there is a point source $A$ at $\mathbf{r}_a$ inside $S$ ; $R$ is the distance between an arbitrary point at $\mathbf{r}$ and the point source $A$ ; $\mathbf{r}_0$ and $\mathbf{r}_1$ point to an detection element on the surface $S$ and $S_1$ , respectively. ....	47

- FIG. 3.2. An example of the PSF as a result of the bandwidth (0, 4 MHz): (a) a grayscale view and (b) a profile through the point source. .... 50
- FIG. 3.3. Superposition of two PSF's at the Rayleigh criterion. Dash line: normalized PSF expressed by  $3j_1(\pi x)/(\pi x)$ . Solid line: superposition of two PSF's. .... 51
- FIG. 3.4. Comparison of the PSF's with different bandwidths: dash-line, (0, 2 MHz); solid-line, (0, 4 MHz); dot-line, (2 MHz, 4 MHz); and dot-dash-line, 4 MHz. .... 52
- FIG. 3.5. Diagram of the detector surface  $\mathbf{r}'$  with origin  $o'$ . The vector  $\mathbf{r}_0$  represents the center of detector  $o'$  in the recording geometry with origin  $o$ . The vector  $\mathbf{r}'_0$  points an element of the detector aperture. .... 54
- FIG. 3.6. (a) Diagram of the spherical measurement geometry:  $\theta'$  is the angle between  $\mathbf{r}_0$  and  $\mathbf{r}'_0$ ;  $dl'$  is an integral element on the detector surface;  $\Theta$  is the angle of the radius of the detector aperture to the measurement geometry origin  $o$ ; the extension of the PSF at point  $A$  is indicated; other denotations of the symbols are the same as in Figs. 3.1 and 3.3. (b) Perspective view of the lateral extension of the PSF's of all the point sources along a radial axis in the spherical measurement geometry. .... 55
- FIG. 3.7. (a) Diagram of the planar measurement geometry:  $P$  is the radius of the detector aperture; the extension of the PSF at point  $A$  is indicated; other denotations of the symbols are the same as in Figs. 3.1 and 3.5; (b) Perspective view of the lateral extension of the PSF's of all the point sources along a line parallel with the  $z$ -axis in the planar measurement geometry. .... 64
- FIG. 3.8. (a) Diagram of the cylindrical geometry:  $\phi'$  is the difference between the polar angles of  $\mathbf{r}_0$  and  $\mathbf{r}'_0$ ;  $\rho'$  and  $z'$  are the projections of  $\mathbf{r}'$  in the  $x$ - $y$  plane and the  $z$ -axis, respectively;  $Z$  is the half width of the detector aperture along the  $z$ -axis and  $\Phi$  is the half angle of the width of the detector aperture parallel with the  $x$ - $y$  plane to the center of the measurement geometry; the extension of the PSF at point  $A$  is indicated; other denotations of the symbols are the same as in Figs. 5.1 and 5.3. (b) Perspective view of the lateral extension of the PSF's of all the point sources along a radial axis in the cylindrical recording geometry. .... 66

FIG. 3.9. An example of the PSF due to the detector aperture: (a) a grayscale view and (b) a lateral profile through the point source. ....	73
FIG. 4.1. Solid line: function $2J_1(\xi)/\xi$ ; Dash line: sinc function $\sin(\xi)/\xi$ . ....	81
FIG. 4.2. Pressure profiles along the line ( $y = 0, z = 10$ mm) that is parallel to the $x$ -axis. Vertical axis is the amplitude in arbitrary unit. Horizontal axis is in mm. Curve 1: original profile. Curves 2 to 6: reconstructions from the measurements with sampling periods, including 4 mm, 2 mm, 1 mm, 0.5 mm and 0.4 mm, respectively. ....	93
FIG. 4.3. Pressure profiles. Curves 1 to 3: reconstructions with sampling periods, including $\pi$ mm, $\pi/2$ mm, and $\pi/4$ mm, respectively, along the line ( $x = 8$ mm, $z = 0$ ), when the absorber is at ( $x = 8$ mm, $y = z = 0$ ). Curves 4 to 6: reconstructions with sampling periods, including $\pi$ mm, $\pi/2$ mm, and $\pi/4$ mm, respectively, along the line ( $x = 16$ mm, $z = 0$ ), when the absorber is at ( $x = 16$ mm, $y = z = 0$ ). ....	95
FIG. 5.1. Properties of human breast tissues. ....	99
FIG. 5.2. Penetration depths versus frequencies. ....	101
FIG. 5.3 Diagram of experimental setup. ....	103
FIG. 5.4. (a) Photograph of the cross-section of a tissue sample; (b) Reconstructed image. ....	104
FIG. 5.5. (a) Photograph of the cross-section of a tissue sample; (b) Side-view of the sample buried 1-cm deep inside a fat base; (c) Reconstructed image. ....	106
FIG. 5.6. (a) Photoacoustic image of a thin wire; (b) Profile across the wire. ....	107
FIG. 5.7. (a) Diagram of the measurement; (b) Cross section of the tissue sample; (c) Reconstructed image. ....	109
FIG. 5.8. (a) Pre-operative mammogram showing suspicious density in the breast, which was taken with standard compression. (b) The mastectomy specimen placed in a plastic cylindrical container with a diameter of 10 cm (c) Radiograph of the mastectomy specimen in the container. (d) Sonogram of the specimen in the container. (e) Photoacoustic image of the specimen in the container. The rectangle marks the wave-guide aperture. The tumor is marked by a circle in (a), (c) and (e) and by two white lines in (d). ....	112

## CHAPTER I

### INTRODUCTION

#### A. Overview

The photoacoustic (PA) effect refers to the generation of acoustic waves by electromagnetic (EM) waves. Although this effect was first reported in 1880 [1], it did not attract much attention until the 1970s when lasers burst onto the scene. Since then, a great deal of experimental and theoretical work on photoacoustics in various branches of physics, chemistry, biology, engineering, and medicine has been reported in the literature [2-12].

In the past decade, biomedical photoacoustics, particularly PA imaging using pulsed EM excitation, has undergone tremendous growth [13-16]. Non-ionizing EM waves such as optical or microwave/radio frequency (RF) waves with low radiation are often utilized for PA generation in biomedical applications. For simplicity, we will use RF to represent either microwave or RF waves or both throughout the text.

The motivation of PA imaging using pulsed EM excitation is to combine the resolution advantages of ultrasound and the contrast advantages of the EM properties in the optical and RF regions. Pure ultrasound imaging can provide better resolution than optical imaging in depths greater than ~1 mm, since ultrasound scattering is 2–3 orders of magnitude weaker than optical scattering in biological tissues [17,18]. However,

---

This dissertation follows the style of Physics Review E.

ultrasound imaging is based on the detection of mechanical properties in biological tissues, so it has weak contrast for early stage tumors. Moreover, it cannot image either oxygen saturation or the concentration of hemoglobin. Likewise, pure RF imaging cannot provide good spatial resolution because of its long wavelength [19]. Utilizing operating frequencies in the range of 500–900 MHz, RF imaging can only provide a spatial resolution of  $\sim 1$  cm [20]. The spatial resolution of PA imaging, as well as the maximum imaging depth, is scaleable with the detected ultrasonic frequency range. For example, PA signals in the MHz range can provide millimeter spatial resolution that is limited by the PA wavelength, since the velocity of sound in soft tissues is  $\sim 1.5$  mm/ $\mu$ s.

### **B. Photoacoustic generation theory**

In our study of photoacoustic imaging of biological tissues, we focus mainly on the thermoelastic mechanism of PA generation with low radiation of pulsed optical or RF sources, in which a sound or stress wave is produced as a consequence of the thermoelastic expansion that is induced by a slight temperature rise, typically less than  $0.01$  °C, as a result of the energy deposition inside the biological tissue through the absorption of the incident EM energy. The thermoelastic mechanism has special features that make PA techniques amenable for biomedical applications. First, it does not break or change the properties of the biological tissue under study. Secondly, only non-ionizing radiation is used, unlike in x-ray imaging or positron-emission tomography (PET). The non-destructive (non-invasive) and non-ionizing nature of PA techniques makes them ideal for *in vivo* applications. Thirdly, the relationships between PA signals

and the physical parameters of biological tissues are well defined. This advantage permits the quantification of various physiological parameters such as the oxygenation of hemoglobin.

In soft tissues, the thermal diffusion effect on the PA signal is usually negligible since the EM energy is deposited in the sample within a relatively short time. Therefore, the efficiency of PA generation is high. Upon the absorption of the pulse energy, the thermal diffusion during the pulse period can be estimated by the following thermal diffusion length [5]:

$$\delta_T = 2\sqrt{D_T\tau_p} , \quad (1.1)$$

where  $\tau_p$  is the pulse duration and  $D_T$  is the thermal diffusivity of the sample. Thermal diffusivity for most soft tissues is  $D_T \sim 1.4 \times 10^{-3} \text{ cm}^2 / \text{s}$  [17]. For example, for an RF pulse of  $\tau_p = 0.5 \mu\text{s}$ ,  $\delta_T \approx 0.5 \mu\text{m}$ , which is typically much less than the spatial resolution of most PA imaging systems and the characteristic heating length  $L_p$  defined by the penetration depth of the EM wave or the size of the absorbing structure.

Photoacoustic waves, like all other acoustic/ultrasonic waves, propagate in three-dimensional (3D) space. For simplicity, the inhomogeneity of acoustic speed in soft tissues is usually neglected in calculating acoustic wave propagation. The speed of sound is relatively constant at  $1.5 \text{ mm}/\mu\text{s}$  with a small variation of less than 5% in most soft tissues [17,21]. If acoustic heterogeneity becomes important, we can resort to a pure acoustic technique, such as ultrasound pulse-echo imaging or ultrasound tomography, to map out the acoustic inhomogeneity.

Here, we review some fundamental equations. In response to a heat source  $H(\mathbf{r}, t)$ , without considering thermal diffusion and kinematical viscosity, the pressure  $p(\mathbf{r}, t)$  at position  $\mathbf{r}$  and time  $t$  in an acoustically homogeneous liquid-like medium obeys the following wave equation [5,6,12,22]:

$$\nabla^2 p(\mathbf{r}, t) - \frac{1}{c^2} \frac{\partial^2}{\partial t^2} p(\mathbf{r}, t) = -\frac{\beta}{C_p} \frac{\partial}{\partial t} H(\mathbf{r}, t), \quad (1.2)$$

where  $H(\mathbf{r}, t)$  is the heating function defined as the thermal energy deposited by the EM radiation per time per volume ( $c$ —the speed of sound;  $\beta$ —the isobaric volume expansion coefficient; and  $C_p$ —the specific heat).

The solution, which is based on Green's function, can be found in the literature of physics or mathematics [23–26]. In general, the solution of Eq. (1.2) in the time domain can be expressed by

$$p(\mathbf{r}, t) = \frac{\beta}{4\pi C_p} \iiint \frac{d^3 r'}{|\mathbf{r} - \mathbf{r}'|} \left. \frac{\partial H(\mathbf{r}', t')}{\partial t'} \right|_{t' = t - \frac{|\mathbf{r} - \mathbf{r}'|}{c}}. \quad (1.3)$$

The heating function can be written as the product of a spatial absorption function and a temporal illumination function:

$$H(\mathbf{r}, t) = A(\mathbf{r})I(t). \quad (1.4)$$

Particularly, if  $I(t) = \delta(t)$ , the initial photoacoustic pressure at position  $\mathbf{r}$  equals  $p_0(\mathbf{r}) = \Gamma(\mathbf{r})A(\mathbf{r})$  [27], where  $\Gamma(\mathbf{r})$  is the Grüneisen parameter equal to  $c^2\beta/C_p$ .

In this thesis, we define the Fourier transform pair on variable  $\bar{t} = ct$  as:



$$\tilde{F}(k) = \int_{-\infty}^{+\infty} F(\bar{t}) \exp(ik\bar{t}) d\bar{t}, \quad (1.5)$$

and

$$F(\bar{t}) = (1/2\pi) \int_{-\infty}^{+\infty} \tilde{F}(k) \exp(-ik\bar{t}) dk, \quad (1.6)$$

where  $k = \omega/c$  and  $\omega$  is an angular frequency and equal to  $2\pi f$ .

Thus, Eq. (1.2) can be rewritten as:

$$(\nabla^2 + k^2) \tilde{p}(\mathbf{r}, k) = ikp_0(\mathbf{r}), \quad (1.7)$$

where  $\tilde{p}(\mathbf{r}, k)$  is the Fourier transform of  $p(\mathbf{r}, \bar{t})$ . Based on Green's theorem, the spectrum  $\tilde{p}(\mathbf{r}_0, k)$  of the pressure  $p(\mathbf{r}_0, \bar{t})$  detected at  $\mathbf{r}_0$  can be written in the frequency domain [23-26] as:

$$\tilde{p}(\mathbf{r}_0, k) = -ik \iiint_{V'} d^3r' \tilde{G}_k^{(out)}(\mathbf{r}', \mathbf{r}_0) p_0(\mathbf{r}'), \quad (1.8)$$

where  $V'$  is the volume of the source  $p_0(\mathbf{r}')$ ; and  $\tilde{G}_k^{(out)}(\mathbf{r}, \mathbf{r}_0)$  is a Green's function:

$$\tilde{G}_k^{(out)}(\mathbf{r}', \mathbf{r}_0) = \frac{\exp(ik|\mathbf{r}' - \mathbf{r}_0|)}{4\pi|\mathbf{r}' - \mathbf{r}_0|}, \quad (1.9)$$

which corresponds to an outgoing wave.

### C. Absorption contrast and penetration

In biomedical applications, non-ionizing EM energy in the optical (from visible to near-IR) and RF regions is often utilized for PA excitation. This is not only because the EM waves in this region are safe for human use, but also because they provide the

high contrast and adequate penetration depths in biological tissues that are required for various applications [17,18,28,29].

No other EM spectrum seems practical for PA generation in deep tissues. For example, T-rays that lie between the above two EM spectra do not penetrate biological tissue well due to water-dominated absorption. In the short-wavelength spectrum below the visible region, such as ultraviolet, radiation has high photon energy and, therefore, is harmful to human subjects. On the other hand, if the RF frequency is too low, the absorption is too weak for efficient PA generation.

### ***1. RF properties***

The RF properties of biological tissues are related to the physiological nature of their electrical properties. The electrical properties [29] can be described by the complex permittivity  $\epsilon^* = \epsilon' \epsilon_0 + \sigma / (j\omega)$  or complex conductivity  $\sigma^* = \sigma + j\omega \epsilon' \epsilon_0$ , where  $\sigma$  is the conductivity (S/m);  $\epsilon'$  is the relative permittivity (dimensionless);  $\epsilon_0 = 8.85 \text{ pF/m}$  (permittivity of vacuum) and  $\omega$  is the angular frequency. This formulation assumes that the dielectric properties of the tissue are linear. In terms of these properties, the wavelength  $\lambda$  of an EM wave in tissue is  $\lambda = c_0 / (f \text{Re} \sqrt{\epsilon^* / \epsilon_0})$  and the 1/e penetration depth of the field is  $\delta = c_0 / (2\pi f \text{Im} \sqrt{\epsilon^* / \epsilon_0})$ , where Re and Im represent the real and imaginary parts, respectively, and  $c_0$  is the velocity of the RF wave *in vacuo*.

In the RF region, such as 0.3–3 GHz, EM waves can readily be transmitted through, absorbed or reflected by biological tissue boundaries in varying degrees

depending on the body size, tissue properties and EM frequency. However, little scattering occurs in tissues in this frequency range [28]. The penetration depth is equal to the reciprocal of the absorption coefficient when scattering and diffraction are ignored. For example, the absorption coefficients in fat (low water content) and muscle (high water content) are about 0.1 and 1  $\text{cm}^{-1}$  at 3 GHz, respectively, and about 0.03 and 0.3  $\text{cm}^{-1}$  at 300 MHz, respectively.

The two properties that have the strongest effect on the degree of RF absorption are ionic conductivity and the vibration of the dipolar molecules of water and proteins in biological tissues [28]. A small increase in ionic conductivity or water content in tissue can produce a significant increase in RF absorption. It is believed that the ionic conductivity and/or water content in cancerous tissue are higher than in normal tissue due to an increased concentration of blood and proteins. These increases are the result of angiogenesis in rapidly growing tumors.

## ***2. Optical properties***

The optical properties of biological tissue in the visible (400 to 700 nm) and near-IR (700 to 1400 nm) region of the EM spectrum are related to the molecular constituents of tissues and their electronic and/or vibrational structures. They are intrinsically sensitive to tissue abnormalities and functions. Optical scattering properties reveal architectural changes in biological tissue at the cellular and sub-cellular levels, whereas optical absorption properties can be used to quantify angiogenesis and hyper-

metabolism. The absorption coefficients of visible to near-IR light vary between  $\sim 0.1$  to  $\sim 10 \text{ cm}^{-1}$  in biological tissues [18]. Contrast agents, such as indocyanine green, can also be used to increase optical absorption.

Light scattering is quite strong in biological tissues. The reduced or effective scattering coefficient is described by  $\mu'_s = \mu_s(1 - g)$ , where  $\mu_s$  and  $g$  are the scattering coefficient and the anisotropy factor, respectively. Typically  $\mu_s \sim 100 \text{ cm}^{-1}$  and  $g \sim 0.9$  in the visible to near-IR region [18]. When scattering is much stronger than absorption, the effective penetration depth  $\delta$  of light equals the reciprocal of the effective attenuation coefficient  $\mu_{eff} = \sqrt{3\mu_a(\mu_a + \mu'_s)}$ ; otherwise, the relationship is more complicated [18]. There are two optical windows that allow light to penetrate relatively deep into biological tissues. The main one lies between 600 and 1300 nm and the second one between 1600 to 1850 nm (in the mid-IR range from 1400 to 3000 nm) [17]. The first window allows deeper penetration than the second one, because the second one is bounded by two water absorption bands.

### ***3. Ultrasonic properties***

In the low MHz frequency range ( $< 10 \text{ MHz}$ ), ultrasound has the properties of low scattering and deep penetration in soft tissues [17,21]. The total attenuation results from the combined losses due to absorption and scattering, while the scatter component accounts for about 10–15% of the total attenuation. The attenuation of all tissues is dependent upon temperature, a variation of which is also frequency dependent. The frequency dependency of ultrasonic attenuation and absorption can be represented by the

expression  $\mu = af^b$ , where  $a$ ,  $b$  are constants and  $f$  is the frequency of ultrasound [17]. A mean value of ultrasound attenuation equals  $\sim 0.6 \text{ dB cm}^{-1} \text{ MHz}^{-1}$  for soft tissues [21]. The attenuation increases with the frequency, so the distance over which useful levels of energy can be propagated becomes less as the frequency is increased. Typically, 3 MHz might be the maximum frequency for a 150-mm penetration [21]. However, in the high MHz frequency range, both scattering and attenuation are increased tremendously, while penetration depth is markedly decreased.

#### ***4. Safety***

For safety reasons, human exposure to EM radiation must be limited. One of the important technical parameters for safety is the so-called maximum permissible exposure (MPE), which is defined as the level of EM radiation to which a person may be exposed without hazardous effects or biological changes. MPE levels are determined as a function of EM wavelength (or frequency), exposure time and pulse repetition. The MPE is usually expressed in terms of either radiant exposure in  $\text{J/cm}^2$  or irradiance in  $\text{W/cm}^2$  for a given wavelength and exposure duration. Exposure to EM energy above the MPE can potentially result in tissue damage. Generally, the longer the wavelength, the higher the MPE; and the longer the exposure time, the lower the MPE.

The IEEE standard (Std C95.1, 1999 edition) defines MPE levels with respect to human exposure to RF fields from 3 kHz to 300 GHz [30]. For an RF radiation in the range of 0.3–3 GHz in a controlled environment,  $\text{MPE} = f / 300 \text{ mW/cm}^2$ , where  $f$  is the frequency in MHz. For exposure to pulsed RF fields with pulse durations of less than

100 ms, the MPE in terms of peak power density for a single pulse is given by the MPE multiplied by the averaging-time in seconds and divided by 5 times the pulse-width in seconds, i.e.,  $\text{Peak-MPE} = \text{MPE} \times \text{Averaging-time} / (5 \times \text{Pulse-width})$ , where the averaging-time for 0.3–3 GHz is 6 min that is an appropriate time period over which exposure is averaged for purposes of determining compliance with an MPE. If there are more than five pulses during any period equal to the averaging-time, the Peak-MPE per pulse should be divided by the pulse repetition frequency (PRF: N pulses per second), i.e.,  $\text{Peak-MPE/Pulse} = \text{Peak-MPE}/N$ . For example, for an RF wave at  $f = 3$  GHz,  $\text{MPE} = 10 \text{ mW/cm}^2$ . If the pulse duration is  $0.5 \text{ }\mu\text{s}$ ,  $\text{Peak-MPE} = 10 \times 360 / (5 \times 0.5 \times 10^{-6}) \text{ mW/cm}^2 = 1.44 \text{ MW/cm}^2$ . If the PRF is  $N = 50 \text{ /s}$ ,  $\text{Peak-MPE/Pulse} = 1.44/50 = 28.8 \text{ KW/cm}^2$ , and the corresponding pulse energy density is  $\text{Peak-MPE/Pulse} \times \text{Pulse-width} = 28.8 \text{ KW/cm}^2 \times 0.5 \text{ }\mu\text{s} = 14.4 \text{ mJ/cm}^2$ .

The American national standard (Z136.1-2000) defines MPE levels for specific laser wavelengths (180nm–1mm) and exposure durations [31]. For example, in the case of skin exposure to a laser beam in the visible and NIR range (400–1400nm),  $\text{MPE} = 200C_A \text{ mW/cm}^2$  for an exposure duration (T) of 10–30000s,  $1.1C_A T^{0.25} \text{ J/cm}^2$  for an exposure duration of  $10^{-7}$ –10s, or  $20C_A \text{ mJ/cm}^2$  for a single short pulse with a duration of 1–100 ns, respectively, where  $C_A = 1.0$  in 400–700 nm,  $10^{2(\lambda-0.7)}$  in 700–1050nm, and 5.0 in 1050–1400nm, respectively;  $\lambda$  is the wavelength. For example, for a 632.8-nm laser,  $\text{MPE} = 20 \text{ mW/cm}^2$  for a CW source, and  $\text{MPE}_{\text{SP}} = 200 \text{ mJ/cm}^2$  for a single pulse with a duration of 10 ns. However, to determine the applicable MPE for an exposure to a repetitive-pulse laser, the wavelength, the PRF, the duration of a single pulse, the

duration of any pulse groups ( $T$ ) and the duration of a complete exposure ( $T_{\max}$ ) must be known. The appropriate MPE/Pulse is the value that indicates the greatest hazard from testing the following three rules. Rule 1, Single-pulse limit: The  $MPE_{SP}$  is limited for any single pulse during the exposure. Rule 2, Average-power limit: The MPE is limited to the MPE for the duration of all pulse trains,  $T$ , divided by the number of pulses,  $n$ , during  $T$ , for all exposure durations up to  $T_{\max}$ . Rule 3, Repetitive-pulse limit: The MPE is limited to  $MPE_{SP}$  multiplied by a correction factor,  $n^{-0.25}$ , where  $n$  is the number of pulses that occur during the exposure duration  $T_{\max}$ . As an example, let us determine the MPE for a 632.8-nm laser that has a pulse width of 10 ns and a PRF of 10 Hz. According to rule 1,  $MPE_{SP} = 200 \text{ mJ/cm}^2$ . According to rule 2, assume an exposure duration of  $T = 10 \text{ s}$ . The MPE for a 10-s exposure is  $MPE = 1.1 \times 10^{0.25} = 2 \text{ J/cm}^2$ . Then, the MPE/Pulse based on a 10-s exposure is  $MPE/Pulse = 2/100 \text{ J/cm}^2 = 20 \text{ mJ/cm}^2$ , since the total number of pulses in a 10-s interval is  $n = PRF \times 10 = 10 \times 10 = 100$  pulses. According to rule 3,  $MPE/Pulse = n^{-0.25} \times MPE_{SP} = 100^{-0.25} \times 200 \text{ mJ/cm}^2 = 63 \text{ mJ/cm}^2$ . Rule 2 provides the MPE/Pulse since it is the most conservative (i.e., lowest value) calculation.

#### **D. Photoacoustic tomography**

Photoacoustic tomography (PAT) is a novel imaging modality, which uses all of the PA signals measured at different positions around the sample. As discussed earlier, with this technique, it is assumed that, following a short pulse of EM illumination, a spatial distribution of acoustic pressure inside the tissue is simultaneously excited by thermoelastic expansion that acts as a source for the acoustic response. The intensity of

the acoustic pressure is strongly related to the locally absorbed EM energy. The acoustic waves from the initial acoustic source propagate toward the surface of the tissue with various time delays. Wideband acoustic transducers are placed around the tissue to intercept the outgoing acoustic waves, which are further used to inversely recover the initial acoustic source.

From a physical point of view, PAT represents an inverse source problem analogous to PET, except that PAT is based on diffraction “optics” due to the diffraction of the ultrasonic wave and PET is based on geometric “optics” due to the straight-line propagation of the  $\gamma$ -rays. Therefore, PAT belongs to the field of diffraction tomography. Since acoustic waves do not travel along straight lines, the projections are not line integrals, which are in contrast to those in straight-ray tomography such as PET and x-ray CT. Nevertheless, many imaging concepts and mathematical techniques for other imaging modalities, such as ultrasonic, x-ray and optical tomography, can be borrowed for PAT applications.

A number of groups worldwide have made significant contributions to this topic. Two methods are often used: scanning PAT with focused ultrasonic transducers and computed tomography with unfocused ultrasonic transducers that have a small aperture. The latter requires computer-based reconstruction. PAT is also called optoacoustic tomography (OAT) or thermoacoustic CT (TCT). The former refers particularly to the use of light as the excitation source, while the term “thermoacoustic” emphasizes the thermal expansion mechanism in PA generation, in which the heating may be induced by various excitation sources such as high-power ultrasound rather than EM waves.



A few researchers [32-35] have demonstrated PA imaging by scanning with a focused ultrasonic transducer, which is actually analogous to the B-mode scan in ultrasonography. Each detected time-resolved signal is converted into a 1D image along the acoustic axis of the transducer, analogous to an ultrasonic A-line or A-scan. Cross-sectional images are formed by combining the 1D images acquired from the same plane. The axial resolution along the acoustic axis is dependent on both the width of the radiation pulse and the width of the impulse response of the transducer. The lateral resolution is determined by the focal diameter of the ultrasonic transducer.

A majority of the more recent works have focused on reconstruction-based PAT. Several approximated reconstruction algorithms have been demonstrated. Among them, Kruger *et al.* [36-38] suggested a filtered back-projection algorithm under circular or spherical measurement geometries, analogous to that used in x-ray computed tomography; Liu [39] presented an approach based on matrix inversion; Hoelen and de Mul *et al.* [40,41] constructed a time-domain delay-and-sum focused beam-forming algorithm to locate the PA sources in a sample in the planar scan geometry; Köstli *et al.* [42] reported an image reconstruction by back-projection of detected two-dimensional (2D) pressure distributions; Paltauf *et al.* [43] studied an iterative reconstruction algorithm to minimize the error between the measured signals and signals calculated from the reconstructed image; and Zhulina [44] explored an optimal statistical approach.

A recent breakthrough in PAT research is the exact reconstruction theories. Xu *et al.* reported exact Fourier-domain reconstructions for spherical [45] and cylindrical [46] measurement geometries with point-detector measurements. Both Xu *et al.* [47] and

Köstli *et al.* [48,49] presented an exact Fourier-domain reconstruction for planar scans. Xu *et al.* [45,50,51] also demonstrated that exact Fourier-domain reconstructions can be closely approximated by time-domain modified back-projection formulas with spatial weighting factors, which are the cosines of the angles between the normal of the detection surface and the vectors from the detection positions to the reconstructed points of the acoustic sources. These works clearly revealed the degree of approximation between the exact solutions and the approximate back-projection methods including those reported by other researchers [36-42].

PAT can be used to image animal or human organs, such as the breast and the brain, where the angiogenesis networks, blood vessels, or blood perfusion can be measured. Recent experimental PAT works are summarized here. Kruger *et al.* conducted phantom studies [52-53] and developed TCT scanners with 434-MHz radio waves to image the breast [54]. They acquired images of porcine kidney [55] as well as of human subjects [56,57]. Kruger *et al.* [58,59] also designed small-animal imaging systems using ultrasound transducer arrays and pulsed laser excitations, and phantom samples as well as nude mice were imaged *ex vivo*. Katabutov and Oraevsky *et al.* [60] pursued OAT in biological tissues, and their recent work was summarized in the preceding reference. Esenaliev *et al.* [61], using a near-IR laser (1064 nm), tested the sensitivity of PAT in detecting small model tumors embedded in bulk phantoms that simulated breast tissues. Oraevsky *et al.* [62] applied an arc array to the detection of breast cancer *in vivo*. Hoelen *et al.* [40,41] demonstrated that PAT can image blood vessels with high resolution *ex vivo*. Wang *et al.* [45-47,63-65] tested tissue phantom

samples in various measurement geometries using both laser and RF excitations. They reported the first *in vivo* noninvasive transdermal and transcranial imaging of the structure and function of the rat brain by means of laser-induced PAT [66] and then successfully demonstrated 3D imaging [67]. In addition, an optical method was demonstrated for 2D ultrasonic detection [68-73]; and a material that may be suitable as a breast phantom for use in photoacoustics was also reported [74]. Reports of more experiments can be found in recent proceedings [13-16].

### **E. Outline**

In this dissertation, we focus on the development of reconstruction algorithms of PAT for breast imaging. First, detailed derivations of both Fourier-domain and time-domain formulas are presented in Chapter II. Then, some key technical issues including spatial resolution and sampling strategy are investigated in Chapter III and IV, respectively. Finally, a prototype of an RF-induced PA imaging system is introduced and experiments using phantom samples as well as a preliminary study of breast imaging for cancer detection are reported in Chapter V.

## **CHAPTER II**

### **RECONSTRUCTION ALGORITHMS**

#### **A. Introduction**

The key of success in PAT is appropriate reconstruction algorithms. In general, different measurement geometries need different reconstruction algorithms. The three geometries commonly used are planar, cylindrical and spherical surfaces.

As mentioned in Chapter I, various reconstruction algorithms have been reported. Among them, the Fourier-domain reconstruction formulas [45-49], based on a full-angle view, are exact, but they are not likely to be widely used because of their requirement of multiple integrations or infinite-series summations and also because of the limited-angle view in practical applications and the difficulty of precisely interpolating in the Fourier domain. The reconstruction algorithms based on matrix inversion or iterative methods [39,43] are also not likely to be widely implemented because of their memory-storage requirement and the time-consuming computation required for the reconstruction of complicated structures. In practical applications, the back-projection or delay-and-sum [32,38,40-42] method is the most widely utilized reconstruction algorithm; this method is based on the idea that different acoustic sources in a sample can be differentiated by the traversed times and intensities of the photoacoustic signals measured by the detectors, since pulse-induced photoacoustic signals are wide-band signals.

Most back-projection algorithms have been proposed for PAT on a case-by-case basis in specific geometries. These algorithms were not derived based on the exact

reconstruction theory of PA imaging, but simply borrowed from other imaging modalities, such as x-ray tomography or ultrasound imaging. Their practical applications in PAT are quite limited. The degrees of approximation of these algorithms in applications of PAT have not been clearly addressed. The questions of what kinds of quantities are proper for summation and how to properly do the summation have not been clearly resolved either.

In this chapter, by constructing Dirichlet Green's function, we first present a formal reconstruction formula for arbitrary measurement geometry. Then, we can directly write down the Fourier-domain reconstruction algorithms for the three common measurement geometries. Next, we present a universal and exact time-domain back-projection (BP) formula for the three common geometries. We also demonstrate this BP formula can be extended to general geometries under certain conditions. A method for implementing this algorithm is also described. Finally, numerical simulations are conducted to test the performance of the BP formula.

## **B. Fourier-domain algorithms**

We start by providing a description of the measurement geometry. As Fig. 2.1 shows, we assume that  $S_0$  is the measurement surface that encloses the source  $p_0(\mathbf{r}')$ . Particularly, for the planar geometry, we assume there is another planar surface  $S'_0$  (parallel to  $S_0$ ) at infinity and that the combination of  $S'_0$  and  $S_0$  encloses the source  $p_0(\mathbf{r}')$ . For convenience, we denote  $S = S_0 + S'_0$  for the planar geometry and  $S = S_0$  for the other two geometries.

In principle, we can construct a Dirichlet Green's function  $\tilde{G}_k^{(D)}(\mathbf{r}, \mathbf{r}_1)$  [23,26], which satisfies the boundary condition:  $\tilde{G}_k^{(D)}(\mathbf{r}, \mathbf{r}_1) = 0$  for  $\mathbf{r}_1$  on  $S$  and  $\mathbf{r}$  inside  $S$ . Then, according to Green's theorem, the acoustic pressure  $\tilde{p}(\mathbf{r}, k)$  inside surface  $S$  can be computed by the surface integral:

$$\tilde{p}(\mathbf{r}, k) = \int_S dS \tilde{p}(\mathbf{r}_0, k) [\mathbf{n}_0^s \cdot \nabla_0 \tilde{G}_k^{(D)}(\mathbf{r}, \mathbf{r}_0)], \quad (2.1)$$

where  $\nabla_0$  denotes the gradient over variable  $\mathbf{r}_0$  and  $\mathbf{n}_0^s$  is the normal of surface  $S$  pointing to the source. Since  $p_0(\mathbf{r}) = p(\mathbf{r}, \bar{t} = 0)$ , we get

$$p_0(\mathbf{r}) = 1/(2\pi) \int_{-\infty}^{+\infty} dk \int_S dS \tilde{p}(\mathbf{r}_0, k) [\mathbf{n}_0^s \cdot \nabla_0 \tilde{G}_k^{(D)}(\mathbf{r}, \mathbf{r}_0)]. \quad (2.2)$$

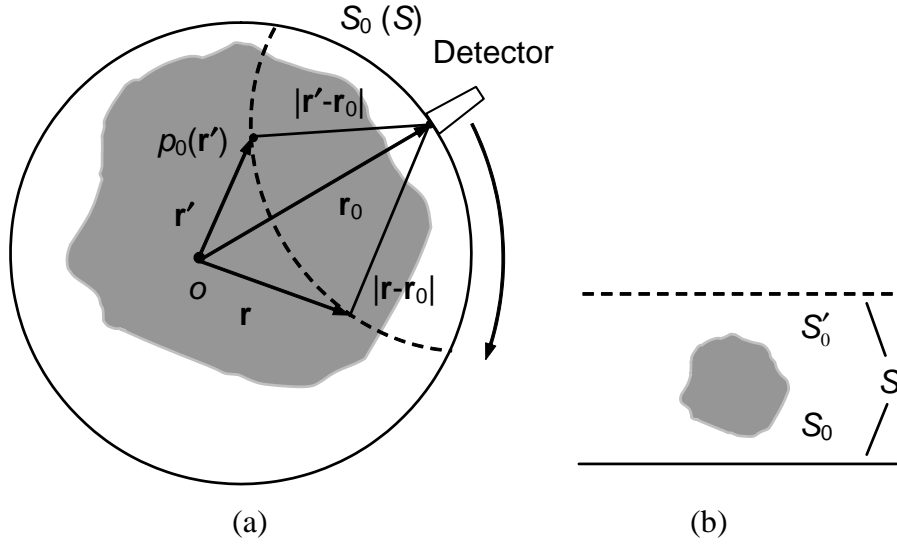


FIG. 2.1. (a) In the measurement, an ultrasonic detector at position  $\mathbf{r}_0$  on a surface  $S_0$  receives PA signals emitted from source  $p_0(\mathbf{r}')$ . In the reconstruction, a quantity related to the measurement at position  $\mathbf{r}_0$  projects backward on a spherical surface with respect to position  $\mathbf{r}_0$ . (b) In the planar geometry, assume there is another surface  $S'_0$  at infinity and that the combination of  $S_0$  and  $S'_0$  encloses the source inside.

For the three common geometries, the function  $\tilde{G}_k^{(D)}(\mathbf{r}, \mathbf{r}_1)$  can be written in some explicit expressions, with which we can directly write down the reconstruction formulas that are consistent to the Fourier-domain formulas summarized in Ref. [75].

### 1. Spherical geometry

As shown in Fig. 2.2(a), it is assumed that the measurement geometry is a spherical surface  $\mathbf{r}_0 = (r_0, \theta_0, \varphi_0)$  in the spherical polar coordinates  $\mathbf{r} = (r, \theta, \varphi)$ , where  $\theta$  is the polar angle from the  $z$ -axis and  $\varphi$  is the azimuth angle in the  $xy$ -plane from the  $x$ -

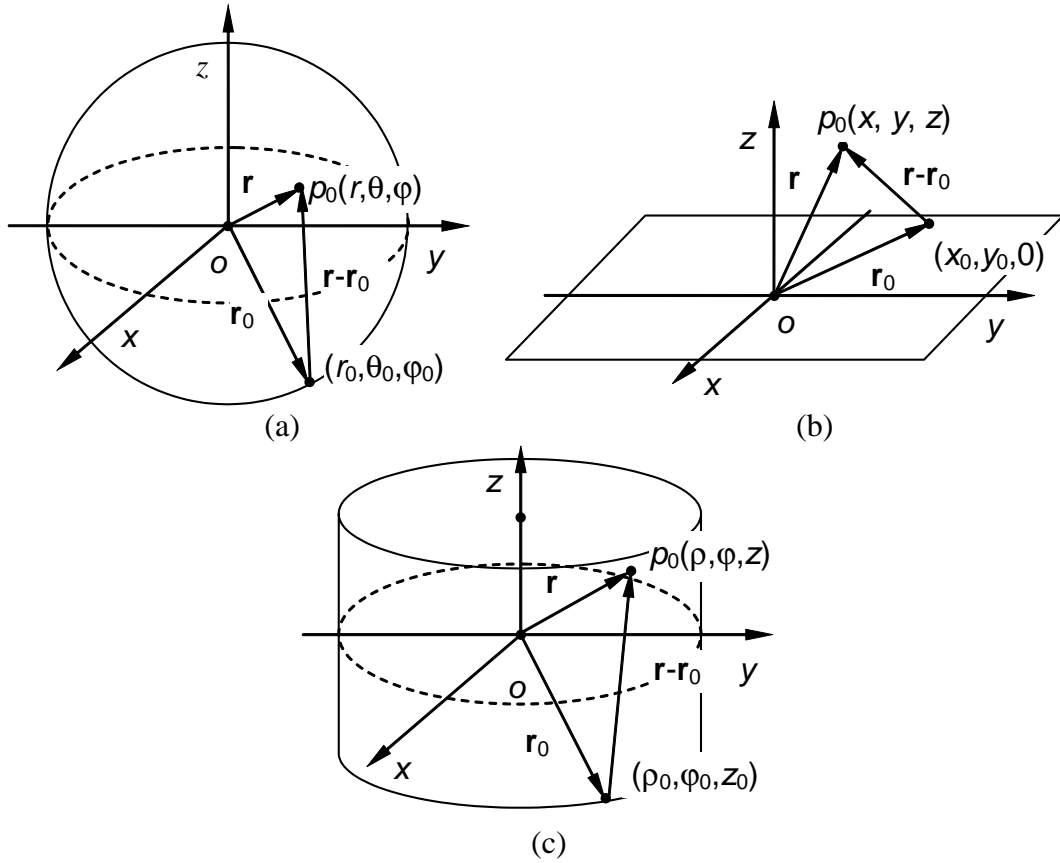


FIG. 2.2. Schematic of measurement geometries: (a) spherical geometry, (b) planar geometry, and (c) cylindrical geometry.

axis. The sample under study lies inside the sphere, i.e.,  $p_0(\mathbf{r}) = p_0(r, \theta, \varphi)$  where  $r < r_0$  and  $p_0(\mathbf{r}) = 0$  when  $r > r_0$ . Compared with Fig. 2.1, in this case,  $S_0: r_1 = r_0$ .

Since  $\mathbf{r}$  is inside  $S_0$ , the Dirichlet Green's function is usually convenient to modify the free-space incoming-wave Green's function (complex conjugate to the outgoing Green's function)

$$\tilde{G}_k^{(in)}(\mathbf{r}, \mathbf{r}_1) = \frac{\exp(-ik|\mathbf{r} - \mathbf{r}_1|)}{4\pi|\mathbf{r} - \mathbf{r}_1|}, \quad (2.3)$$

by the addition of a free standing wave  $\tilde{\Psi}_k(\mathbf{r}, \mathbf{r}_1)$  in the following form [26]:

$$\tilde{G}_k^{(D)}(\mathbf{r}, \mathbf{r}_1) = \tilde{G}_k^{(in)}(\mathbf{r}, \mathbf{r}_1) + \tilde{\Psi}_k(\mathbf{r}, \mathbf{r}_1), \quad (2.4)$$

where

$$(\nabla^2 + k^2)\tilde{G}_k^{(in)}(\mathbf{r}, \mathbf{r}_1) = -\delta(\mathbf{r} - \mathbf{r}_1), \quad (2.5)$$

and

$$(\nabla^2 + k^2)\tilde{\Psi}_k(\mathbf{r}, \mathbf{r}_1) = 0. \quad (2.6)$$

In the spherical geometry, the incoming Green's function can be expanded as [24]:

$$\tilde{G}_k^{(in)}(\mathbf{r}, \mathbf{r}_1) = \frac{-ik}{4\pi} \sum_{l=0}^{\infty} (2l+1) j_l(kr) h_l^{(2)}(kr_1) P_l(\mathbf{n} \cdot \mathbf{n}_1), \quad (k > 0), \quad (2.7)$$

where  $j_l(\cdot)$  is a spherical Bessel function of the first kind;  $h_l^{(2)}(\cdot)$  is a spherical Hankel function of the second kind;  $P_l(\cdot)$  is a Legendre polynomial; and  $\mathbf{n} = \mathbf{r}/r$  and  $\mathbf{n}_1 = \mathbf{r}_1/r_1$  are unit vectors. Therefore, for  $k > 0$ , we construct



$$\begin{aligned}\tilde{G}_k^{(D)}(\mathbf{r}, \mathbf{r}_1) = & (-ik / 4\pi) \sum_{l=0}^{\infty} (2l+1) j_l(kr) P_l(\mathbf{n} \cdot \mathbf{n}_1) \\ & \times [h_l^{(2)}(kr_1) - h_l^{(1)}(kr_1) h_l^{(2)}(kr_0) / h_l^{(1)}(kr_0)].\end{aligned}\quad (2.8)$$

According to the Wronskian formula related to the spherical Hankel functions [24]:

$$h_l^{(1)}(\xi) \frac{dh_l^{(2)}(\xi)}{d\xi} - h_l^{(2)}(\xi) \frac{dh_l^{(1)}(\xi)}{d\xi} = \frac{-2i}{\xi^2}, \quad (2.9)$$

substituting Eq (2.8) into (2.2) gives

$$p_0(\mathbf{r}) = \int_{S_0} dS_0 \int_{-\infty}^{+\infty} dk \tilde{p}(\mathbf{r}_0, k) \tilde{K}(\mathbf{r}_0, \mathbf{r}; k), \quad (2.10)$$

where  $dS_0 = r_0^2 d\Omega_0 = r_0^2 \sin \theta_0 d\theta_0 d\phi_0$  and

$$\tilde{K}(\mathbf{r}_0, \mathbf{r}; k) = \frac{1}{4\pi^2 r_0^2} \sum_{l=0}^{\infty} \frac{(2l+1) j_l(kr)}{h_l^{(1)}(kr_0)} P_l(\mathbf{n}_0 \cdot \mathbf{n}), \quad (k > 0) \quad (2.11)$$

with  $\tilde{K}(\mathbf{r}_0, \mathbf{r}; k) = [\tilde{K}(\mathbf{r}_0, \mathbf{r}; -k)]^*$  ( $k < 0$ ) (\* denotes the complex of conjugate), where

$h_l^{(1)}(\cdot)$  is the spherical Bessel function of the first kind and  $\mathbf{n}_0 = \mathbf{r}_0 / r_0$  is a unit vector.

In addition, Eq. (2.10) is consistent to the following formula summarized in [75]:

$$p_0(\mathbf{r}) = \int_{S_0} dS_0 \int_0^{+\infty} dk \tilde{p}(\mathbf{r}_0, k) \tilde{K}_k(\mathbf{r}_0, \mathbf{r}), \quad (2.12)$$

with  $\tilde{K}_k(\mathbf{r}_0, \mathbf{r}) = 2\tilde{K}(\mathbf{r}_0, \mathbf{r}; k)$ .

## 2. Planar geometry

As show in Fig. 2.2(b), it is assumed that the measurement surface lies in the  $z = 0$  plane, i.e.,  $\mathbf{r}_0 = (x_0, y_0, 0)$  in a Cartesian coordinate system  $\mathbf{r} = (x, y, z)$ . The sample lies above the plane, i.e.,  $p_0(\mathbf{r}) = p_0(x, y, z)$  where  $z > 0$  and  $p_0(\mathbf{r}) = 0$

otherwise. Compared with Fig. 2.1, in this case,  $S_0$ :  $z_1 = 0$  and  $S'_0$  at infinity, and  $\mathbf{n}_0^s$  along axis  $z$ .

By the image method, we construct [24]:

$$\tilde{G}_k^{(D)}(\mathbf{r}, \mathbf{r}_1) = \frac{\exp(-ikR_-)}{4\pi R_-} - \frac{\exp(-ikR_+)}{4\pi R_+}, \quad (2.13)$$

where  $R_{\pm} = \sqrt{(x - x_1)^2 + (y - y_1)^2 + (z \pm z_1)^2}$ . By taking the limit  $S'_0 \rightarrow \infty$ , the integral over surface  $S'_0$  in Eq. (2.2) gives  $p_0(\mathbf{r})/2$ . Therefore,

$$p_0(\mathbf{r}) = 1/\pi \int_{-\infty}^{+\infty} dk \int_{S_0} dS_0 \tilde{p}(\mathbf{r}_0, k) [\mathbf{n}_0^s \cdot \nabla_0 \tilde{G}_k^{(D)}(\mathbf{r}, \mathbf{r}_0)]. \quad (2.14)$$

Further, by substituting Eq. (2.13) into (2.14), we get

$$p_0(\mathbf{r}) = \int_{S_0} dS_0 \int_{-\infty}^{+\infty} dk \tilde{p}(\mathbf{r}_0, k) \tilde{K}(\mathbf{r}_0, \mathbf{r}; k), \quad (2.15)$$

where

$$\tilde{K}(\mathbf{r}_0, \mathbf{r}; k) = (2/\pi) [\mathbf{n}_0^s \cdot \nabla_0 \tilde{G}_k^{(in)}(\mathbf{r}, \mathbf{r}_0)]. \quad (2.16)$$

In addition, the incoming Green's function can be written as [24,26]:

$$\tilde{G}_k^{(in)}(\mathbf{r}, \mathbf{r}_0) = \frac{1}{(2\pi)^3} \int \int \int_{-\infty}^{+\infty} d^3K \frac{\exp[-i\mathbf{K} \cdot (\mathbf{r} - \mathbf{r}_0)]}{K^2 - k^2}. \quad (2.17)$$

Using the contour evaluation in the complex plane [24] and considering the following definition of rectangle function:

$$\text{rect}(\xi) = \begin{cases} 1, & \text{for } |\xi| < 1/2 \\ 0, & \text{otherwise} \end{cases} \quad (2.18)$$

we can rewrite the incoming Green's function as ( $z > z_0$ ):

$$\tilde{G}_k^{(in)}(\mathbf{r}, \mathbf{r}_0) = \frac{1}{(2\pi)^3} \int \int_{-\infty}^{+\infty} dudv \exp[-iu(x-x_0)] \exp[-iv(y-y_0)] \tilde{g}_k(z-z_0, \rho), \quad (2.19)$$

with

$$\begin{aligned} \tilde{g}_k(z-z_0, \rho) = & -\text{rect}\left(\frac{\rho}{2k}\right) i\pi \text{sgn}(k) \frac{\exp\left[-i(z-z_0) \text{sgn}(k) \sqrt{k^2 - \rho^2}\right]}{\sqrt{k^2 - \rho^2}} \\ & - \text{rect}\left(\frac{2k}{\rho}\right) \pi \frac{\exp\left[-(z-z_0) \sqrt{\rho^2 - k^2}\right]}{\sqrt{\rho^2 - k^2}}, \end{aligned} \quad (2.20)$$

where  $\rho = \sqrt{u^2 + v^2}$ ;  $\text{sgn}(k) = 1$  if  $k > 0$  and  $\text{sgn}(k) = -1$  if  $k < 0$ . Therefore, Eq. (2.16)

can be rewritten as

$$\tilde{K}(\mathbf{r}_0, \mathbf{r}; k) = \tilde{K}_k(\mathbf{r}_0, \mathbf{r}) + \tilde{\varepsilon}(\mathbf{r}_0, \mathbf{r}; k), \quad (2.21)$$

where

$$\begin{aligned} \tilde{K}_k(\mathbf{r}_0, \mathbf{r}) = & \frac{1}{4\pi^3} \int \int_{-\infty}^{+\infty} dudv \exp[-iu(x-x_0)] \exp[-iv(y-y_0)] \\ & \times \text{rect}\left(\frac{\rho}{2k}\right) \exp[-iz \text{sgn}(k) \sqrt{k^2 - \rho^2}], \end{aligned} \quad (2.22)$$

and

$$\begin{aligned} \tilde{\varepsilon}(\mathbf{r}_0, \mathbf{r}; k) = & \frac{1}{4\pi^3} \int \int_{-\infty}^{+\infty} dudv \exp[-iu(x-x_0)] \exp[-iv(y-y_0)] \\ & \times (-1) \text{rect}\left(\frac{2k}{\rho}\right) \exp[-z \sqrt{\rho^2 - k^2}]. \end{aligned} \quad (2.23)$$

Substituting Eq. (2.21) into (2.15) gives

$$p_0(\mathbf{r}) = \int_{S_0} dS_0 \int_{-\infty}^{+\infty} dk \tilde{p}(\mathbf{r}_0, k) \tilde{K}_k(\mathbf{r}_0, \mathbf{r}) + \varepsilon(\mathbf{r}), \quad (2.24)$$

where

$$\varepsilon(\mathbf{r}) = \int_{S_0} dS_0 \int_{-\infty}^{+\infty} dk \tilde{p}(\mathbf{r}_0, k) \tilde{\varepsilon}(\mathbf{r}_0, \mathbf{r}; k). \quad (2.25)$$

As shown in Eq. (1.8) in Chapter I,

$$\tilde{p}(\mathbf{r}_0, k) = -ik \int \int_{V'} d^3 r' \tilde{G}_k^{(out)}(\mathbf{r}', \mathbf{r}_0) p_0(\mathbf{r}'). \quad (2.26)$$

The function  $\tilde{G}_k^{(out)}(\mathbf{r}', \mathbf{r}_0)$  can be rewritten as the expression of Eq. (2.19) ( $z' > z_0$ ), i.e.,

$$\tilde{G}_k^{(out)}(\mathbf{r}', \mathbf{r}_0) = [\tilde{G}_k^{(in)}(\mathbf{r}', \mathbf{r}_0)]^* \text{ with the replacements of } u \text{ by } u', v \text{ by } v', \text{ and } \rho \text{ by } \rho'$$

$\rho' = \sqrt{u'^2 + v'^2}$ . Since the identity:

$$\int \int_{S_0} dx_0 dy_0 \exp[ix_0(u - u')] \exp[iy_0(v - v')] = (2\pi)^2 \delta(u - u') \delta(v - v'), \quad (2.27)$$

substituting Eq. (2.26) into (2.25) gives

$$\varepsilon(\mathbf{r}) = \int \int_{V'} d^3 r' p_0(\mathbf{r}') \int_{-\infty}^{+\infty} dk F(\mathbf{r}, \mathbf{r}'), \quad (2.28)$$

where

$$\begin{aligned} F(\mathbf{r}, \mathbf{r}') = & -\frac{ik}{(2\pi)^3} \int \int_{-\infty}^{+\infty} dudv \exp[-iu(x - x') - iv(y - y')] \\ & \times \text{rect}\left(\frac{2k}{\rho}\right) \frac{\exp\left[-(z' + z)\sqrt{\rho^2 - k^2}\right]}{\sqrt{\rho^2 - k^2}}. \end{aligned} \quad (2.29)$$

The above equation shows  $F(\mathbf{r}, \mathbf{r}')$  is an odd function of  $k$ . Thus,  $\varepsilon(\mathbf{r}) = 0$ . Therefore,

$$p_0(\mathbf{r}) = \int_{S_0} dS_0 \int_{-\infty}^{+\infty} dk \tilde{p}(\mathbf{r}_0, k) \tilde{K}_k(\mathbf{r}_0, \mathbf{r}), \quad (2.30)$$

with  $\tilde{K}_k(\mathbf{r}_0, \mathbf{r})$  as the expression of Eq. (2.22), which is consistent to the formula summarized in [75].

### 3. Cylindrical geometry

As shown in Fig. 2.2(c), it is assumed that the measurement surface is a circular cylindrical surface  $\mathbf{r}_0 = (\rho_0, \varphi_0, z_0)$  in a circular cylindrical coordinate system  $\mathbf{r} = (\rho, \varphi, z)$ . The sample lies in the cylinder, i.e.,  $p_0(\mathbf{r}) = p_0(\rho, \varphi, z)$  where  $\rho < \rho_0$  and  $p_0(\mathbf{r}) = 0$  otherwise. In this case,  $S_0: \rho_1 = \rho_0$ . The incoming Green's function can be expressed in the cylindrical coordinates as ( $k > 0$ ):

$$\begin{aligned} \tilde{G}_k^{(in)}(\mathbf{r}, \mathbf{r}_1) = & \frac{1}{4\pi^2} \sum_{n=-\infty}^{+\infty} \exp[in(\varphi_1 - \varphi)] \int_{-\infty}^{+\infty} dk_z \exp[ik_z(z_1 - z)] \\ & \times (-i\pi/2) J_n(\mu^* \rho) H_n^{(2)}(\mu^* \rho_1), \end{aligned} \quad (2.31)$$

where  $\mu = \sqrt{k^2 - k_z^2}$  ( $k > k_z$ ) and  $\mu = i\sqrt{k_z^2 - k^2}$  ( $k < k_z$ );  $J_n(\cdot)$  and  $H_n^{(2)}(\cdot)$  are a Bessel function of the first kind and a Hankel function of the second kind, respectively.

Then, we construct

$$\begin{aligned} \tilde{G}_k^{(D)}(\mathbf{r}, \mathbf{r}_1) = & (1/4\pi^2) \sum_{n=-\infty}^{+\infty} \exp[in(\varphi_1 - \varphi)] \\ & \times \int_{-\infty}^{+\infty} dk_z \exp[ik_z(z_1 - z)] \tilde{g}_n(\rho, \rho_1, \rho_0; \mu) \end{aligned} \quad (2.32)$$

with

$$\begin{aligned} \tilde{g}_n(\rho, \rho_1, \rho_0; \mu) = & (-i\pi/2) J_n(\mu^* \rho) \\ & \times [H_n^{(2)}(\mu^* \rho_1) - H_n^{(1)}(\mu \rho_1) H_n^{(2)}(\mu^* \rho_0) / H_n^{(1)}(\mu \rho_0)], \end{aligned} \quad (2.33)$$

where  $H_n^{(1)}(\cdot)$  is a Hankel function of the first kind. According to the Wronskian formula related to the Hankel functions [24]:

$$H_n^{(1)}(\xi) \frac{dH_n^{(2)}(\xi)}{d\xi} - H_n^{(2)}(\xi) \frac{dH_n^{(1)}(\xi)}{d\xi} = \frac{-4i}{\pi \xi}, \quad (2.34)$$

substituting Eq. (2.32) into (2.2) gives

$$p_0(\rho, \varphi, z) = \int \int_{S_0} dS_0 \int_{-\infty}^{+\infty} dk \tilde{p}(\mathbf{r}_0, k) \tilde{K}(\mathbf{r}_0, \mathbf{r}; k), \quad (2.35)$$

where  $dS_0 = \rho_0 d\varphi_0 dz_0$ ; for  $k > 0$

$$\begin{aligned} \tilde{K}(\mathbf{r}_0, \mathbf{r}; k) &= \frac{1}{4\pi^3 \rho_0} \int_{-\infty}^{+\infty} \text{rect}\left(\frac{k_z}{2k}\right) dk_z \exp[ik_z(z_0 - z)] \\ &\times \sum_{n=-\infty}^{+\infty} \exp[in(\varphi_0 - \varphi)] \frac{J_n(\rho\mu)}{H_n^{(1)}(\rho_0\mu)}, \end{aligned} \quad (2.36)$$

and for  $k < 0$ ,  $\tilde{K}(\mathbf{r}_0, \mathbf{r}; k) = [\tilde{K}(\mathbf{r}_0, \mathbf{r}; -k)]^*$ ; and  $H_n^{(1)}(\cdot)$  is a Hankel function of the first kind.

In addition, Eq. (2.33) is consistent to the following formula summarized in [75]:

$$p_0(\mathbf{r}) = \int_{S_0} dS_0 \int_0^{+\infty} dk \tilde{p}(\mathbf{r}_0, k) \tilde{K}_k(\mathbf{r}_0, \mathbf{r}), \quad (2.37)$$

with  $\tilde{K}_k(\mathbf{r}_0, \mathbf{r}) = 2\tilde{K}(\mathbf{r}_0, \mathbf{r}; k)$ .

## C. Universal time-domain algorithm

### 1. Back-projection formula

Our further study shows that the Fourier-domain reconstruction formulas for the three common geometries can be further simplified into a universal back-projection formula; however, the derivations on a case-by-case base are too extensive. For readability, we first propose the BP formula, and then demonstrate the exactness of the formula.

The back-projection formula takes the following form:

$$p_0^{(b)}(\mathbf{r}) = \frac{1}{\pi} \int_S dS \int_{-\infty}^{+\infty} dk \tilde{p}(\mathbf{r}_0, k) [\mathbf{n}_0^s \cdot \nabla_0 \tilde{G}_k^{(in)}(\mathbf{r}, \mathbf{r}_0)], \quad (2.38)$$

where  $\tilde{G}_k^{(in)}(\mathbf{r}, \mathbf{r}_0)$  is a Green's function:  $\tilde{G}_k^{(in)}(\mathbf{r}, \mathbf{r}_0) = \exp(-ik|\mathbf{r} - \mathbf{r}_0|)/(4\pi|\mathbf{r} - \mathbf{r}_0|)$ , which corresponds to an incoming wave. The BP formula only involves a free-space Green's function  $\tilde{G}_k^{(in)}(\mathbf{r}, \mathbf{r}_0)$  instead of a boundary-dependent Dirichlet Green's function. In addition, it is straightforward to rewrite Eq. (2.38) in the time domain (to be detailed later).

Now, we begin to prove that the BP formula offers an exact reconstruction of the PA source, i.e.,  $p_0^{(b)}(\mathbf{r}) \equiv p_0(\mathbf{r})$ , for the three common geometries. Substituting Eq. (1.8) into (2.38) gives

$$p_0^{(b)}(\mathbf{r}) = \int \int_{V'} d^3r' p_0(\mathbf{r}') \text{PSF}(\mathbf{r}', \mathbf{r}), \quad (2.39)$$

where  $\text{PSF}(\mathbf{r}', \mathbf{r})$  is a point-spread function (PSF), expressed by

$$\text{PSF}(\mathbf{r}', \mathbf{r}) = \frac{1}{\pi} \int_{-\infty}^{+\infty} ik dk \int_S dS \tilde{G}_k^{(out)}(\mathbf{r}', \mathbf{r}_0) [-\mathbf{n}_0^s \cdot \nabla_0 \tilde{G}_k^{(in)}(\mathbf{r}, \mathbf{r}_0)]. \quad (2.40)$$

According to Gauss's theorem [24], Eq. (2.40) can be rewritten as:

$$\text{PSF}(\mathbf{r}', \mathbf{r}) = \frac{1}{\pi} \int_{-\infty}^{+\infty} ik dk \int_{V_0} dV_0 \nabla_0 \cdot [\tilde{G}_k^{(out)}(\mathbf{r}', \mathbf{r}_0) \nabla_0 \tilde{G}_k^{(in)}(\mathbf{r}, \mathbf{r}_0)], \quad (2.41)$$

where  $V_0$  is the volume enclosed by surface  $S$ .

Because both  $\tilde{G}_k^{(out)}(\mathbf{r}', \mathbf{r}_0)$  and  $\tilde{G}_k^{(in)}(\mathbf{r}, \mathbf{r}_0)$  are scalar functions, we have the identity [24]:

$$\begin{aligned}
& \nabla_0 \cdot [\tilde{G}_k^{(out)}(\mathbf{r}', \mathbf{r}_0) \nabla_0 \tilde{G}_k^{(in)}(\mathbf{r}, \mathbf{r}_0)] \\
&= \nabla_0 \tilde{G}_k^{(out)}(\mathbf{r}', \mathbf{r}_0) \cdot \nabla_0 \tilde{G}_k^{(in)}(\mathbf{r}, \mathbf{r}_0) + \tilde{G}_k^{(out)}(\mathbf{r}', \mathbf{r}_0) \nabla_0^2 \tilde{G}_k^{(in)}(\mathbf{r}, \mathbf{r}_0).
\end{aligned} \tag{2.42}$$

For convenience, we denote  $\nabla'$  as the gradient over variable  $\mathbf{r}'$  and  $\nabla$  as the gradient over variable  $\mathbf{r}$ . Since  $\nabla_0 |\mathbf{r}' - \mathbf{r}_0| = -\nabla' |\mathbf{r}' - \mathbf{r}_0|$  and  $\nabla_0 |\mathbf{r} - \mathbf{r}_0| = -\nabla |\mathbf{r} - \mathbf{r}_0|$ , Eq. (2.42) can be rewritten as

$$\begin{aligned}
& \nabla_0 \cdot [\tilde{G}_k^{(out)}(\mathbf{r}', \mathbf{r}_0) \nabla_0 \tilde{G}_k^{(in)}(\mathbf{r}, \mathbf{r}_0)] \\
&= (\nabla' \cdot \nabla) \tilde{G}_k^{(out)}(\mathbf{r}', \mathbf{r}_0) \tilde{G}_k^{(in)}(\mathbf{r}, \mathbf{r}_0) + \tilde{G}_k^{(out)}(\mathbf{r}', \mathbf{r}_0) \nabla^2 \tilde{G}_k^{(in)}(\mathbf{r}, \mathbf{r}_0).
\end{aligned} \tag{2.43}$$

The Green's functions  $\tilde{G}_k^{(out)}(\mathbf{r}', \mathbf{r}_0)$  and  $\tilde{G}_k^{(in)}(\mathbf{r}, \mathbf{r}_0)$  satisfy the following equations, respectively:

$$\nabla'^2 \tilde{G}_k^{(out)}(\mathbf{r}', \mathbf{r}_0) + k^2 \tilde{G}_k^{(out)}(\mathbf{r}', \mathbf{r}_0) = -\delta(\mathbf{r}' - \mathbf{r}_0), \tag{2.44}$$

and

$$\nabla^2 \tilde{G}_k^{(in)}(\mathbf{r}, \mathbf{r}_0) + k^2 \tilde{G}_k^{(in)}(\mathbf{r}, \mathbf{r}_0) = -\delta(\mathbf{r} - \mathbf{r}_0). \tag{2.45}$$

Multiplying Eq. (2.44) by  $\tilde{G}_k^{(in)}(\mathbf{r}, \mathbf{r}_0)$  and (2.45) by  $\tilde{G}_k^{(out)}(\mathbf{r}', \mathbf{r}_0)$ , then subtracting them and rearranging, we obtain

$$\begin{aligned}
& \tilde{G}_k^{(out)}(\mathbf{r}', \mathbf{r}_0) \nabla^2 \tilde{G}_k^{(in)}(\mathbf{r}, \mathbf{r}_0) \\
&= (1/2)[(\nabla^2 + \nabla'^2) \tilde{G}_k^{(out)}(\mathbf{r}', \mathbf{r}_0) \tilde{G}_k^{(in)}(\mathbf{r}, \mathbf{r}_0) \\
&+ \delta(\mathbf{r}' - \mathbf{r}_0) \tilde{G}_k^{(in)}(\mathbf{r}, \mathbf{r}_0) - \delta(\mathbf{r} - \mathbf{r}_0) \tilde{G}_k^{(out)}(\mathbf{r}', \mathbf{r}_0)].
\end{aligned} \tag{2.46}$$

We then substitute Eq. (2.46) into (2.43) and further substitute Eq. (2.43) into (2.41) and rewrite  $\text{PSF}(\mathbf{r}', \mathbf{r})$  as a summation of two terms:

$$\text{PSF}(\mathbf{r}', \mathbf{r}) = P^{(1)}(\mathbf{r}', \mathbf{r}) + P^{(2)}(\mathbf{r}', \mathbf{r}), \tag{2.47}$$

where the first term is



$$P^{(1)}(\mathbf{r}', \mathbf{r}) = \frac{1}{\pi} \int_{-\infty}^{+\infty} ik dk \int_{V_0} dV_0 \quad (2.48)$$

$$\times (1/2) [\delta(\mathbf{r}' - \mathbf{r}_0) \tilde{G}_k^{(in)}(\mathbf{r}, \mathbf{r}_0) - \delta(\mathbf{r} - \mathbf{r}_0) \tilde{G}_k^{(out)}(\mathbf{r}', \mathbf{r}_0)],$$

and the second term is

$$P^{(2)}(\mathbf{r}', \mathbf{r}) = \frac{1}{2\pi} (\nabla + \nabla')^2 \int_{-\infty}^{+\infty} ik dk \quad (2.49)$$

$$\times \int_{V_0} dV_0 \tilde{G}_k^{(out)}(\mathbf{r}', \mathbf{r}_0) \tilde{G}_k^{(in)}(\mathbf{r}, \mathbf{r}_0),$$

The first term reduces to a delta function:  $P^{(1)}(\mathbf{r}', \mathbf{r}) = \delta(|\mathbf{r}' - \mathbf{r}|) / (2\pi |\mathbf{r}' - \mathbf{r}|^2) = \delta(\mathbf{r}' - \mathbf{r})$ .

The second term involves a volume integral that depends on the measurement geometry.

Particularly, when  $\mathbf{r}' = \mathbf{r}$ ,  $P^{(2)}(\mathbf{r}', \mathbf{r}) = 0$ . The second term can also be rewritten as

$$P^{(2)}(\mathbf{r}', \mathbf{r}) = \frac{1}{2\pi} (\nabla + \nabla')^2 [err^+ + (err^+)^*], \quad (2.50)$$

where  $*$  denotes the complex conjugate and  $err^+ = i \int_0^{+\infty} \tilde{F}_k(\mathbf{r}', \mathbf{r}) k dk$  with

$$\tilde{F}_k(\mathbf{r}', \mathbf{r}) = \int_{V_0} dV_0 \tilde{G}_k^{(out)}(\mathbf{r}', \mathbf{r}_0) \tilde{G}_k^{(in)}(\mathbf{r}, \mathbf{r}_0). \quad (2.51)$$

In the spherical geometry, we have ( $k > 0$ ) [24]:

$$\tilde{G}_k^{(in)}(\mathbf{r}, \mathbf{r}_0) = \frac{-ik}{4\pi} \sum_{l=0}^{\infty} (2l+1) j_l(kr) h_l^{(2)}(kr_0) P_l(\mathbf{n} \cdot \mathbf{n}_0), \quad (2.52)$$

and  $\tilde{G}_k^{(out)}(\mathbf{r}', \mathbf{r}_0) = [\tilde{G}_k^{(in)}(\mathbf{r}', \mathbf{r}_0)]^*$  with the replacement of  $\mathbf{n}$  by  $\mathbf{n}'$ , where  $\mathbf{n}' = \mathbf{r}' / r$ ,

$\mathbf{n}_0 = \mathbf{r}_0 / r_0$  and  $\mathbf{n} = \mathbf{r} / r$ . Since  $dV_0 = r_0^2 dr_0 d\Omega_0$  and the identity [24]:

$$\int_{\Omega_0} d\Omega_0 P_l(\mathbf{n} \cdot \mathbf{n}_0) P_{l'}(\mathbf{n}' \cdot \mathbf{n}_0) = \frac{4\pi}{2l+1} \delta_{ll'} P_l(\mathbf{n} \cdot \mathbf{n}'), \quad (2.53)$$

substituting  $\tilde{G}_k^{(in)}(\mathbf{r}, \mathbf{r}_0)$  and  $\tilde{G}_k^{(out)}(\mathbf{r}', \mathbf{r}_0)$  with the expansion of Eq. (2.52) into (2.51)

gives

$$\tilde{F}_k(\mathbf{r}', \mathbf{r}) = \frac{k^2}{4\pi} \sum_{l=0}^{\infty} (2l+1) j_l(kr) j_l(kr') P_l(\mathbf{n} \cdot \mathbf{n}') \int_{r_0}^{\infty} r_0^2 dr_0 m_l^2(kr_0), \quad (2.54)$$

with  $m_l^2(kr_0) = j_l^2(kr_0) + n_l^2(kr_0)$ , where  $n_l(\cdot)$  is a spherical Bessel function of the second kind. From Eq. (2.54),  $\tilde{F}_k(\mathbf{r}', \mathbf{r})$  is real. Thus,  $err^+(\mathbf{r})$  becomes purely imaginary.

Therefore, from Eq. (2.50),  $P^{(2)}(\mathbf{r}', \mathbf{r}) = 0$ .

In the planar geometry, we have  $\tilde{G}_k^{(out)}(\mathbf{r}', \mathbf{r}_0) = [\tilde{G}_k^{(in)}(\mathbf{r}', \mathbf{r}_0)]^*$  as the expression of Eq. (2.19) with the replacements of  $\mathbf{r} = (x, y, z)$  by  $\mathbf{r}' = (x', y', z')$ ,  $(u, v)$  by  $(u', v')$ , and  $\rho$  by  $\rho' = \sqrt{u'^2 + v'^2}$ , respectively. Since

$$\int \int_{-\infty}^{+\infty} dx_0 dy_0 \exp[ix_0(u - u')] \exp[iy_0(v - v')] = (2\pi)^2 \delta(u - u') \delta(v - v'), \quad (2.55)$$

substituting  $\tilde{G}_k^{(in)}(\mathbf{r}, \mathbf{r}_0)$  and  $\tilde{G}_k^{(out)}(\mathbf{r}', \mathbf{r}_0)$  into (2.49) gives

$$\begin{aligned} P^{(2)}(\mathbf{r}', \mathbf{r}) = & \frac{1}{32\pi^3} (\nabla + \nabla')^2 \int_0^{+\infty} dz_0 \int \int_{-\infty}^{+\infty} du dv \exp[-iu(x - x') - iv(y - y')] \\ & \times \int_{-\infty}^{+\infty} ikdk \left\{ \text{rect}\left(\frac{\rho}{2k}\right) \frac{\exp[-i(z - z') \text{sgn}(k) \sqrt{k^2 - \rho^2}]}{k^2 - \rho^2} \right. \\ & \left. + \text{rect}\left(\frac{2k}{\rho}\right) \frac{\exp[-(z + z' - 2z_0) \sqrt{\rho^2 - k^2}]}{\rho^2 - k^2} \right\}. \end{aligned} \quad (2.56)$$

The above equation shows  $P^{(2)}(\mathbf{r}', \mathbf{r}) = 0$ . Actually, in the planar geometry, by taking the limit  $S'_0 \rightarrow \infty$ , the integral over surface  $S'_0$  gives  $p_0(\mathbf{r})/2$ , then, Eq. (2.38) becomes identical to Eq. (2.15).

In the cylindrical geometry, we denote  $\mathbf{r}' = (\rho', \varphi', z')$ ,  $\mathbf{r} = (\rho, \varphi, z)$ , and  $\mathbf{r}_0 = (\rho_0, \varphi_0, z_0)$ . In this case, we have ( $k > 0$ ) [26,75]:

$$\begin{aligned} \tilde{G}_k^{(in)}(\mathbf{r}, \mathbf{r}_0) = & \frac{1}{4\pi^2} \sum_{n=-\infty}^{+\infty} \exp[in(\varphi_0 - \varphi)] \int_{-\infty}^{+\infty} dk_z \exp[ik_z(z_0 - z)] \\ & \times \left[ \frac{-i\pi}{2} \text{rect}\left(\frac{k_z}{2k}\right) J_n(\mu\rho) H_n^{(2)}(\mu\rho_0) + \text{rect}\left(\frac{2k}{k_z}\right) I_n(\mu\rho) K_n(\mu\rho_0) \right], \end{aligned} \quad (2.57)$$

and  $\tilde{G}_k^{(out)}(\mathbf{r}', \mathbf{r}_0) = [\tilde{G}_k^{(in)}(\mathbf{r}', \mathbf{r}_0)]^*$  with the replacements of  $n$  by  $n'$ ,  $k_z$  by  $k'_z$ , and  $\mu$  by  $\mu'$ , respectively, where  $\mu = \sqrt{k^2 - k_z^2}$  and  $\mu' = \sqrt{k^2 - k_z'^2}$ ;  $J_n(\cdot)$  is a Bessel function of the first kind;  $H_n^{(2)}(\cdot)$  is a Hankel function of the second kind;  $I_n(\cdot)$  is a modified Bessel function of the first kind; and  $K_n(\cdot)$  is a modified Bessel function of the second kind. Since  $dV_0 = \rho_0 d\rho_0 d\varphi_0 dz_0$  and the identity [24]:

$$\int_{\varphi_0} d\varphi_0 \exp[i\varphi_0(n - n')] \int_{z_0} dz_0 \exp[iz_0(k_z - k'_z)] = (2\pi)^2 \delta_{nn'} \delta(k_z - k'_z), \quad (2.58)$$

substituting  $\tilde{G}_k^{(in)}(\mathbf{r}, \mathbf{r}_0)$  and  $\tilde{G}_k^{(out)}(\mathbf{r}', \mathbf{r}_0)$  with the expansion of Eq. (2.57) into (2.51)

gives

$$\begin{aligned} \tilde{F}_k(\mathbf{r}', \mathbf{r}) = & \frac{1}{4\pi^2} \sum_{n=-\infty}^{+\infty} \exp[in(\varphi' - \varphi)] \int_{-\infty}^{+\infty} dk_z \exp[ik_z(z' - z)] \\ & \times \left[ \frac{\pi^2}{4} \text{rect}\left(\frac{k_z}{2k}\right) J_n(\mu\rho') J_n(\mu\rho) \int_{\rho_0} d\rho_0 M_n^2(\mu\rho_0) \right. \\ & \left. + \text{rect}\left(\frac{2k}{k_z}\right) I_n(\mu\rho') I_n(\mu\rho) \int_{\rho_0} d\rho_0 K_n^2(\mu\rho_0) \right], \end{aligned} \quad (2.59)$$

with  $M_n^2(\mu\rho_0) = J_n^2(\mu\rho_0) + N_n^2(\mu\rho_0)$ , where  $N_n(\cdot)$  is a Bessel function of the second kind. There are properties:  $Z_{-n}(\cdot) = (-1)^n Z_n(\cdot)$  for  $Z_n = J_n$  and  $N_n$ ; and  $Z_{-n}(\cdot) = Z_n(\cdot)$

for  $Z_n = I_n$  and  $K_n$ . Therefore, the summation  $\sum_{n=-\infty}^{+\infty} \exp[in(\varphi' - \varphi)]$  in Eq. (2.59) reduces to  $\delta(n) + 2 \sum_{n=1}^{+\infty} \cos[n(\varphi' - \varphi)]$ . Because  $\mu = \sqrt{|k^2 - k_z^2|}$ , the integral  $\int_{-\infty}^{+\infty} dk_z \exp[ik_z(z' - z)]$  in Eq. (2.59) reduces to  $\int_{-\infty}^{+\infty} dk_z \cos[k_z(z' - z)]$ . From Eq. (2.59),  $\tilde{F}_k(\mathbf{r}', \mathbf{r})$  is real. Thus,  $err^+(\mathbf{r})$  becomes purely imaginary. Therefore, from Eq. (2.50),  $P^{(2)}(\mathbf{r}', \mathbf{r}) = 0$ .

In conclusion, for all three common geometries, we get  $\text{PSF}(\mathbf{r}', \mathbf{r}) = \delta(\mathbf{r}', \mathbf{r})$ . Therefore, from Eq. (2.39), we prove  $p_0^{(b)}(\mathbf{r}) = p_0(\mathbf{r})$ . Particularly for the planar geometry, by taking the limit  $S'_0 \rightarrow \infty$  in Eq. (2.38), we find that the integral over  $S'_0$  gives  $p_0(\mathbf{r})/2$ . Since the relationship:  $\nabla_0 \tilde{G}_k^{(in)}(\mathbf{r}, \mathbf{r}_0) = -\nabla \tilde{G}_k^{(in)}(\mathbf{r}, \mathbf{r}_0)$ , by taking the inverse Fourier transform of  $\tilde{p}(\mathbf{r}_0, k)$ , we rewrite Eq. (2.38) in the time domain as:

$$p_0^{(b)}(\mathbf{r}) = -\frac{2}{\Omega_0} \nabla \cdot \int_{S_0} \mathbf{n}_0^s dS_0 \left[ \frac{p(\mathbf{r}_0, \bar{t})}{\bar{t}} \right]_{\bar{t}=|\mathbf{r}-\mathbf{r}_0|}, \quad (2.60)$$

where  $\Omega_0$  is the solid angle of the whole surface  $S_0$  with respect to the reconstruction point inside  $S_0$ :  $\Omega_0 = 2\pi$  for the planar geometry and  $\Omega_0 = 4\pi$  for the spherical and cylindrical geometries.

In addition, a similar inversion formula for the spherical geometry was reported in Ref. [76]. We find it can be simplified to Eq. (2.60). We rewrite Eq. (1.8) as:

$$\bar{t} \int_0^{\bar{t}} p(\mathbf{r}_0, \bar{t}) d\bar{t} = (1/4\pi) \int \int_V d^3r p_0(\mathbf{r}) \delta(|\mathbf{r} - \mathbf{r}_0| - \bar{t}). \quad (2.61)$$

If we denote  $\Psi(\mathbf{r}_0, \bar{t}) = \bar{t} \int_0^{\bar{t}} p(\mathbf{r}_0, \bar{t}) d\bar{t}$ , the reconstruction formula for the spherical geometry can be written as [76]:

$$p'_0(\mathbf{r}) = -\frac{2}{r_0 \Omega_0} \nabla^2 \int_{S_0} dS_0 \Psi(\mathbf{r}_0, |\mathbf{r} - \mathbf{r}_0|) / |\mathbf{r} - \mathbf{r}_0|. \quad (2.62)$$

Since  $\nabla |\mathbf{r} - \mathbf{r}_0| = (\mathbf{r} - \mathbf{r}_0) / |\mathbf{r} - \mathbf{r}_0|$ , the above formula reduces to

$$p'_0(\mathbf{r}) = p_0^{(b)}(\mathbf{r}) - \frac{2}{r_0 \Omega_0} \nabla \cdot \mathbf{r} F(\mathbf{r}), \quad (2.63)$$

where

$$\begin{aligned} F(\mathbf{r}) &= \int_{S_0} dS_0 \frac{p(\mathbf{r}_0, |\mathbf{r} - \mathbf{r}_0|)}{|\mathbf{r} - \mathbf{r}_0|} \\ &= 2 \int_{V'} d^3 r' p_0(\mathbf{r}') \int_{-\infty}^{+\infty} (-ik) dk \int_{S_0} dS_0 \tilde{G}_k^{(out)}(\mathbf{r}', \mathbf{r}_0) \tilde{G}_k^{(in)}(\mathbf{r}, \mathbf{r}_0). \end{aligned} \quad (2.64)$$

Similarly to prove  $P^{(2)}(\mathbf{r}', \mathbf{r}) = 0$ , we find  $F(\mathbf{r}) = 0$ . Therefore,  $p'_0(\mathbf{r}) = p_0^{(b)}(\mathbf{r})$ .

Further, we can rewrite Eq (2.60) as

$$p_0^{(b)}(\mathbf{r}) = \frac{1}{\Omega_0} \int_{\Omega_0} b(\mathbf{r}_0, \bar{t} = |\mathbf{r} - \mathbf{r}_0|) d\Omega_0, \quad (2.65)$$

with the back-projection term:

$$b(\mathbf{r}_0, \bar{t}) = 2p(\mathbf{r}_0, \bar{t}) - 2\bar{t} \frac{\partial}{\partial \bar{t}} p(\mathbf{r}_0, \bar{t}), \quad (2.66)$$

where  $d\Omega_0 = dS_0 / |\mathbf{r} - \mathbf{r}_0|^2 \cdot [\mathbf{n}_0^s \cdot (\mathbf{r} - \mathbf{r}_0) / |\mathbf{r} - \mathbf{r}_0|]$ , which is the solid angle for a detection element  $dS_0$  with respect to a reconstruction point at  $\mathbf{r}$ . As shown in Fig. 2.1, the reconstruction simply projects the quantity  $b(\mathbf{r}_0, \bar{t})$ , which is related to the measurement at position  $\mathbf{r}_0$ , backward on a spherical surface with respect to position  $\mathbf{r}_0$ . The term

$d\Omega_0/\Omega_0$  in Eq. (2.65) is a factor weighting the contribution to the reconstruction from the detection element  $dS_0$ . The first derivative over time  $t$  actually represents a pure ramp filter  $k$  in the frequency domain. The ramp filter depresses the low-frequency signal. It is not surprising that the relatively high-frequency components of the PA signal play the primary role in the reconstruction of the acoustic source inside the tissue. In the special case when  $k|\mathbf{r} - \mathbf{r}_0| \gg 1$ ,  $\bar{t} \partial p(\mathbf{r}_0, \bar{t}) / \partial \bar{t} \gg p(\mathbf{r}_0, \bar{t})$ , therefore  $b(\mathbf{r}_0, \bar{t}) \approx -2\bar{t} \partial p(\mathbf{r}_0, \bar{t}) / \partial \bar{t}$ .

In addition, in the case that the detecting distances between the photoacoustic sources and the detecting transducers are much greater than the wavelengths of the high-frequency photoacoustic signals, i.e.,  $k|\mathbf{r}' - \mathbf{r}_0| \gg 1$  and  $k|\mathbf{r} - \mathbf{r}_0| \gg 1$  ( $r_0 \gg r'$ ,  $r_0 \gg r$ ), with the following first-order approximations:

$$\tilde{G}_k^{(out)}(\mathbf{r}', \mathbf{r}_0) \approx \frac{\exp(ikr_0)}{4\pi r_0} \cdot \exp(-ik\mathbf{n}_0 \cdot \mathbf{r}'), \quad (2.67)$$

and

$$\tilde{G}_k^{(in)}(\mathbf{r}, \mathbf{r}_0) \approx \frac{\exp(-ikr_0)}{4\pi r_0} \cdot \exp(ik\mathbf{n}_0 \cdot \mathbf{r}), \quad (2.68)$$

Eq. (2.49) reduces to

$$P^{(2)}(\mathbf{r}', \mathbf{r}) = \frac{1}{2\pi} (\nabla + \nabla')^2 \int_{-\infty}^{+\infty} ikdk \int_{V_0} dV_0 \frac{\exp[ik\mathbf{n}_0 \cdot (\mathbf{r} - \mathbf{r}')] }{(4\pi r_0)^2}. \quad (2.69)$$

It is easy to show  $P^{(2)}(\mathbf{r}', \mathbf{r}) = 0$ . Therefore, if  $k|\mathbf{r} - \mathbf{r}_0| \gg 1$ , the back-projection formula Eq. (2.60) can be extended to arbitrary geometry with good approximation in the detection of small (compared with the measurement geometry) but deeply buried objects.

## 2. Implementation method

Next, we discuss how to implement the BP algorithm. Usually, the EM pulse  $I_e(t)$  is not a delta function. However, as discussed in Chapter I, the thermal diffusion effect is negligible in most soft tissues. Thus, as Eq. (1.2) described in Chapter I, the initial PA source satisfies the following equation:

$$\nabla^2 p(\mathbf{r}, t) - \frac{1}{c^2} \frac{\partial^2}{\partial t^2} p(\mathbf{r}, t) = -p_0(\mathbf{r}) \frac{dI_e(t)}{cdt}. \quad (2.70)$$

Consider a detector with an impulse response of  $I_d(t)$ ; we can write the measurement as:

$$p'(\mathbf{r}_0, t) = H(t) \otimes p(\mathbf{r}_0, t), \quad (2.71)$$

with

$$H(t) = I_e(t) \otimes I_d(t), \quad (2.72)$$

where  $p(\mathbf{r}_0, t)$  is the pressure with a  $\delta(t)$  EM excitation and its Fourier transform  $\tilde{p}(\mathbf{r}_0, k)$  is expressed by Eq. (1.8); and  $\otimes$  denotes a convolution. Thus, the spectrum of the measurement can be expressed by

$$\tilde{p}'(\mathbf{r}_0, k) = \tilde{H}(k) \tilde{p}(\mathbf{r}_0, k), \quad (2.73)$$

where  $\tilde{H}(k)$  is the Fourier transform of  $H(\bar{t})$ . Replacing  $\tilde{p}(\mathbf{r}_0, k)$  with  $\tilde{p}'(\mathbf{r}_0, k)$  in Eq. (2.38) introduces the factor  $\tilde{H}(k)$  in the PSF expressed by Eq. (2.41), i.e., both in the first term Eq. (2.48) and in the second term Eq. (2.49).

If  $\tilde{H}(k)$  is even, i.e.,  $\tilde{H}(-k) = \tilde{H}(k)$ , it is easy to show  $P^{(2)}(\mathbf{r}', \mathbf{r}) = 0$ . Thus, the PSF equals

$$P^{(1)}(\mathbf{r}', \mathbf{r}) = \frac{1}{4\pi^2} \int_{-\infty}^{+\infty} \tilde{H}(k) j_0(kR) k^2 dk, \quad (2.74)$$

where  $R = |\mathbf{r} - \mathbf{r}'|$ , i.e.,

$$\text{PSF}(R) = -\frac{1}{2\pi R} \frac{dH(R)}{dR}, \quad (2.75)$$

which is identical to the result in Ref. [75]. Since  $H(\bar{r})$  is real,  $\tilde{H}(-k) = [\tilde{H}(k)]^*$ . If  $\tilde{H}(k)$  is odd, i.e.,  $\tilde{H}(-k) = -\tilde{H}(k)$ ,  $P^{(1)}(\mathbf{r}', \mathbf{r}) = 0$ . Usually, however,  $P^{(2)}(\mathbf{r}', \mathbf{r}) \neq 0$ . In this case, the BP formula Eq. (2.60) gives a “bad” reconstruction, because  $P^{(2)}(\mathbf{r}', \mathbf{r})$  doesn’t converge to a point as  $P^{(1)}(\mathbf{r}', \mathbf{r})$  does. In other words, because acoustic pressure is phase-sensitive, the reconstruction may be seriously destroyed due to the phase-distortions that are introduced in the measured PA signals by  $\tilde{H}(k)$ . Moreover, the ramp filter  $k$  clearly indicates the contribution of each frequency component in the reconstruction. If the  $k$  weighting in the different frequency components is not followed, the reconstruction will also be distorted.

Therefore, to accurately recover the source distribution, in principle we need to find a filter to adjust the measurement. Two types of filters are possible. One is to restore the pressure by  $\tilde{F}_1(k)$  such that

$$\tilde{F}_1(k) \tilde{H}(k) = 1, \quad (2.76)$$

and

$$\tilde{F}_1(k) \tilde{p}'(\mathbf{r}_0, k) = \tilde{p}(\mathbf{r}_0, k). \quad (2.77)$$

The other is to restore the derivative of the pressure, by  $\tilde{F}_2(k)$  such that



$$\tilde{F}_2(k)\tilde{H}(k) = -ik, \quad (2.78)$$

and

$$\tilde{F}_2(k)\tilde{p}'(\mathbf{r}_0, k) = -ik\tilde{p}(\mathbf{r}_0, k). \quad (2.79)$$

Since the real measurement is band-limited, we need to add a low-pass filter, such as a Hanning window, to dampen the noisy high-frequency components. Sometimes, we also need to remove a small portion of the low-frequency components if the ultrasound detectors are not sensitive in that frequency range. For convenience, we denote the additional band-pass filter as  $\tilde{W}(k)$ . With filter  $\tilde{F}_1(k)$ , we compute

$$S_1^{(1)}(\mathbf{r}_0, \bar{t}) = FT^{-1}[\tilde{W}(k)\tilde{F}_1(k)\tilde{p}'(\mathbf{r}_0, k)], \quad (2.80)$$

and

$$S_1^{(2)}(\mathbf{r}_0, \bar{t}) = FT^{-1}[-ik\tilde{W}(k)\tilde{F}_1(k)\tilde{p}'(\mathbf{r}_0, k)], \quad (2.81)$$

where the Fourier transform

$$FT^{-1}[(\cdot)] = (1/2\pi) \int_{-\infty}^{+\infty} (\cdot) \exp(-ikt) dk. \quad (2.82)$$

which can be performed by the fast Fourier transform algorithm. Thus, the back-projection term is

$$b(\mathbf{r}_0, \bar{t}) = 2S_1^{(1)}(\mathbf{r}_0, \bar{t}) - 2\bar{t}S_1^{(2)}(\mathbf{r}_0, \bar{t}). \quad (2.83)$$

With filter  $\tilde{F}_2(k)$ , we first compute

$$S_2^{(2)}(\mathbf{r}_0, \bar{t}) = FT^{-1}[\tilde{W}(k)\tilde{F}_2(k)\tilde{p}'(\mathbf{r}_0, k)], \quad (2.84)$$

then,

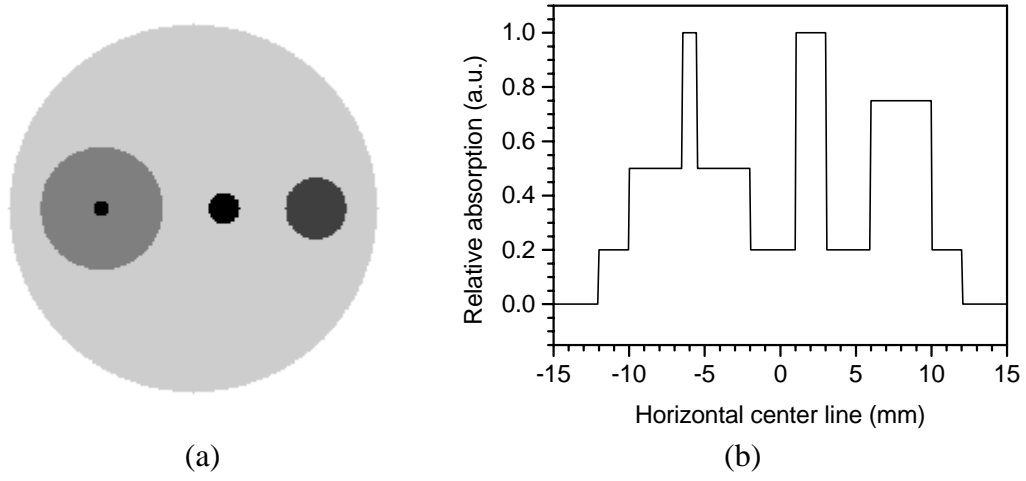


FIG. 2.3. Original sample: (a) a cross-sectional image, (b) a profile along the horizontal center line.

$$S_2^{(1)}(\mathbf{r}_0, \bar{t}) = \int_0^{\bar{t}} S_2^{(2)}(\mathbf{r}_0, \bar{t}) d\bar{t} . \quad (2.85)$$

Thus, the back-projection term is

$$b(\mathbf{r}_0, \bar{t}) = 2S_2^{(1)}(\mathbf{r}_0, \bar{t}) - 2\bar{t}S_2^{(2)}(\mathbf{r}_0, \bar{t}) . \quad (2.86)$$

In addition, instead of the above frequency-domain filters, we can directly construct the corresponding time-domain filters.

### 3. Numerical simulations<sup>1</sup>

Now we want to conduct some numerical experiments to demonstrate the performance of the above BP formulas for PAT.

---

<sup>1</sup> ©2003 IEEE. Reprinted, with permission, from M.-H Xu, Y, Xu and L.-H. Wang, “Time-domain reconstruction algorithms and numerical simulations for thermoacoustic tomography in various geometries,” IEEE Trans. Biomed. Eng. **50**, 1086-1099 (2003).

We consider uniform spherical absorbers surrounded by a non-absorbing background medium. For convenience, we use the centers of the absorbers to denote their positions. The uniform spherical absorber can be written as  $A(\mathbf{r}) = A_0 U(a - |\mathbf{r} - \mathbf{r}_a|)$ , where  $A_0$  is the absorption intensity, and  $a$  and  $\mathbf{r}_a$  are the radius and the center of the sphere, respectively. As shown in Fig. 2.3(a), assume a sample contains five spherical absorbers with different absorption intensities and the centers of these spheres lie in a line parallel to the  $x$ -axis. For convenience, we call this line the horizontal center line. As shown in Fig. 2.3(b), from the smallest to the biggest, the radii are 0.5, 1, 2, 4 and 12 mm, respectively, and the relative absorption intensities are 1, 1, 0.75, 0.5 and 0.2, respectively.

We also assume that the RF pulse duration is very short and can be regarded as a delta function, and, consequently, that the photoacoustic signal irradiated from a uniform sphere can be calculated by  $p(\mathbf{r}_0, t) = (\beta c^2 / C_p) U(a - |R - ct|)(R - ct)/(2R)$ , where  $R$  is the distance between the detection position  $\mathbf{r}_0$  and the absorber center  $\mathbf{r}_a$  ( $R = |\mathbf{r}_0 - \mathbf{r}_a|$ ) [22]. As mentioned before, the quantity  $\partial p(\mathbf{r}_0, t) / \partial t$  can be calculated through the Fourier transform. The band-pass filter we use here is a Hanning window:

$$\tilde{W}(f) = \begin{cases} 0.5 + 0.5 \cos\left(\pi \frac{f}{f_c}\right), & \text{if } |f| < f_c, \\ 0, & \text{otherwise.} \end{cases} \quad (2.87)$$

We assume the photoacoustic waves to be in a frequency range below 4 MHz, and choose  $f_c = 4$  MHz. Here, the data sampling frequency is 20 MHz.

## (a). Spherical geometry

Figure 2.2(a) shows the spherical measurement geometry. To simulate a practical condition, we adopt only a half-spherical measurement area in the upper half space ( $z > 0$ ). Suppose a quarter circular array has 30 elements and the radius of the array is 50 mm. Then one can rotationally scan the array along its radius with a step size of 3 degrees to cover a half spherical measurement area. In this way, the measurement contains 3600 detection positions, which are approximately evenly distributed in the measurement area. The sample center lies (0, 0, 12 mm) inside the measurement surface. Fig. 2.4(a) shows the reconstructed RF absorption distribution of the  $z = 12$  mm plane, and Fig. 2.4(b) shows the comparison of the original and reconstructed absorption profiles along the horizontal center line.

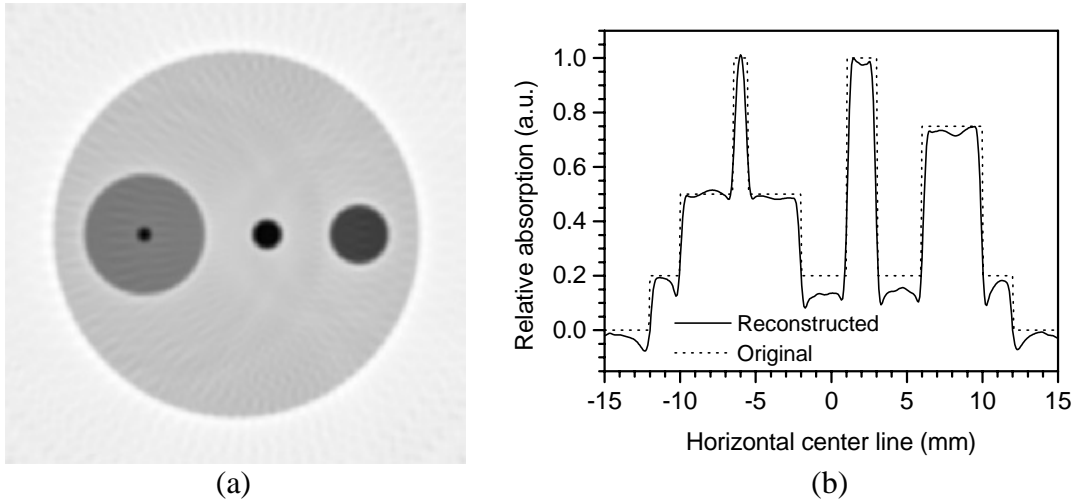


FIG. 2.4. Reconstructed image from spherical measurement geometry using 3600 detector positions with high cutoff frequency 4 MH: (a) a cross-sectional image at the  $z = 12$  mm plane, (b) comparison of the original and reconstructed absorption profiles along the horizontal center line.

## (b). Planar geometry

We use the planar measurement geometry as shown in Fig. 2.2(b). Assume that the measurement area is  $120 \times 120 \text{ mm}^2$  in the  $z = 0$  plane and that the photoacoustic signals are collected at 3600 total detection positions that are evenly distributed in the measurement area. Such a measurement can be realized by using a rectangular ultrasonic array or by scanning a linear array or even by scanning a single detector to cover the measurement area. The center of the measurement area is  $(0, 0, 0)$ . The sample center  $(0, 0, 30)$  lies 30 mm above the measurement area. Fig. 2.5(a) shows the reconstructed RF absorption distribution of the  $z = 30 \text{ mm}$  plane, and Fig. 2.5(b) shows the comparison of the original and reconstructed absorption profiles along the horizontal center line.

## (c). Cylindrical geometry

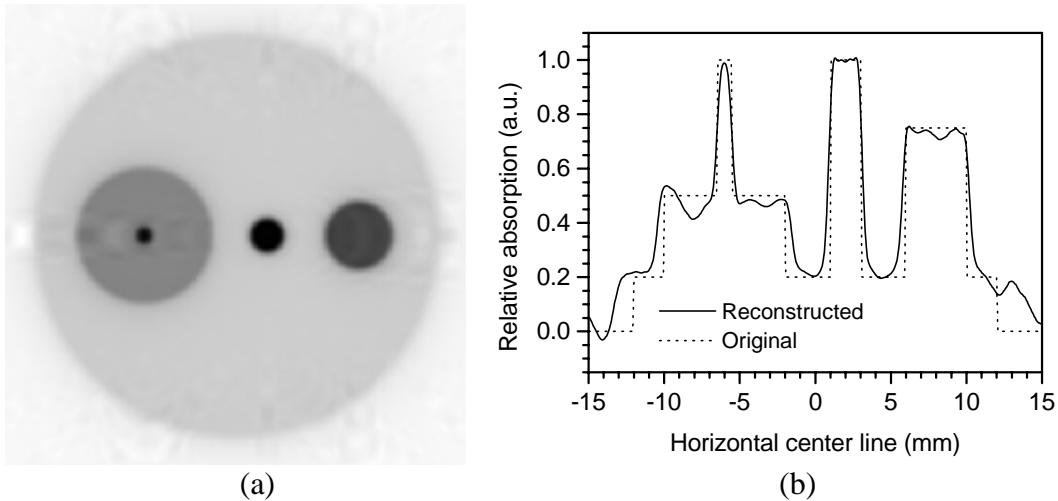


FIG. 2.5. Reconstructed image from planar measurement geometry using 3600 detector positions with high cutoff frequency 4 MHz: (a) a cross-sectional image at the  $z = 30 \text{ mm}$  plane, (b) comparison of the original and reconstructed absorption profiles along the horizontal center line.

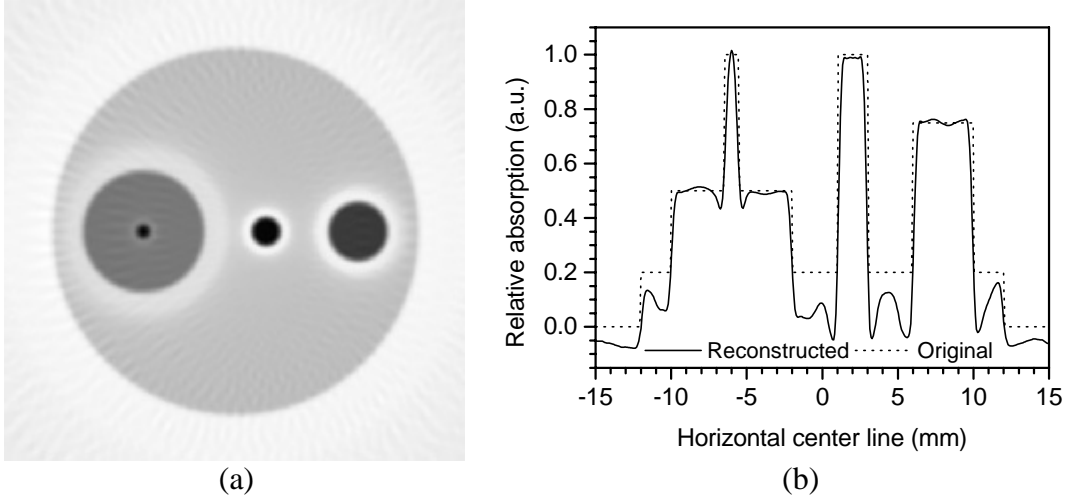


FIG. 2.6. Reconstructed image from cylindrical geometry using 3600 detector positions with high cutoff frequency 4 MHz: (a) a cross-sectional image at the  $z = 0$  mm plane, (b) comparison of the original and reconstructed absorption profiles along the horizontal center line.

We employ the cylindrical measurement geometry as shown in Fig. 2.2(c). Assume the measurement area is a cylindrical surface with a length of 90 mm and a radius of 50 mm. One can use a linear ultrasound array, which is vertically placed and has 30 elements evenly distributed a length of 90 mm, to horizontally scan the sample, with a step size of 3 degrees to cover the measurement area. In this way, the measurement covers 3600 detection positions, which are approximately evenly distributed in the measurement area. The sample center lies at  $(0, 0, 0)$ , the center of the measurement cylindrical surface. Fig. 2.6(a) shows the reconstructed RF absorption distribution in the  $z = 0$  mm plane and Fig. 2.6(b) shows the comparison of the original and reconstructed absorption profiles along the horizontal center line.

The above examples demonstrate the performance of the time-domain formulas for different measurement geometries. The reconstructed profiles are in good agreement

with the original distributions. As mentioned before, with a cutoff frequency  $f_c = 4$  MHz, the dominative frequency in  $f\tilde{W}(f)$  is 1.7 MHz, which corresponds to an acoustic wavelength of 0.9 mm. That explains why the small absorbers, as well as the boundaries of the big absorbers, can be faithfully reconstructed. The flat bases of the big absorbers are not faithfully recovered, which results from the limited-view detection.

(d). Low resolution

However, in the absence of a high frequency signal, the small size structure will be lost. For example, if the cut-off frequency  $f_c = 1.5$  MHz, the dominative frequency in  $f\tilde{W}(f)$  is about 0.6 MHz, which corresponds to an acoustic wavelength of 2.5 mm. Without loss of generality, we will take the spherical measurement geometry as an example. The other parameters in the numerical experiment are the same as the example

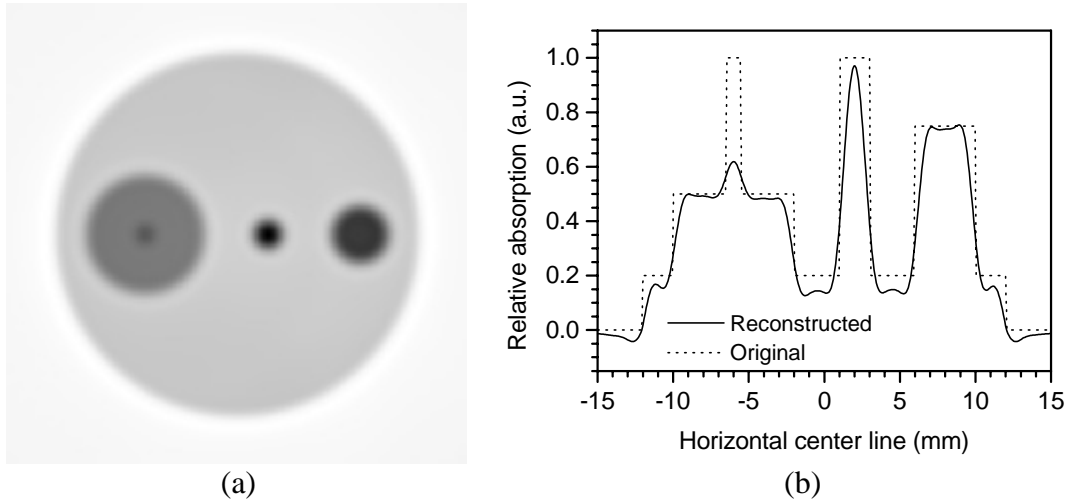


FIG. 2.7. Reconstructed image from spherical measurement geometry using 3600 detector positions with high cutoff frequency 1.5 MHz: (a) a cross-sectional image at the  $z = 12$  mm plane, (b) comparison of the original and reconstructed absorption profiles along the horizontal center line.

shown in Fig. 2.3. As shown in Fig. 2.7, not only is the small absorber nearly corrupted, but also the originally sharp borders of the big absorbers are greatly degraded.

#### **D. Summary**

In summary, we have presented in this Chapter a unified and exact time-domain back-projection algorithm for the three common measurement geometries. This algorithm can be straightforwardly extended to the limited-angle view case, in which the reconstruction may be incomplete and reconstruction artifacts may occur. The solid-angle weighting factor in the BP formula, however, can compensate for the variations in the detection views. Numerical simulations have demonstrated the performance of the back-projection algorithm. In addition, the back-projection formula can also be extended to arbitrary geometry with good approximation in the detection of small (compared with the measurement geometry) but deeply buried object. This BP formula can serve as the basis for time-domain photoacoustic reconstruction in the three-dimensional space.



## CHAPTER III

### SPATIAL RESOLUTION<sup>1</sup>

#### A. Introduction

Spatial resolution is one of the most important parameters of PA imaging. Many factors can affect the quality of a PA image. Important assumptions in reconstruction theory include the homogeneous acoustic property of the tissue sample and the full-angle view measurement. Acoustic inhomogeneity and attenuation blur the reconstructed image [77], although in some cases, the blurring can be corrected. Moreover, in reality, it is physically impossible to collect PA signals over a full-angle view. A limited angular range has to be tolerated. The incomplete data, however, can result in some reconstruction artifacts [78].

The spatial resolution of a PAT image can also be affected by the following parameters: (1) the pulse duration of the excitation EM wave, (2) the temporal-frequency bandwidth of the detection system including the ultrasound detector, and (3) the sensing aperture of the detector element. In the PA measurement, it is desirable to know how to choose appropriate parameters to meet the predefined spatial resolution. Past research work has only estimated the spatial resolution based on measurements or numerical simulations. So far, no general solution to the question has been reported.

---

<sup>1</sup> M.-H Xu and L.-H. Wang, “Analytic explanation of spatial resolution related to bandwidth and detector aperture size in thermoacoustic or photoacoustic reconstruction,” *Phys. Rev. E*, vol. 67, article number: 056605, 2003, pp.1-15. Copyright (2003) by the American Physical Society.

In this chapter, a complete theoretical explanation of the degree of spatial resolution that results from varying the bandwidth as well as the detector aperture is presented. Analytic expressions of point-spread functions on the spherical, planar and cylindrical measurement surfaces are explicitly derived.

## B. Bandwidth-limited PSF

### *1. Space-invariance*

In Chapter II, we have obtained the point-spread function with the bandwidth characterized by  $\tilde{H}(k)$ , for the three common geometries, as:

$$\text{PSF}_b(R) = \frac{1}{4\pi^2} \int_{-\infty}^{+\infty} \tilde{H}(k) j_0(kR) k^2 dk, \quad (3.1)$$

i.e.,

$$\text{PSF}_b(R) = -\frac{1}{2\pi R} \frac{dH(R)}{dR}, \quad (3.2)$$

where subscript  $b$  denotes that the PSF is related to the bandwidth;  $R$  is the distance between the point-source and the reconstruction point; and  $H(t)$  is the temporal shape of the bandwidth  $\tilde{H}(k)$  that is assumed to be an even function. This expression can be derived on a case-by-case base as shown in [75]; however, the derivations are extensive.

Equation (3.2) indicates that the bandwidth-limited PSF is independent of the position of the point source but dependent on the distance  $R$  from the point source. Therefore, the PSF due to bandwidth is space-invariant.

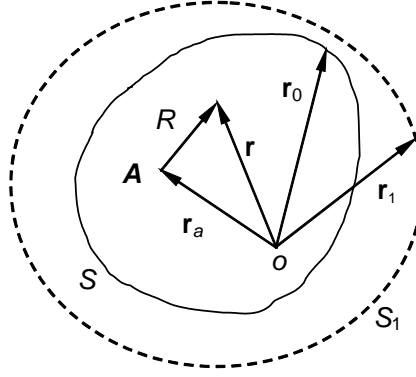


FIG. 3.1. Diagram of the measurement geometry: a measurement surface  $S_1$  completely encloses another measurement surface  $S$ ; there is a point source  $A$  at  $\mathbf{r}_a$  inside  $S$ ;  $R$  is the distance between an arbitrary point at  $\mathbf{r}$  and the point source  $A$ ;  $\mathbf{r}_0$  and  $\mathbf{r}_1$  point to an detection element on the surface  $S$  and  $S_1$ , respectively.

Actually, the space invariance of PSF due to bandwidth can be extended to more general measurement geometries. In chapter II, we find the reconstruction for  $p_0(\mathbf{r})$  can be expressed by a linear integral:

$$p_0(\mathbf{r}) = \int_{-\infty}^{+\infty} dk \int_S dS \tilde{p}(\mathbf{r}_0, k) \tilde{K}(\mathbf{r}_0, \mathbf{r}; k). \quad (3.3)$$

where  $S$  is the measurement surface that covers the object under study and  $\tilde{K}(\mathbf{r}_0, \mathbf{r}; k) = 1/(2\pi)[\mathbf{n}_0^s \cdot \nabla_0 \tilde{G}_k^{(D)}(\mathbf{r}, \mathbf{r}_0)]$ .

As shown in Fig. 3.1, suppose another measurement surface  $S_1$ , which could be a spherical, planar or cylindrical measurement surface, can completely enclose surface  $S$ . Then, based on Green's theorem [26], the pressure  $\tilde{p}(\mathbf{r}_1, k)$  at  $S_1$  can be computed by the pressure  $\tilde{p}(\mathbf{r}_0, k)$  on surface  $S$ ,

$$\tilde{p}(\mathbf{r}_1, k) = \int_S dS \left( \tilde{p}(\mathbf{r}_0, k) \frac{\partial \tilde{G}_k^{(out)}(\mathbf{r}_1, \mathbf{r}_0)}{\partial n_0^s} - \tilde{G}_k^{(out)}(\mathbf{r}_1, \mathbf{r}_0) \frac{\partial \tilde{p}(\mathbf{r}_0, k)}{\partial n_0^s} \right), \quad (3.4)$$

where  $\partial/\partial n_0^s$  is the normal component of the gradient on surface  $S$  and points outward away from the acoustic source; and  $\mathbf{r}_0$  and  $\mathbf{r}_1$  represent detection positions on surfaces  $S$  and  $S_1$ , respectively. Since the reconstruction based on Eq. (3.3) from the measurement on surface  $S$  is exact, the pressure  $\tilde{p}(\mathbf{r}_1, k)$  on surface  $S_1$  must be identical to the PA pressure directly generated by the source  $p_0(\mathbf{r})$ :

$$\tilde{p}(\mathbf{r}_1, k) = -ik \int_{V_0} dV_0 p_0(\mathbf{r}) \tilde{G}_k^{(out)}(\mathbf{r}_1, \mathbf{r}), \quad (3.5)$$

where  $V_0$  is the volume enclosed by  $S$ .

Now, considering the bandwidth  $\tilde{H}(k)$ , one can rewrite the reconstruction Eq. (3.3) as:

$$p'_0(\mathbf{r}) = \int_{-\infty}^{+\infty} dk \int_S dS \tilde{K}(\mathbf{r}_0, \mathbf{r}; k) \cdot [\tilde{H}(k) \tilde{p}(\mathbf{r}_0, k)]. \quad (3.6)$$

In other words, Eq. (3.6) gives the exact reconstruction of a new and unique source  $p'_0(\mathbf{r})$  from  $\tilde{H}(k) \tilde{p}(\mathbf{r}_0, k)$  measured on surface  $S$ :

$$\tilde{H}(k) \tilde{p}(\mathbf{r}_0, k) = -ik \int_{V_0} dV_0 p'_0(\mathbf{r}) \tilde{G}_k(\mathbf{r}_0, \mathbf{r}). \quad (3.7)$$

Based on Green's theorem, the pressure on surface  $S_1$  can be computed by the pressure  $\tilde{H}(k) \tilde{p}(\mathbf{r}_0, k)$  on surface  $S$ , which is found equal to  $\tilde{H}(k) \tilde{p}(\mathbf{r}_1, k)$  with considering Eq. (3.4):

$$\begin{aligned}
& \int_S dS \left( \left[ \tilde{H}(k) \tilde{p}(\mathbf{r}_0, k) \right] \frac{\partial \tilde{G}_k^{(out)}(\mathbf{r}_1, \mathbf{r}_0)}{\partial n_0^s} - \tilde{G}_k^{(out)}(\mathbf{r}_1, \mathbf{r}_0) \frac{\partial [\tilde{H}(k) \tilde{p}(\mathbf{r}_0, k)]}{\partial n_0^s} \right) \\
&= \tilde{H}(k) \int_S dS \left( \tilde{p}(\mathbf{r}_0, k) \frac{\partial \tilde{G}_k^{(out)}(\mathbf{r}_1, \mathbf{r}_0)}{\partial n_0^s} - \tilde{G}_k^{(out)}(\mathbf{r}_1, \mathbf{r}_0) \frac{\partial \tilde{p}(\mathbf{r}_0, k)}{\partial n_0^s} \right) \\
&= \tilde{H}(k) \tilde{p}(\mathbf{r}_1, k).
\end{aligned} \tag{3.8}$$

This pressure must be identical to the PA pressure directly generated by the new source  $p'_0(\mathbf{r})$  in volume  $V_0$ ,

$$-ik \int_{V_0} dV_0 p'_0(\mathbf{r}) \tilde{G}_k(\mathbf{r}_1, \mathbf{r}) = \tilde{H}(k) \tilde{p}(\mathbf{r}_1, k), \tag{3.9}$$

i.e.,

$$\tilde{H}(k) \tilde{p}(\mathbf{r}_1, k) = -ik \int_{V_1} dV_1 p'_0(\mathbf{r}) \tilde{G}_k(\mathbf{r}_1, \mathbf{r}), \tag{3.10}$$

since there is no source in the volume between the surfaces  $S$  and  $S_1$ .

Equation (3.10) indicates that the new source  $p'_0(\mathbf{r})$  could be restored from the value  $\tilde{H}(k) \tilde{p}(\mathbf{r}_1, k)$  on surface  $S_1$ , if an exact reconstruction from data only on surface  $S_1$  does exist. In other words, the reconstruction for  $p'_0(\mathbf{r})$  from the measurement with the bandwidth  $\tilde{H}(k)$  on surface  $S$  is identical to the reconstruction from the measurement with the same bandwidth  $\tilde{H}(k)$  on surface  $S_1$  that fully encloses  $S$ . Fortunately, we have already obtained the exact reconstruction formulas from measurements on such a surface  $S_1$  as the spherical, planar or cylindrical measurement geometries. Therefore, the PSF of the point source as a function of bandwidth  $\tilde{H}(k)$  from the measurement on surface  $S$  is nothing but the same expression as Eq. (3.2).

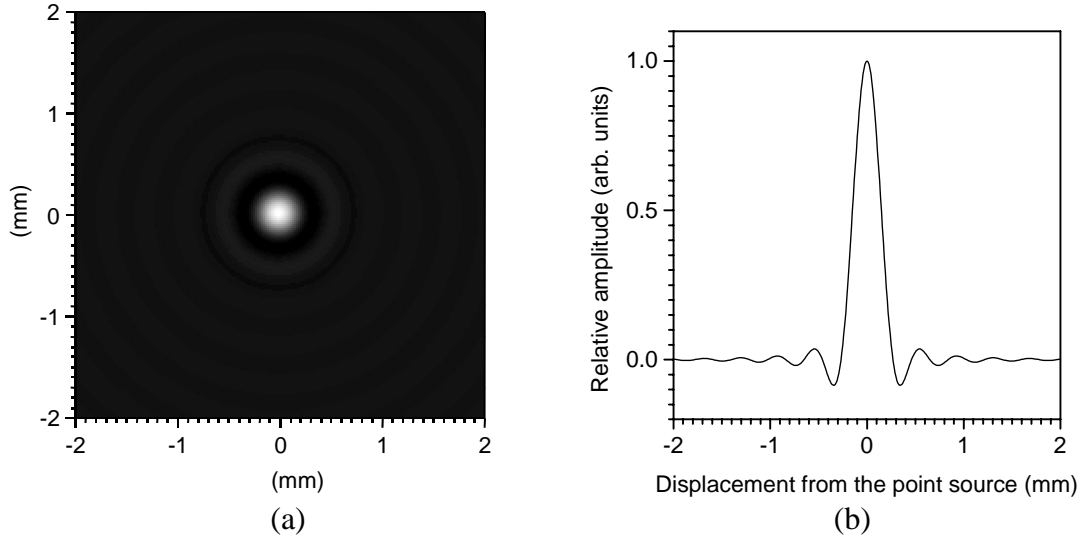


FIG. 3.2. An example of the PSF as a result of the bandwidth (0, 4 MHz): (a) a grayscale view and (b) a profile through the point source.

## 2. Diffraction-limited resolution

We consider a rectangular-shaped band, which is cut off at the frequency of  $f_c$ .

In this case,  $H(t)$  is a sinc function as  $\text{sinc}(k_c t)k_c / \pi$ , where  $\text{sinc}(x) = \sin(x)/x$  and

$k_c = 2\pi/\lambda_c$  ( $\lambda_c = 2\pi c / f_c$ ). From Eq. (3.2), we can easily derive the PSF as

$$\text{PSF}_b(R) = \frac{k_c^3}{2\pi^2} \cdot \frac{j_1(k_c R)}{k_c R}. \quad (3.11)$$

The FWHM characterizes the extension of the PSF, which can be used to represent the spatial resolution. It is easy to show  $3j_1(x)/x = 0.5$  when  $x = 2.4983$ . Therefore, the

FWMH of the PSF

$$R_w = 2 \times \frac{2.4983}{k_c} = 2 \times \frac{2.4983}{2\pi f_c / c} = 0.7952c / f_c \approx 0.8\lambda_c, \quad (3.12)$$

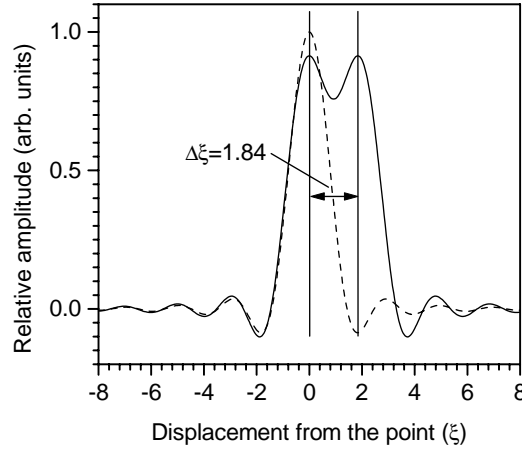


FIG. 3.3. Superposition of two PSF's at the Rayleigh criterion. Dash line: normalized PSF expressed by  $3j_1(\pi x)/(\pi x)$ . Solid line: superposition of two PSF's.

For example, if  $c = 1.5 \text{ mm}/\mu\text{s}$ ,  $f_c = 4 \text{ MHz}$ , then  $\text{FWHM} \approx 0.3 \text{ mm}$ . The corresponding  $\text{PSF}_b(R)$  is plotted in Fig. 3.2 (a) and (b).

In an analogy to the Rayleigh criterion, an alternative definition of spatial resolution is the distance between two PSFs when the maximum (positive) of one PSF at the position of the first minimum (negative) of the second. Figure 3.3 shows the superposition of two PSF's in the above condition, in which two point sources can be clearly distinguished. By this definition, the spatial resolution becomes  $R_s \approx 0.92\lambda_c$ , which is slightly wider than the FWHM. The Rayleigh criterion is more appropriate, however, because negative-valued artifacts are introduced into the reconstruction due to the finite bandwidth.

Sometimes, a detection system has a finite bandwidth characterized by a central frequency  $f_0$  with a low cutoff frequency  $f_{Lc}$  and a high cutoff frequency  $f_{Hc}$ . For

simplicity, suppose  $\tilde{H}(k)=1$  is in the above frequency range, and then the PSF can be expressed by

$$\text{PSF}_b(R) = \frac{k_{Hc}^3}{2\pi^2} \cdot \frac{j_1(k_{Hc}R)}{k_{Hc}R} - \frac{k_{Lc}^3}{2\pi^2} \cdot \frac{j_1(k_{Lc}R)}{k_{Lc}R}, \quad (3.13)$$

where  $k_{Lc} = 2\pi f_{Lc}/c$  and  $k_{Hc} = 2\pi f_{Hc}/c$ .

For example, a system is with  $f_0 = 3$  MHz, and  $f_{Lc} = 2$  MHz and  $f_{Hc} = 4$  MHz. The corresponding PSF is plotted as the dotted-line in Fig. 3.4. As shown in Fig. 3.4, the FWHM of the PSF with a bandwidth of (2 MHz, 4 MHz) is slightly narrower than the FWHM of the PSF with a wider bandwidth of (0, 4 MHz) [solid line in Fig. 3.4]. In other words, due to the absence of a low frequency component, the high frequency component will cause the FWHM to be narrower. The minimum value of the FWHM can be estimated in the PSF with a single frequency  $f_c$  and zero bandwidth. The PSF in

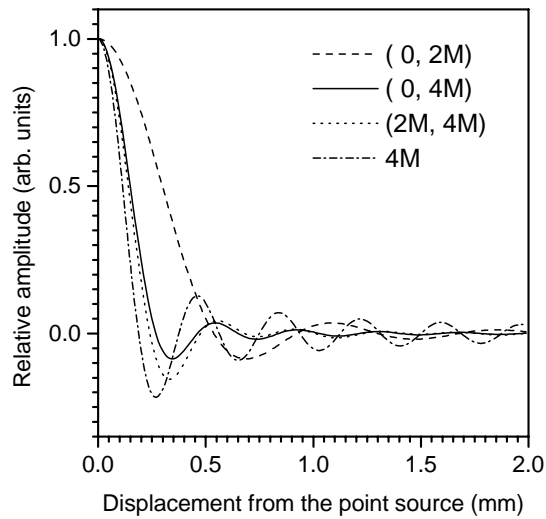


FIG. 3.4. Comparison of the PSF's with different bandwidths: dash-line, (0, 2 MHz); solid-line, (0, 4 MHz); dot-line, (2 MHz, 4 MHz); and dot-dash-line, 4 MHz.



this case is nothing but the integral kernel in Eq. (3.1): the zero-order spherical Bessel function  $j_0(k_c R)$ . Such an example, with  $f_c = 4$  MHz, is plotted as the dash-dot line in Fig. 3.4. Since  $j_0(1.895) \approx 0.5$ , the minimum FWHM  $\approx 0.6 \lambda_c$ , where  $\lambda_c$  is the wavelength at the cutoff frequency  $f_c$ . But, as shown in Fig. 3.4, a PSF that lacks a low frequency component does not concentrate in the center beam any more, and the side beams of the PSF slowly attenuate as the position gets farther away from the point source, thereby introducing significant artifacts in the investigation of large objects.

In summary, the spatial resolution is actually diffraction-limited by the photoacoustic waves. The obtainable spatial resolution is on the order of the photoacoustic wavelength at the dominative frequency.

### C. Effect of detector aperture

Next, let us derive the analytic expressions of the PSF's related to detector aperture size. As shown in Fig. 3.5, the real signal detected at position  $\mathbf{r}_0$  can be expressed as a surface integral over the detector aperture

$$\tilde{p}'_d(\mathbf{r}_0, k) = \iint \tilde{p}(\mathbf{r}'_0, k) W(\mathbf{r}'_0) d^2 \mathbf{r}'_0, \quad (3.14)$$

where  $W(\mathbf{r}'_0)$  is a weighting factor, which represents the contribution from different elements of the detector surface to the total signal of the detector.

Since  $\mathbf{r}'_0 = \mathbf{r}_0 + \mathbf{r}'$ , Eq. (3.14) can be rewritten as

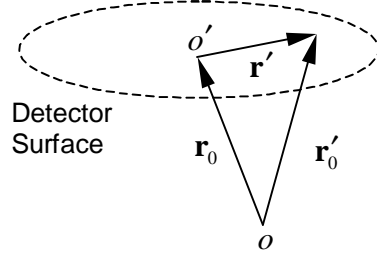


FIG. 3.5. Diagram of the detector surface  $\mathbf{r}'$  with origin  $o'$ . The vector  $\mathbf{r}_0$  represents the center of detector  $o'$  in the measurement geometry with origin  $o$ . The vector  $\mathbf{r}'_0$  points an element of the detector aperture.

$$\tilde{p}'_d(\mathbf{r}_0, k) = \iint \tilde{p}(\mathbf{r}_0 + \mathbf{r}', k) W(\mathbf{r}') d^2\mathbf{r}'. \quad (3.15)$$

We suppose a point source  $p_0(\mathbf{r}) = \delta(\mathbf{r} - \mathbf{r}_a)$  at  $\mathbf{r}_a$ . Then, from Eq. (1.8), we have

$$\tilde{p}(\mathbf{r}_0, k) = -ik \frac{\exp(ik|\mathbf{r}_a - \mathbf{r}_0|)}{4\pi|\mathbf{r}_a - \mathbf{r}_0|}. \quad (3.16)$$

Further, we get the detected signal at position  $\mathbf{r}_0$  using Eq. (3.14) or (3.15). If the signal is not band-limited, by substituting  $\tilde{p}'_d(\mathbf{r}_0, k)$  for  $p(\mathbf{r}_0, k)$  in the exact reconstruction formulas as presented in Chapter II, one can get analytic expression of the  $\text{PSF}_a$  for the spherical, planar or cylindrical geometry, where subscript  $a$  denotes the PSF is related to the sensing aperture. In general, the analytic expressions cannot be thoroughly simplified for arbitrary detector apertures. In order to explicitly demonstrate the effects of the detector apertures on spatial resolution, we have to make some assumptions about the detector apertures.

### 1. Spherical geometry

As shown in Fig. 3.6(a),  $\mathbf{r}_0$  represents the center of detector  $o'$  in the global spherical coordinates  $(r, \theta, \phi)$  with the origin at the measurement geometry center  $o$ . A local spherical coordinate system aligned with  $\mathbf{r}_0$  is used as well. Assume that the detector is circularly symmetric about its center  $o'$ ; in this case, the weighting factor depends only on  $\theta'$ ,  $W(\mathbf{r}') = W(\theta')$ , where the angle  $\theta'$  between  $\mathbf{r}'_0$  and  $\mathbf{r}_0$ —the polar angle of  $\mathbf{r}'_0$  in the local coordinate system—varies from 0 to  $\Theta$  depending on the size of the detector. The azimuthal angle  $\phi'$  of  $\mathbf{r}'_0$  in the local coordinate system varies from 0 to  $2\pi$ . The normal of the detector surface at point  $o'$  is assumed to point to the center of the measurement geometry  $o$ . The surface integral in Eq. (3.15) can be transformed into an integral over a curve radiating from the center  $o'$  on the surface  $l'$  and the azimuthal

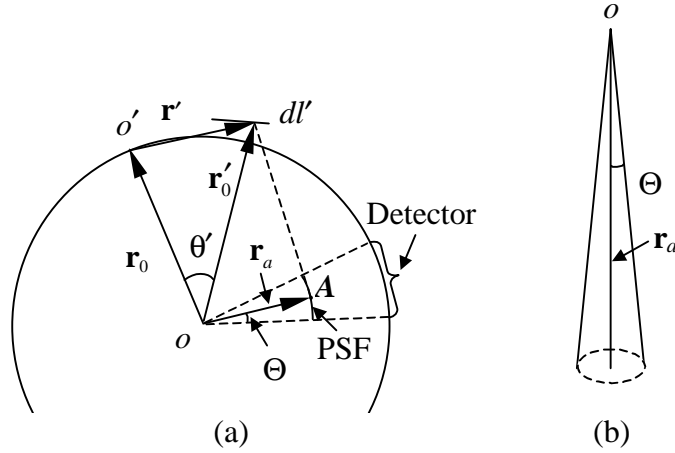


FIG. 3.6. (a) Diagram of the spherical measurement geometry:  $\theta'$  is the angle between  $\mathbf{r}_0$  and  $\mathbf{r}'_0$ ;  $dl'$  is an integral element on the detector surface;  $\Theta$  is the angle of the radius of the detector aperture to the measurement geometry origin  $o$ ; the extension of the PSF at point  $A$  is indicated; other denotations of the symbols are the same as in Figs. 3.1 and 3.3. (b) Perspective view of the lateral extension of the PSF's of all the point sources along a radial axis in the spherical measurement geometry.

angle  $\varphi'$ :

$$\begin{aligned}\tilde{p}'_d(\mathbf{r}_0, k) &= \int \int \tilde{p}(\mathbf{r}_0 + \mathbf{r}', k) W(\theta') r' \sqrt{1 - (\mathbf{n}_0 \cdot \mathbf{n}')^2} d\varphi' dl' \\ &= \int_{l'} W(\theta') \sqrt{1 - (\mathbf{n}_0 \cdot \mathbf{n}')^2} r' dl' \int_0^{2\pi} \tilde{p}(\mathbf{r}_0 + \mathbf{r}', k) d\varphi',\end{aligned}\quad (3.17)$$

where  $\mathbf{n}' = \mathbf{r}' / r'$  and

$$\tilde{p}(\mathbf{r}_0 + \mathbf{r}', k) = -ik \frac{\exp(ik|\mathbf{r}_a - \mathbf{r}_0 - \mathbf{r}'|)}{4\pi|\mathbf{r}_a - \mathbf{r}_0 - \mathbf{r}'|}. \quad (3.18)$$

Considering the expansion in the local spherical coordinates, and denoting  $\mathbf{n}'_0 = \mathbf{r}'_0 / r'_0$ ,

$\mathbf{n}'_0 = (\theta', \varphi')$ , and  $\mathbf{n}_a = (\theta'_a, \varphi'_a)$ , one obtains

$$\frac{\exp(ik|\mathbf{r}_a - \mathbf{r}'_0|)}{4\pi|\mathbf{r}_a - \mathbf{r}'_0|} = \frac{ik}{4\pi} \sum_{l=0}^{\infty} (2l+1) j_l(kr_a) h_l^{(1)}(kr'_0) P_l(\mathbf{n}_a \cdot \mathbf{n}'_0), \quad (3.19)$$

where  $P_l(\mathbf{n}_a \cdot \mathbf{n}'_0)$  can be expanded as [14]

$$\begin{aligned}P_l(\mathbf{n}_a \cdot \mathbf{n}'_0) &= P_l(\cos \theta'_a) P_l(\cos \theta') \\ &\quad + 2 \sum_{m=1}^l \frac{(l-m)!}{(l+m)!} P_l^m(\cos \theta'_a) P_l^m(\cos \theta') \cos[m(\varphi'_a - \varphi')].\end{aligned}\quad (3.20)$$

Then, one can evaluate the following integral

$$\int_0^{2\pi} P_l(\mathbf{n}_a \cdot \mathbf{n}'_0) d\varphi' = 2\pi P_l(\cos \theta') P_l(\cos \theta'_a). \quad (3.21)$$

Actually,  $\theta'_a$  is the angle between  $\mathbf{r}_0$  and  $\mathbf{r}_a$ , i.e.,  $\cos \theta'_a = \mathbf{n}_a \cdot \mathbf{n}_0$ .

Combining the results of Eqs. (3.19), (3.20), and (3.21), Eq. (3.17) can be rewritten as

$$\begin{aligned}\tilde{p}'_d(\mathbf{r}_0, k) &= \frac{k^2 c^2 \eta}{2} \int_{l'} W(\theta') \sqrt{1 - (\mathbf{n}_0 \cdot \mathbf{n}')^2} r' dl' \\ &\times \sum_{l=0}^{\infty} (2l+1) P_l(\cos \theta') P_l(\mathbf{n}_a \cdot \mathbf{n}_0) j_l(kr_a) h_l^{(1)}(kr'_0).\end{aligned}\quad (3.22)$$

By replacing  $p(\mathbf{r}_0, k)$  with  $\tilde{p}'_d(\mathbf{r}_0, k)$  in the reconstruction formula as Eq. (2.12)

shown in Chapter II:

$$p_0(\mathbf{r}) = \frac{1}{2\pi^2} \int_{\Omega_0} d\Omega_0 \int_0^{+\infty} dk \tilde{p}(\mathbf{r}_0, k) \sum_{l=0}^{\infty} \frac{(2l+1) j_l(kr)}{h_l^{(1)}(kr_0)} P_l(\mathbf{n} \cdot \mathbf{n}_0), \quad (3.23)$$

and considering the identity [24]:

$$\int_{\Omega_0} P_l(\mathbf{n}_a \cdot \mathbf{n}_0) P_m(\mathbf{n}_0 \cdot \mathbf{n}) = \frac{4\pi}{2l+1} \delta_{lm} P_l(\mathbf{n}_a \cdot \mathbf{n}), \quad (3.24)$$

we obtain the reconstruction for the point source as:

$$\begin{aligned}\text{PSF}_a(\mathbf{r}, \mathbf{r}_a) &= \frac{1}{\pi} \int_{l'} W(\theta') \sqrt{1 - (\mathbf{n}_0 \cdot \mathbf{n}')^2} r' dl' \\ &\times \sum_{m=0}^{\infty} (2m+1) P_m(\mathbf{n}_a \cdot \mathbf{n}) P_m(\cos \theta') \\ &\times \int_0^{+\infty} j_m(kr_a) j_m(kr) \frac{h_m^{(1)}(kr'_0)}{h_m^{(1)}(kr_0)} k^2 dk.\end{aligned}\quad (3.25)$$

Letting  $\tilde{\theta}$  and  $\tilde{\varphi}$  be the polar and azimuthal angles of vector  $\mathbf{n}$  with respect to vector  $\mathbf{n}_a$ , and using an identity similar to the one shown in Eq. (3.21), one can rewrite Eq. (3.25) as:

$$\begin{aligned}\text{PSF}_a(\mathbf{r}, \mathbf{r}_a) &= \int \int W(\theta') r' \sqrt{1 - (\mathbf{n}_0 \cdot \mathbf{n}')^2} d\varphi' dl' \times \frac{1}{2\pi^2} \sum_{m=0}^{\infty} (2m+1) P_m(\cos \tilde{\gamma}) \\ &\times \int_0^{+\infty} j_m(kr_a) j_m(kr) \frac{h_m^{(1)}(kr'_0)}{h_m^{(1)}(kr_0)} k^2 dk,\end{aligned}\quad (3.26)$$

where  $\cos \tilde{\gamma} = \cos \tilde{\theta} \cos \theta' + \sin \tilde{\theta} \sin \theta' \cos(\tilde{\varphi} - \varphi')$ .

## (a) Special spherical aperture

For simplicity, assume the detector is a small section of the spherical measurement surface, i.e.,  $r'_0 = |\mathbf{r}'_0| = |\mathbf{r}_0 + \mathbf{r}'| = |\mathbf{r}_0| = r_0$ . Therefore, one obtains

$$\sqrt{1 - (\mathbf{n}_0 \cdot \mathbf{n}')^2} r' dl' = r_0^2 \sin \theta' d\theta', \quad (3.27)$$

and

$$h_m^{(1)}(kr'_0)/h_m^{(1)}(kr_0) = 1. \quad (3.28)$$

Substituting the identities [24]:

$$\int_0^{+\infty} j_m(kr) j_m(kr_a) k^2 dk = \frac{\pi}{2r^2} \delta(r - r_a), \quad (3.29)$$

and

$$\sum_{m=0}^{\infty} (2m+1) P_m(\mathbf{n}_a \cdot \mathbf{n}) P_m(\cos \theta') = 2\delta(\cos \theta' - \mathbf{n}_a \cdot \mathbf{n}), \quad (3.30)$$

the following identity into Eq. (3.25), we obtain

$$\text{PSF}_a(\mathbf{r}, \mathbf{r}_a) = \frac{r_0^2}{r^2} \delta(r - r_a) \int_0^{\Theta} \sin \theta' W(\theta') d\theta' \delta(\cos \theta' - \mathbf{n}_a \cdot \mathbf{n}). \quad (3.31)$$

Letting  $\gamma$  be the angle between  $\mathbf{n}_a$  and  $\mathbf{n}$ , i.e.,  $\mathbf{n}_a \cdot \mathbf{n} = \cos \gamma$ ,

$$\begin{aligned} \text{PSF}_a(\mathbf{r}, \mathbf{r}_a) &= \frac{r_0^2}{r^2} \delta(r - r_a) \int_0^{\Theta} \sin \theta' W(\theta') d\theta' \delta(\cos \theta' - \cos \gamma) \\ &= \frac{r_0^2}{r^2} \delta(r - r_a) W(\gamma). \end{aligned} \quad (3.32)$$

If letting  $W(\theta') = 1$ ,

$$\text{PSF}_a(\mathbf{r}, \mathbf{r}_a) = \frac{r_0^2}{r^2} \delta(r - r_a) [U(\gamma) - U(\gamma - \Theta)], \quad (3.33)$$

where  $U$  is the step function,  $U(x) = 1$  when  $x > 0$  and  $U(x) = 0$  when  $x < 0$ .

Equation (3.33) indicates that, in this special case, the PSF only extends along the lateral direction, which is proportional to the solid angle of the detector aperture to the origin of the measurement geometry. The perspective view of the lateral extension of all the points in a radial axis looks like a cone as shown in Fig. 3.6(b). The farther the point source is away from the origin, the more extension the PSF has. Therefore, the lateral resolution is worse when the point is close to the detector. But, a lateral resolution superior to the aperture size can still be achieved if the object under study is close to the center of the geometry.

(b). Small flat aperture

Now, let us consider flat apertures. Sometimes, a set of small flat detectors is used to form a spherical measurement surface. Suppose the detector aperture is disk-like and its radius is  $P$ . Since  $\mathbf{n}_0 \cdot \mathbf{n}' = 0$  in this case,

$$\sqrt{1 - (\mathbf{n}_0 \cdot \mathbf{n}')^2} r' dl' = r' dr', \quad (3.34)$$

where  $r' = r_0 \tan \theta'$ . If the aperture is small relative to the radius of the detection surface, i.e.,  $r' \leq P \ll r_0$ , the following approximation holds:

$$r'_0 - r_0 = \sqrt{r_0^2 + r'^2} - r_0 \approx \frac{r'^2}{2r_0}. \quad (3.35)$$

Neglecting the second-order and higher small quantities, one can approximate  $h_m^{(1)}(kr'_0)/h_m^{(1)}(kr_0) \approx 1$ . Then, one can follow the derivation for the special spherical aperture and obtain

$$\text{PSF}_a(\mathbf{r}, \mathbf{r}_a) = \frac{1}{r^2} \delta(r - r_a) \int_0^P W(r') r' dr' \delta(\cos \theta' - \mathbf{n}_a \cdot \mathbf{n}). \quad (3.36)$$

Letting  $W(r') = 1$  and approximating  $r = r_0 \tan \theta' \approx r_0 \theta'$  for the small aperture case, one reaches

$$\begin{aligned} \text{PSF}_a(\mathbf{r}, \mathbf{r}_a) &\approx \frac{r_0^2}{r^2} \delta(r - r_a) \int_0^{P/r_0} \theta' \frac{\delta(\theta' - \gamma)}{\sin \theta'} d\theta' \\ &= \frac{r_0^2}{r^2} \delta(r - r_a) \int_0^{P/r_0} \delta(\theta' - \gamma) d\theta' \\ &= \frac{r_0^2}{r^2} \delta(r - r_a) [U(\gamma) - U(\gamma - P/r_0)]. \end{aligned} \quad (3.37)$$

Equation (3.37) indicates that, for the small flat aperture, the extension of the PSF is primarily along the lateral axis. In fact, if we substitute  $\Theta$  for  $P/r_0$ , Eq. (3.37) becomes identical to Eq. (3.33) for the special spherical aperture.

Particularly, at the center of the measurement geometry, i.e.,  $r_a = 0$ , we have

$$j_m(0) = \delta_{m0}, \quad P_0(\cdot) = 1, \quad \text{and} \quad h_0^{(1)}(kr) = -i \exp(ikr)/(kr). \quad \text{Assuming } W(r') = 1, \text{ Eq. (3.25)}$$

reduces to

$$\text{PSF}_a(\mathbf{r}, \mathbf{r}_a) = \frac{1}{\pi} \int_0^{+\infty} j_0(kr) \exp(-ikr_0) k^2 dk \int_0^P \frac{r_0}{r'_0} r' dr' \exp(ikr'_0). \quad (3.38)$$

Using the relation  $r'_0 = \sqrt{r_0^2 + r'^2}$ , one can simplify Eq. (3.38) to



$$\text{PSF}_a(\mathbf{r}, \mathbf{r}_a) = \frac{1}{\pi} \int_0^{+\infty} j_0(kr) k^2 dk \frac{r_0 [\exp(ik\sqrt{P^2 + r_0^2} - ikr_0) - 1]}{ik}. \quad (3.39)$$

Because  $P \ll r_0$ , the imaginary part is much less than the real part and hence can be neglected; as a result, one can obtain

$$\text{PSF}_a(\mathbf{r}, \mathbf{r}_a) \approx \frac{r_0}{\pi} \int_0^{+\infty} j_0(kr) \sin[k(\sqrt{P^2 + r_0^2} - r_0)] k dk. \quad (3.40)$$

Using the following identity [24],

$$\begin{aligned} \int_0^{+\infty} j_0(ka) \sin(kb) k dk &= b \int_0^{+\infty} j_0(ka) j_0(kb) k^2 dk \\ &= \frac{\pi}{2b} \delta(b - a), \end{aligned} \quad (3.41)$$

in the small-aperture case, i.e.,  $P \ll r_0$ , Eq. (3.40) reduces to

$$\text{PSF}_a(\mathbf{r}, \mathbf{r}_a) = \frac{r_0^2}{P^2} \delta(r - \frac{P^2}{2r_0}). \quad (3.42)$$

Equation (3.40) indicates that the point source at the center becomes a circle with a diameter  $P^2/r_0$ .

Next, we want to estimate the lateral extension at an arbitrary point. Taking the asymptotic form of the Hankel function to approximate

$$\begin{aligned} \frac{h_m^{(1)}(kr'_0)}{h_m^{(1)}(kr_0)} &\approx \frac{\exp(ikr'_0)/(kr'_0)}{\exp(ikr_0)/(kr_0)} \\ &= \frac{r_0}{r'_0} \exp(ikr'_0 - ikr_0), \end{aligned} \quad (3.43)$$

one can rewrite Eq. (3.25) as

$$\begin{aligned} \text{PSF}_a(\mathbf{r}, \mathbf{r}_a) &= \frac{1}{\pi} \int_0^P W(r') r' dr' \int_0^{+\infty} \frac{r_0}{r'_0} \exp(ikr'_0 - ikr_0) k^2 dk \\ &\times \sum_{m=0}^{\infty} (2m+1) P_m(\mathbf{n}_a \cdot \mathbf{n}) P_m(\cos \theta') j_m(kr_a) j_m(kr). \end{aligned} \quad (3.44)$$

The above integral is still complicated. Here, we consider only the spread along  $\mathbf{r}_a$  with the assumption of  $W(r') = 1$ . Substituting  $P_m(\mathbf{n}_a \cdot \mathbf{n}) = P_m(1) = 1$  into Eq. (3.44) and considering the identity [79]:

$$\sum_{m=0}^{\infty} (2m+1) P_m(\mathbf{n}_a \cdot \mathbf{n}) j_m(kr_a) j_m(kr) = \frac{\sin(kR)}{kR} = j_0(kR), \quad (3.45)$$

and further approximating  $j_0(k\sqrt{r_a^2 + r^2 - 2r_a r \cos \theta'}) \approx j_0(k|r - r_a|)$  for the small-aperture case ( $r' \ll r_0$ , i.e.,  $\theta' \ll 1$ ), one obtains

$$\text{PSF}_a(r\mathbf{n}_a, \mathbf{r}_a) = \frac{1}{\pi} \int_0^{+\infty} j_0(k|r - r_a|) \exp(-ikr_0) k^2 dk \int_0^P \frac{r_0}{r'_0} r' dr' \exp(ikr'_0). \quad (3.46)$$

If we substitute  $|r - r_a|$  for  $r$ , Eq. (3.46) becomes identical to Eq. (3.38). Thus, in the small-aperture case ( $P \ll r_0$ ), Eq. (3.46) reduces to Eq. (3.42) with the replacement of  $r$  by  $|r - r_a|$ :

$$\text{PSF}_a(r\mathbf{n}_a, \mathbf{r}_a) \approx \frac{r_0^2}{P^2} \delta\left(|r - r_a| - \frac{P^2}{2r_0}\right). \quad (3.47)$$

Equation (3.47) indicates that the point source at which  $\mathbf{r}_a$  extends in the radial direction to a region with diameter  $P^2/r_0$  is the same as the extension of the PSF at the recoding geometry center as shown in Eq. (3.42). But, in most cases, this extension is negligible. For example, when using a transducer with even a 6 mm diameter to image a

10-cm-size breast on a measurement geometry surface with a 15-cm diameter,  $P^2/r_0 = 3^2/150 = 0.06 \text{ mm}$ . However, the lateral extension at  $r$  is on the order of  $2rP/r_0$  as shown in Eq. (3.37). For example, even at  $r = 1 \text{ cm}$ ,  $2rP/r_0 = (2)(10)(3)/150 = 0.4 \text{ mm} > 0.06 \text{ mm}$ .

## 2. Planar geometry

In this case, we reasonably assume that the detector surface is flat. As shown in Fig. 3.7(a),  $\mathbf{r}_0$  represents the center of the detector  $o'$  in the global Cartesian coordinates  $(x, y, z)$  with the origin at the measurement geometry center  $o$ . Let  $x'$ ,  $y'$  and  $z'$  be the differences of the coordinates between  $\mathbf{r}'_0$  and  $\mathbf{r}_0$ , respectively. For the following two linear translations:

$$\mathbf{r}_0 \rightarrow \mathbf{r}'_0: x_0 \rightarrow x_0 + x' = x'_0, y_0 \rightarrow y_0 + y' = y'_0, \quad (3.48)$$

$$\mathbf{r}_a \rightarrow \mathbf{r}'_a: x_a \rightarrow x_a - x' = x'_a, y_a \rightarrow y_a - y' = y'_a, \quad (3.49)$$

there exist the following translational invariances:  $|\mathbf{r}_a - \mathbf{r}'_0| = |\mathbf{r}'_a - \mathbf{r}_0|$ .

The detected signal at  $\mathbf{r}_0$  can be written as

$$\begin{aligned} \tilde{p}'_d(\mathbf{r}_0, k) &= \iint W(\mathbf{r}') \tilde{p}(\mathbf{r}_0 + \mathbf{r}', k) d^2 \mathbf{r}' \\ &= \iint W(x', y') \tilde{p}(x_0 + x', y_0 + y', k) dx' dy'. \end{aligned} \quad (3.50)$$

Using  $\tilde{p}'_d(\mathbf{r}_0, k)$  to replace  $p(\mathbf{r}_0, k)$  in the reconstruction formula Eq. (2.30) shown in Chapter II:

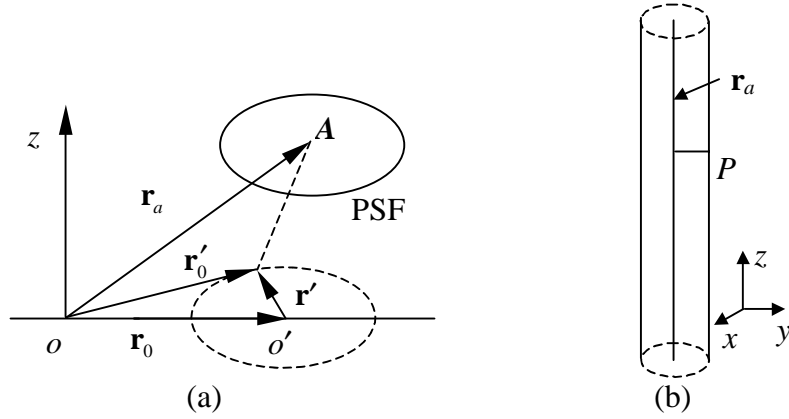


FIG. 3.7. (a) Diagram of the planar measurement geometry:  $P$  is the radius of the detector aperture; the extension of the PSF at point  $A$  is indicated; other denotations of the symbols are the same as in Figs. 3.1 and 3.5; (b) Perspective view of the lateral extension of the PSF's of all the point sources along a line parallel with the  $z$ -axis in the planar measurement geometry.

$$\begin{aligned}
 p_0(\mathbf{r}) &= \frac{1}{4\pi^3} \int \int_{-\infty}^{+\infty} dx_0 dy_0 \int_{-\infty}^{+\infty} dk \tilde{p}(\mathbf{r}_0, k) \\
 &\times \int \int_{-\infty}^{+\infty} du dv \exp[-iu(x-x_0)] \exp[-iv(y-y_0)] \\
 &\times \text{rect}\left(\frac{\rho}{2k}\right) \exp[-iz \text{sgn}(k) \sqrt{k^2 - \rho^2}],
 \end{aligned} \tag{3.51}$$

where  $\rho = \sqrt{u^2 + v^2}$ , we get the reconstruction for the point source as:

$$\begin{aligned}
 \text{PSF}_a(\mathbf{r}, \mathbf{r}_a) &= \int \int W(x', y') \delta(x - x'_a) \delta(y - y'_a) \delta(z - z_a) dx' dy' \\
 &= \int \int W(x', y') \delta(x - x_a + x') \delta(y - y_a + y') \delta(z - z_a) dx' dy',
 \end{aligned} \tag{3.52}$$

i.e.,

$$\text{PSF}_a(\mathbf{r}, \mathbf{r}_a) = W(x - x_a, y - y_a) \delta(z - z_a). \tag{3.53}$$

Supposing the detector surface is a disk with radius  $P$ , and  $W(x', y') = 1$  when

$\sqrt{x'^2 + y'^2} < P$ , Eq. (3.53) reduces to

$$\text{PSF}_a(\mathbf{r}, \mathbf{r}_a) = U(P - D)\delta(\Delta z), \quad (3.54)$$

where  $D = \sqrt{(\Delta x)^2 + (\Delta y)^2}$ , and  $\Delta x = x - x_a$ , etc.

Equation (3.54) indicates that without considering the bandwidth, the PSF does not extend along the axial direction, but it greatly extends in the lateral direction. Moreover, the lateral extension is proportional to the detector aperture. The perspective view of the lateral extension of all the PSF's in a line parallel with the  $z$ -axis looks like a cylinder as shown in Fig. 3.7(b). Therefore, the lateral resolution is totally blurred by the detector aperture, no matter where the point is.

### 3. Cylindrical geometry

#### (a). Special cylindrical aperture

We first suppose the detector surface is a section of the cylindrical measurement surface. As shown in Fig. 3.8(a),  $\mathbf{r}_0$  represents the center of the detector  $o'$  in the global cylindrical coordinates  $(\rho, \phi, z)$  with the origin at the measurement geometry center  $o$ . Let  $\phi'$  be the difference between the polar angles of  $\mathbf{r}_0$  and  $\mathbf{r}'_0$ , and  $\rho'$  and  $z'$  be the projections of  $\mathbf{r}'$  in the  $x$ - $y$  plane and the  $z$ -axis, respectively. Two sides of the detector are along the  $z$ -axis from  $-Z$  to  $Z$ , and the other two sides are parallel with the  $x$ - $y$  plane and the polar angle  $\phi'$  varies from  $-\Phi$  to  $\Phi$ . For the following two translations:

$$\mathbf{r}_0 \rightarrow \mathbf{r}'_0: \phi_0 \rightarrow \phi_0 + \phi' = \phi'_0, \quad z_0 \rightarrow z_0 + z' = z'_0, \quad (3.55)$$

$$\mathbf{r}_a \rightarrow \mathbf{r}'_a: \phi_a \rightarrow \phi_a - \phi' = \phi'_a, \quad z_a \rightarrow z_a - z' = z'_a, \quad (3.56)$$



$$\begin{aligned}
p_0(\mathbf{r}) = & \frac{1}{2\pi^3 \rho_0} \int_0^{2\pi} d\varphi_0 \int_{-\infty}^{+\infty} dz_0 \int_0^{+\infty} dk \tilde{p}(\mathbf{r}_0, k) \\
& \times \int_{-k}^{+k} d\gamma \exp[i\gamma(z_0 - z)] \\
& \times \sum_{n=-\infty}^{+\infty} \exp[in(\varphi_0 - \varphi)] \frac{J_n(\rho \sqrt{k^2 - \gamma^2})}{H_n^{(1)}(\rho_0 k^2 - \gamma^2)},
\end{aligned} \tag{3.58}$$

we get the reconstruction for the point source as:

$$\begin{aligned}
\text{PSF}_a(\mathbf{r}, \mathbf{r}_a) = & \int \int \frac{1}{\rho} \delta(\rho - \rho_a) \delta(\varphi - \varphi'_a) \delta(z - z'_a) W(\varphi', z') \rho_0 d\varphi' dz' \\
= & \frac{\rho_0}{\rho} \delta(\rho - \rho_a) \int \int \delta(\varphi - \varphi_a + \varphi') \delta(z - z_a + z') W(\varphi', z') d\varphi' dz',
\end{aligned} \tag{3.59}$$

i.e.,

$$\text{PSF}_a(\mathbf{r}, \mathbf{r}_a) = \frac{\rho_0}{\rho} \delta(\rho - \rho_a) W(\varphi - \varphi_a, z - z_a). \tag{3.60}$$

If  $W(\varphi', z') = 1$ ,  $\varphi'$  from  $-\Phi$  to  $\Phi$  and  $z'$  from  $-Z$  to  $Z$ , Eq. (3.60) can be rewritten as

$$\text{PSF}_a(\mathbf{r}, \mathbf{r}_a) = \frac{\rho_0}{\rho} \delta(\rho - \rho_a) U(\Phi - |\varphi - \varphi_a|) U(Z - |z - z_a|). \tag{3.61}$$

Equation (3.61) indicates that the extension of the PSF in the cylindrical geometry combines the properties of the PSF's in the spherical and planar geometries. In this special case, the PSF does not extend along the radial direction. The perspective view of the lateral extension of all the point sources in a radial axis looks like a piece of cake as shown in Fig. 3.8(b). In the  $z$ -axis direction, the PSF extension is proportional to the detector size along the  $z$ -axis, just like the planar geometry. While parallel with the  $x$ - $y$  plane, the lateral extension is proportional to the angle of the detector width to the  $z$ -axis, just like in the spherical case. Therefore, a lateral resolution that is better than the

aperture size can be obtained parallel to the  $x$ - $y$  plane if the object under study is close to the center of the geometry; however, the lateral resolution along the  $z$ -axis is determined by the detector size.

(b). Small rectangular aperture

Sometimes a set of small rectangular detectors is used to form a cylindrical array. The normal of the detector at the center point  $o'$  is assumed to point to the center of the measurement geometry. Two sides of the detector are along the  $z$ -axis from  $-Z$  to  $Z$ , and the other two sides are parallel with the  $x$ - $y$  plane and have a length of  $2P$ . One can follow the similar derivation in Section III I, and get the reconstruction for the point source as

$$\begin{aligned} \text{PSF}_a(\mathbf{r}, \mathbf{r}_a) = & \frac{1}{2\pi} \int_{-Z}^Z \delta(z_a - z - z') dz' \int_{-P}^{+P} d\rho' W(\varphi', z') \sum_{m=-\infty}^{+\infty} \exp[im(\varphi_a - \varphi - \varphi')] \\ & \times \int_0^{+\infty} \mu d\mu J_m(\mu \rho_a) J_m(\mu \rho) \frac{H_m^{(1)}(\mu \sqrt{\rho_0^2 + \rho'^2})}{H_m^{(1)}(\mu \rho_0)}, \end{aligned} \quad (3.62)$$

where  $\rho' = \rho_0 \tan \varphi'$ . Let  $W(\varphi', z') = 1$ .

For the small aperture case,  $\rho' \ll \rho_0$ , one can approximate

$$\frac{H_m^{(1)}(\mu \sqrt{\rho_0^2 + \rho'^2})}{H_m^{(1)}(\mu \rho_0)} \approx 1. \quad (3.63)$$

Further, taking the small aperture approximation:  $\rho' = \rho_0 \tan \varphi' \approx \rho_0 \varphi'$ , and considering the following identity [24],



$$\int_0^{+\infty} \mu d\mu J_m(\mu \rho_a) J_m(\mu \rho) = \frac{1}{\rho} \delta(\rho - \rho_a), \quad (3.64)$$

one can rewrite Eq. (3.62) as

$$\text{PSF}_a(\mathbf{r}, \mathbf{r}_a) = U(Z - |z - z_a|) \frac{1}{\rho} \delta(\rho - \rho_a) \int_{-P/\rho_0}^{+P/\rho_0} \rho_0 d\phi' \delta(\phi_a - \phi - \phi'), \quad (3.65)$$

i.e.,

$$\text{PSF}_a(\mathbf{r}, \mathbf{r}_a) = \frac{\rho_0}{\rho} \delta(\rho - \rho_a) U\left(\frac{P}{\rho_0} - |\phi - \phi_a|\right) U(Z - |z - z_a|). \quad (3.66)$$

Equation (3.66) indicates that, for the small flat aperture, the extension of the PSF is primarily along the lateral axis. In fact, if we substitute  $\Phi$  for  $P/\rho_0$ , Eq. (3.66) becomes identical to Eq. (3.61) in the special cylinder aperture case.

Next, we want to estimate the lateral extension of the PSF. One can also take the asymptotic form of the Hankel function to approximate

$$\frac{H_m^{(1)}(\mu \sqrt{\rho_0^2 + \rho'^2})}{H_m^{(1)}(\mu \rho_0)} \approx \exp[i\mu(\sqrt{\rho_0^2 + \rho'^2} - \rho_0)], \quad (3.67)$$

and then rewrite Eq. (3.62) as

$$\begin{aligned} \text{PSF}_a(\mathbf{r}, \mathbf{r}_a) &= \frac{1}{2\pi} U(Z - |z - z_a|) \int_0^{+\infty} \mu d\mu \int_{-P}^{+P} d\rho' \exp[i\mu(\sqrt{\rho_0^2 + \rho'^2} - \rho_0)] \\ &\quad \times \sum_{m=-\infty}^{+\infty} J_m(\mu \rho_a) J_m(\mu \rho) \exp[im(\phi_a - \phi - \phi')]. \end{aligned} \quad (3.68)$$

Considering the identity [79]

$$\sum_{m=-\infty}^{+\infty} \exp[im(\phi_a - \phi)] J_m(\mu \rho_a) J_m(\mu \rho) = J_0(\mu D), \quad (3.69)$$

Eq. (3.68) can be rewritten as

$$\begin{aligned} \text{PSF}_a(\mathbf{r}, \mathbf{r}_a) = & \frac{1}{2\pi} U(Z - |z - z_a|) \int_0^{+\infty} \mu d\mu \int_{-P}^{+P} d\rho' \exp[i\mu(\sqrt{\rho_0^2 + \rho'^2} - \rho_0)] \\ & \times J_0[\mu\sqrt{\rho_a^2 + \rho^2 - 2\rho_a\rho\cos(\varphi_a - \varphi - \varphi')}] . \end{aligned} \quad (3.70)$$

Equation (3.70) is still complicated. Here, by only considering the points along  $\mathbf{r}_a$ , i.e., letting  $\varphi = \varphi_a$ , and then taking the small aperture approximation ( $\varphi' \ll 1$ ),

$$J_0[\mu\sqrt{\rho_a^2 + \rho^2 - 2\rho_a\rho\cos(\varphi_a - \varphi - \varphi')}] \approx J_0(\mu|\rho - \rho_a|), \quad (3.71)$$

and

$$\sqrt{\rho_0^2 + \rho'^2} - \rho_0 \approx \frac{\rho'^2}{2\rho_0}, \quad (3.72)$$

one can rewrite Eq. (3.70) as

$$\begin{aligned} \text{PSF}_a[(\rho, \varphi_a, z), \mathbf{r}_a] = & U(Z - |z - z_a|) \int_{-P}^{+P} d\rho' \\ & \times \int_0^{+\infty} \mu d\mu J_0(\mu|\rho - \rho_a|) \exp(i\mu\rho'^2/2\rho_0). \end{aligned} \quad (3.73)$$

Because  $\rho' \ll \rho_0$ , the imaginary part is much less than the real part and hence can be neglected,

$$\begin{aligned} & \text{PSF}_a[(\rho, \varphi_a, z), \mathbf{r}_a] \\ = & U(Z - |z - z_a|) \int_{-P}^{+P} d\rho' \int_0^{+\infty} \mu d\mu J_0(\mu|\rho - \rho_a|) \cos(\mu\rho'^2/2\rho_0) \\ = & U(Z - |z - z_a|) \int_{-P}^{+P} d\rho' \left(\frac{\rho_0}{\rho'}\right) \frac{\partial}{\partial \rho'} \int_0^{+\infty} d\mu J_0(\mu|\rho - \rho_a|) \sin(\mu\rho'^2/2\rho_0). \end{aligned} \quad (3.74)$$

Using the following identity [15]

$$\int_0^{+\infty} dt J_0(ta) \sin(tb) = \begin{cases} \frac{1}{\sqrt{b^2 - a^2}}, & 0 < a < b, \\ 0, & \text{otherwise,} \end{cases} \quad (3.75)$$

one can get the integral in Eq. (3.74)

$$\begin{aligned}
& \int_{-P}^{+P} d\rho' \left( \frac{\rho_0}{\rho'} \right) \frac{\partial}{\partial \rho'} \left[ \sqrt{(\rho'^2/2\rho_0)^2 - |\rho - \rho_a|^2} \right]^{-1} \\
&= \left( \frac{\rho_0}{\rho'} \right) \left[ \sqrt{(\rho'^2/2\rho_0)^2 - |\rho - \rho_a|^2} \right]^{-1} \Big|_{-P}^P \\
&- \int_{-P}^{+P} \left[ \sqrt{(\rho'^2/2\rho_0)^2 - |\rho - \rho_a|^2} \right]^{-1} d\left( \frac{\rho_0}{\rho'} \right).
\end{aligned} \tag{3.76}$$

The integral of Eq. (3.76) only exists in the range:  $(P^2/2\rho_0) > |\rho - \rho_a|$ . Therefore, the PSF extends to a region with a diameter  $P^2/\rho_0$ , which is negligible compared with the lateral extension as we discussed in the spherical geometry explanation.

So far, we have derived the analytic PSF's due to the detector apertures for the specific spherical, planar and cylindrical measurement geometries. The explicit expressions can be given when the detector surfaces are assumed to have the same geometric properties as the measurement geometries. Otherwise, it appears that explicitly carrying out the analytic derivations is impossible. But, in reality, the detector aperture is very small compared with the measurement surface. We have also estimated axial extension in this case and found it was negligible compared to lateral extension.

#### ***4. Combined effects***

Finally, we attempt to analyze the combined effects of bandwidth and detector size together. Suppose the detected signal is band-limited, characterized by  $\tilde{H}(k)$  with a cutoff frequency  $k_c$ , and the detectors have the same geometries as the measurement surfaces. One can then follow the derivations in Sections 2 and 3 and reach the following results:

(a) Spherical geometry:

$$\text{PSF}_{ba}(\mathbf{r}) = \int \int W(\theta') \text{PSF}_b(R') r_0^2 \sin \theta' d\theta' d\phi' \quad (3.77)$$

where  $R' = \sqrt{r^2 + r_a^2 - 2rr_a \cos \tilde{\gamma}}$ ,  $\cos \tilde{\gamma} = \cos \tilde{\theta} \cos \theta' + \sin \tilde{\theta} \sin \theta' \cos(\tilde{\phi} - \phi')$ , and  $\tilde{\theta}$  and  $\tilde{\phi}$  are the polar and azimuthal angles of vector  $\mathbf{n}$  with respect to vector  $\mathbf{n}_a$ , respectively.

(b) Planar geometry:

$$\text{PSF}_{ba}(x, y, z) = \int \int W(x', y') \text{PSF}_b(R') dx' dy', \quad (3.78)$$

where  $R' = \sqrt{(x - x_a + x')^2 + (y - y_a + y')^2 + (z - z_a)^2}$ ,

(c) Cylindrical geometry:

$$\text{PSF}_{ba}(\rho, \phi, z) = \int \int W(\phi', z') \text{PSF}_b(R') \rho_0 d\phi' dz', \quad (3.79)$$

where  $R' = \sqrt{\rho^2 + \rho_a^2 - 2\rho\rho_a \cos(\phi - \phi_a + \phi') + (z - z_a + z')^2}$ .

Equations (3.77), (3.78) and (3.79) clearly reveal that the PSF can be regarded as a convolution of the detector aperture with the space-invariant  $\text{PSF}_b$ . However, in the spherical geometry case, the convolution becomes complicated as shown in Eq. (3.77). Further, we can imagine how complicated the convolution could be with an arbitrary measurement geometry using arbitrary-aperture detectors.

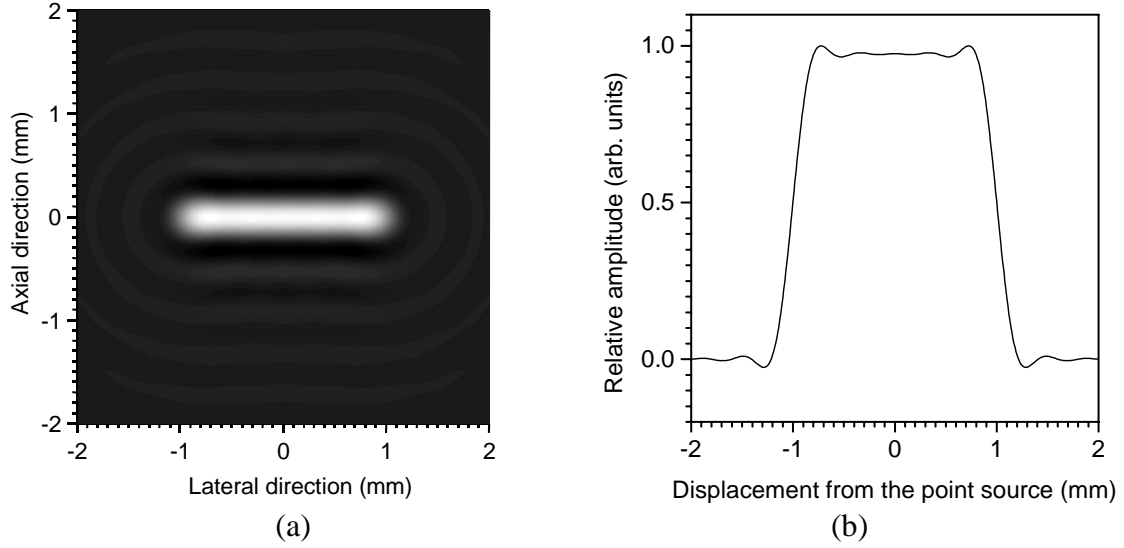


FIG. 3.9. An example of the PSF due to the detector aperture: (a) a grayscale view and (b) a lateral profile through the point source

Let us take the PSF in the planar geometry case as an example, which is shown in Fig. 3.9. The detector aperture is assumed to be a disk with a radius of 1 mm and a cutoff frequency  $f_c = 4$  MHz. In the axial direction, the extension of the PSF is similar to that shown in Fig. 3.2(b), which is determined by the bandwidth. However, as shown Fig. 3.9(b), the PSF greatly expands in the lateral direction; and its corresponding FWHM  $\approx 2$  mm, which is physically limited by the detector size.

#### D. Summary

We have proved that the PSF as a function of bandwidth is space-invariant for any measurement geometry when the reconstruction is linear and exact. The bandwidth limits the obtainable spatial resolution. We have also demonstrated that the finite aperture of the detector extends the PSF for different measurement geometries. The

detector aperture blurs lateral resolution greatly at different levels for different measurement geometries but the effect on axial resolution is slight. The results offer clear instruction for designing appropriate photoacoustic imaging systems with predefined spatial resolutions.

## **CHAPTER IV**

### **SAMPLING STRATEGY**

#### **A. Introduction**

Photoacoustic computed tomography is based on measurement of the outgoing acoustic waves emitted from the initial PA source. The measurement is performed by scanning wideband acoustic transducers around the sample under investigation. Each temporal PA signal, measured at various detection positions, provides one-dimensional (1D) depth, or radial, information about the acoustic source, while two-dimensional (2D) surface scans offer other 2D lateral information about the acoustic source. A combination of the temporal and spatial measurements may afford sufficient information for a complete reconstruction of a three-dimensional (3D) PA source.

For computer-based reconstructions, the PA signals must be discretely sampled in both space and time. In reality, the outgoing PA waves are acquired around the initial PA source at a series of discrete spatial detection positions on the measurement surface with a spatial sampling frequency (i.e., the inverse of the sampling period); and at each detection position, a series of discrete temporal points is sampled with a temporal sampling frequency.

According to the sampling (Nyquist) theorem, to accurately reconstruct a signal from a periodically sampled version of it, the sampling frequency must be at least twice the maximum frequency of the signal. Otherwise, a phenomenon known as aliasing is introduced, which causes confusion and serious measurement errors because the high-

frequency components above half the sampling frequency disguise themselves as low-frequency components in the discretely sampled data [80].

Therefore, if the spatial-sampling period is not sufficient, aliasing artifacts will be introduced in the measured data. However, a smaller spatial-sampling period means more data acquisition positions, which may tremendously increase the amount of raw data for reconstruction as well as the data acquisition time if the measurement is performed by scanning a single detector or a small number of them. Therefore, it is desirable to know the optimal spatial-sampling period for PA measurement, but, so far, no sampling strategy for the PA measurement has been proposed.

In the sampling of temporal signals, an analog anti-aliasing filter is often applied prior to the analog-to-digital (A/D) converter, which filters out frequency information that is higher than half the temporal sampling frequency. In a surface scan, however, the sampling of the positions is dependent on the measurement geometries.

In this chapter, we first present a theoretical analysis of spatial sampling in PA measurement for various measurement geometries, including spherical, planar, and cylindrical surfaces. Then, based on the sampling theorem, we propose an optimal sampling strategy for PA measurement. Optimal spatial sampling periods for different geometries are derived. The aliasing effects on the PAT images in the different geometries are also discussed. At last, we conduct numerical simulations to test the proposed optimal sampling strategy and also to demonstrate how the aliasing related to spatially discrete sampling affects the PAT image.



## B. Optimal sampling strategy

From a physical point of view, the measurement is to collect the Fourier component  $\tilde{p}_0(\mathbf{k})$  of the spatial source  $p_0(\mathbf{r})$ , where the Fourier transform is defined by

$$\tilde{p}_0(\mathbf{k}) = \int \int \int_{\mathbf{r}} p_0(\mathbf{r}) \exp(i\mathbf{k} \cdot \mathbf{r}) d^3\mathbf{r}, \quad (4.1)$$

and the inverse transform is

$$p_0(\mathbf{r}) = \frac{1}{(2\pi)^3} \int \int \int_{\mathbf{k}} \tilde{p}_0(\mathbf{k}) \exp(-i\mathbf{k} \cdot \mathbf{r}) d^3\mathbf{k}. \quad (4.2)$$

Since the PA measurement system is linear, the measurement of  $\tilde{p}_0(\mathbf{k})$  can be written as

$$\tilde{p}_d(\mathbf{k}) = \tilde{B}(\mathbf{k}) \tilde{p}_0(\mathbf{k}), \quad (4.3)$$

where  $\tilde{B}(\mathbf{k})$  is a system-dependent constant. If  $\tilde{B}(\mathbf{k})$  is not band-limited,  $\tilde{p}_0(\mathbf{k})$  could be perfectly recovered from the measurement  $\tilde{p}_d(\mathbf{k})$ .

However, in the actual measurement,  $\tilde{B}(\mathbf{k})$  is band-limited. As discussed in Chapter III, the real signal detected at position  $\mathbf{r}_0$  can be expressed as the convolution of the surface integral over the aperture of the detector and the impulse response of the data acquisition system:

$$\tilde{p}'_d(\mathbf{r}_0, k) = \tilde{H}(k) \int \int_{\mathbf{r}'} d^2\mathbf{r}' W(\mathbf{r}') \tilde{p}_d(\mathbf{r}_0 + \mathbf{r}', k), \quad (4.4)$$

where  $\mathbf{r}'$  points to an element on the surface of the detector with respect to the position of the detector  $\mathbf{r}_0$ ;  $W(\mathbf{r}')$  is a weighting factor that represents the contribution from the various surface elements of the detector to the total signal received by the detector; and

$\tilde{H}(k)$  is the Fourier transform of  $H(t) = I_e(t) \otimes I_d(t)$ , in which  $I_e(t)$  and  $I_d(t)$  are the temporal illumination function and the impulse response of the detector, respectively.

Obviously, the function  $\tilde{H}(k)$  works as a low-pass temporal-frequency filter that limits the temporal-frequency bandwidth of the measured PA signals, while  $W(\mathbf{r}')$  acts as a low-pass spatial-frequency filter that restricts the spatial-frequency bandwidth of the data. The high-frequency information beyond these bandwidths is filtered out in the measurement.

As discussed in the introduction, to accurately measure the signal in a finite bandwidth, the sampling frequency must be no less than the Nyquist frequency. In the sampling of temporal signals, it is straightforward to find out the Nyquist frequency. Assume  $\tilde{H}(k)$  has a rectangular-shaped bandwidth with a cutoff frequency of  $f_c$ . Then, the temporal Nyquist sampling frequency equals  $2f_c$ . Actually, in the measurement instrument, an anti-aliasing filter (low-pass filter) is often applied prior to the A/D converter to avoid aliasing. In a 2D surface scan, the spatial sampling is dependent on the measurement geometry. In the following three sections, we investigate three measurement geometries, including planar, spherical and cylindrical surfaces, respectively.

### 1. Planar geometry

The Cartesian coordinates are used in this case. We denote  $\mathbf{k} = (u, v, w)$  and  $\mathbf{r} = (x, y, z)$ . Assume the measurement surface is the  $z = 0$  plane and the sample lies above this plane.

First, we consider the idealized measurement condition. Taking the 2D Fourier transforms of  $\tilde{p}_d(\mathbf{r}_0, k)$  on spatial variables  $x_0$  and  $y_0$  gives

$$\tilde{q}_d(u, v, k) = \int \int_{-\infty}^{+\infty} \tilde{p}_d(x_0, y_0, k) \exp(iux_0 + ivy_0) dx_0 dy_0. \quad (4.5)$$

Then, from the Fourier-domain reconstruction formula Eq. (2.30), we find the relationship between the Fourier spectrum  $\tilde{q}_d(u, v, k)$  of the measurement and the Fourier spectrum  $\tilde{p}_0(u, v, w)$  of the source as:

$$\tilde{q}_d(u, v, k) = \frac{1}{2} \frac{k}{w} \tilde{p}_0(u, v, w), \quad (4.6)$$

where  $w = \text{sgn}(k) \sqrt{k^2 - u^2 - v^2}$ .

Next, we consider the actual measurement condition. Assume the detector has a flat sensing surface. The center of the detector surface represents the detector's position  $\mathbf{r}_0$ . Denote  $\mathbf{r}' = (x', y')$ , which points to an element on the detector surface with respect to  $\mathbf{r}_0$ ; and then  $W(\mathbf{r}') = W(x', y')$  and  $d^2\mathbf{r}' = dx' dy'$ .

Similarly, taking the 2D Fourier transforms of  $\tilde{p}'(\mathbf{r}_0, k)$  on spatial variables  $x_0$  and  $y_0$  gives

$$\tilde{q}'_d(u, v, k) = \int \int_{-\infty}^{+\infty} \tilde{p}'_d(x_0, y_0, k) \exp(iux_0 + ivy_0) dx_0 dy_0. \quad (4.7)$$

Then, from Eq. (4.4), one can derive

$$\tilde{q}'_d(u, v, k) = \tilde{q}_d(u, v, k) \times \tilde{H}(k) \tilde{W}^*(u, v), \quad (4.8)$$

where the symbol  $*$  denotes the complex conjugate, and

$$\tilde{W}(u, v) = \int \int_{-\infty}^{+\infty} W(x', y') \exp(iux' + ivy') dx' dy'. \quad (4.9)$$

The factor  $\tilde{W}(u, v)$  serves as a spatial-frequency filter. Three examples will be described below.

In the first example, assume that the sensing aperture is a disk with a radius of  $P$ .

If  $W(\mathbf{r}') = 1$  when  $|\mathbf{r}'| \leq P$  and 0 otherwise, then

$$\tilde{W}(u, v) = \pi P^2 \times \frac{2J_1(\rho P)}{\rho P}, \quad (4.10)$$

where  $\rho = \sqrt{u^2 + v^2}$  and  $J_1$  is the first order of the Bessel function. We plot the function  $2J_1(\xi)/\xi$  as the solid line in Fig. 4.1. For simplicity, the main-lobe is regarded as the bandwidth. Since the first zero of the Bessel function  $J_1$  is at 3.8317, the maximum  $u$  or  $v$  is  $U = 3.8317/P$ . Therefore, the spatial Nyquist frequency equals  $2 \times U / 2\pi \approx 1.22/P$ . The spatial sampling periods should be  $\Delta x_0, \Delta y_0 \leq 0.8P$  along the  $x_0$ - or  $y_0$ -direction, respectively.

In the second example, assume the sensing aperture is a rectangle with a half width of  $Z$ . If we let  $W(\mathbf{r}') = 1$  when  $-Z \leq x', y' \leq Z$  and zero otherwise, then,

$$\tilde{W}(u, v) = 4Z^2 \times \frac{\sin(uZ)}{uZ} \frac{\sin(vZ)}{vZ}. \quad (4.11)$$

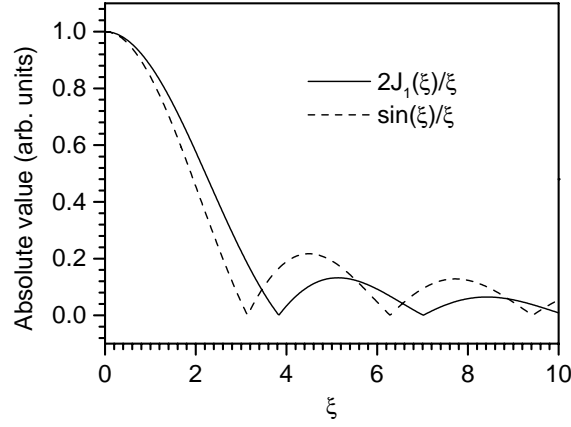


FIG. 4.1. Solid line: function  $2J_1(\xi)/\xi$ ; Dash line: sinc function  $\sin(\xi)/\xi$ .

This is the product of two sinc functions. We plot the sinc function  $\sin(\xi)/\xi$  as the dash line in Fig. 4.1. For simplicity, the main-lobe is again regarded as the bandwidth. The first zero of the sinc function is at  $u = U = \pi/Z$  or  $v = V = \pi/Z$ . Therefore, the spatial Nyquist frequency equals  $2 \times U / 2\pi = 1/Z$ . The spatial sampling periods should be  $\Delta x_0, \Delta y_0 \leq Z$  along the  $x_0$ - or  $y_0$ -direction, respectively.

In the third example, assume the detector is a point, i.e.,  $\tilde{W}(u, v) = 1$  for all  $u$  and  $v$ . Since only the non-evanescent wave is used for reconstruction, both  $u$  and  $v$  should be cut off at  $k_c = 2\pi f_c / c$  which is determined by the temporal-frequency bandwidth  $\tilde{H}(k)$ . In this case, the spatial Nyquist frequency equals  $2 \times 2\pi / k_c = 2f_c / c$ . The spatial sampling periods should be  $\Delta x_0, \Delta y_0 \leq k_c / 2 = \pi f_c / c$  along the  $x_0$ - or  $y_0$ - direction, respectively.

## 2. Cylindrical geometry

The cylindrical coordinates  $\mathbf{r} = (\rho, \varphi, z)$  are employed in this case. The symbol  $\varphi$  denotes the azimuth angle from the  $x$ -axis. Assume the measurement surface is a cylindrical surface  $\mathbf{r}_0 = (\rho_0, \varphi_0, z_0)$ . The sample is enclosed in this cylindrical surface. To conform to the Fourier transform Eqs. (4.1) and (4.2), we can change the Cartesian coordinates to the polar cylindrical coordinates by letting  $\mathbf{k} = (\mu, \varphi_0, \gamma)$  and  $\mathbf{r} = (\rho, \varphi, z)$  with the following relationships:  $\gamma = w$ ,  $u = \mu \cos \varphi_0$ ,  $v = \mu \sin \varphi_0$ ,  $\mu = \sqrt{u^2 + v^2}$ ,  $x = \rho \cos \varphi$ ,  $y = \rho \sin \varphi$ ,  $\rho = \sqrt{x^2 + y^2}$ , and  $k^2 = \gamma^2 + \mu^2$ . Then, the inverse Fourier transform Eq. (4.2) can be rewritten as:

$$p_0(\rho, \varphi, z) = \frac{1}{2\pi} \int_{-\infty}^{+\infty} d\gamma \exp(-i\gamma z) \times \frac{1}{(2\pi)^2} \int_0^{2\pi} d\varphi_0 \int_0^{+\infty} \mu d\mu \times \tilde{p}_0(\mu, \varphi_0, \gamma) \exp[-i\mu\rho \cos(\varphi_0 - \varphi)]. \quad (4.12)$$

Further, by expanding  $\tilde{p}_0(\mu, \varphi_0, \gamma)$  in circular harmonics as

$$\tilde{p}_0(\mu, \varphi_0, \gamma) = \frac{1}{2\pi} \sum_{n=-\infty}^{+\infty} \tilde{p}_{0n}(\mu, \gamma) \exp(-in\varphi_0), \quad (4.13)$$

and considering the identity [24]

$$\exp[-i\mu\rho \cos(\varphi_0 - \varphi)] = \sum_{n=-\infty}^{+\infty} (-i)^n J_n(\mu\rho) \exp[in(\varphi_0 - \varphi)], \quad (4.14)$$

where  $J_n(\cdot)$  is the Bessel function of the first kind, we can rewrite the inverse Fourier transform Eq. (4.12) as

$$\begin{aligned}
p_0(\rho, \varphi, z) &= \frac{1}{2\pi} \int_{-\infty}^{+\infty} d\gamma \exp(-i\gamma z) \times \frac{1}{2\pi} \sum_{n=-\infty}^{+\infty} \exp(-in\varphi) \\
&\times \frac{(-i)^n}{2\pi} \int_0^{+\infty} \mu d\mu J_n(\rho\mu) \tilde{p}_{0n}(\mu, \gamma).
\end{aligned} \tag{4.15}$$

The corresponding forward transform becomes

$$\begin{aligned}
\tilde{p}_{0n}(\mu, \gamma) &= \int_{-\infty}^{+\infty} dz \exp(i\gamma z) \times \int_0^{2\pi} d\varphi \exp(in\varphi) \\
&\times 2\pi (+i)^n \int_0^{+\infty} \rho d\rho J_n(\mu\rho) p_0(\rho, \varphi, z).
\end{aligned} \tag{4.16}$$

We first consider the idealized measurement condition. Expanding  $\tilde{p}_d(\varphi_0, z_0, k)$  in circular harmonics and then taking the Fourier transform on variable  $z_0$  gives

$$\tilde{q}_{dn}(\gamma, k) = \int_{-\infty}^{+\infty} dz_0 \exp(i\gamma z_0) \times \int_0^{2\pi} d\varphi_0 \exp(in\varphi_0) \times \tilde{p}_d(\varphi_0, z_0, k). \tag{4.17}$$

The corresponding inverse transform is

$$\tilde{p}_d(\varphi_0, z_0, k) = \frac{1}{2\pi} \int_{-\infty}^{+\infty} d\gamma \exp(-i\gamma z_0) \times \frac{1}{2\pi} \sum_{n=-\infty}^{+\infty} \exp(-in\varphi_0) \times \tilde{q}_{dn}(\gamma, k). \tag{4.18}$$

Then, from the exact Fourier-domain reconstruction formula Eq. (2.37), we get the relationship between  $\tilde{q}_{dn}(\gamma, k)$  of the measurement and  $\tilde{p}_{0n}(\mu, \gamma)$  of the initial source as:

$$\tilde{q}_{dn}(\gamma, k) = \tilde{p}_{0n}(\mu, \gamma) \times \frac{(-i)^n}{4} k H_n^{(1)}(\mu\rho_0), \tag{4.19}$$

where  $H_n^{(1)}(\cdot)$  is the Hankel function of the first kind.

Next, we consider the actual measurement condition. Assume the detector surface is a section of the cylindrical measurement surface. The center of the detector surface represents the detector's position  $\mathbf{r}_0$ . The vector  $\mathbf{r}'_0$  points to an element on the surface of the detector. Let  $\varphi'$  be the difference between the polar angles of  $\mathbf{r}_0$  and  $\mathbf{r}'_0$ ,

and  $z'$  be the projection of  $\mathbf{r}' = \mathbf{r}'_0 - \mathbf{r}_0$  in the  $z$  axis; then,  $W(\mathbf{r}') = W(\varphi', z')$  and  $d^2\mathbf{r}' = \rho_0 d\varphi' dz'$ . Therefore, the real signal detected at position  $\mathbf{r}_0$  can be expressed as a surface integral over the aperture of the detector as:

$$\tilde{p}'_d(\mathbf{r}_0, k) = \tilde{H}(k) \iint \tilde{p}_d(\varphi_0 + \varphi', z_0 + z', k) W(\varphi', z') \rho_0 d\varphi' dz'. \quad (4.20)$$

Similarly, expanding  $\tilde{p}'_d(\mathbf{r}_0, k)$  in circular harmonics and taking the Fourier transform on variable  $z_0$  gives

$$\tilde{q}'_{dn}(\gamma, k) = \int_{-\infty}^{+\infty} dz_0 \exp(i\gamma z_0) \times \int_0^{2\pi} d\varphi_0 \exp(in\varphi_0) \times \tilde{p}'_d(\varphi_0, z_0, k). \quad (4.21)$$

Then, from Eq. (4.20), one can derive

$$\tilde{q}'_{dn}(\gamma, k) = \tilde{q}_{dn}(\gamma, k) \times \tilde{H}(k) \tilde{W}_n^*(\gamma), \quad (4.22)$$

where

$$\tilde{W}_n(\gamma) = \iint W(\varphi', z') \exp(i\gamma z') \exp(in\varphi') \rho_0 d\varphi' dz'. \quad (4.23)$$

The factor  $\tilde{W}_n(\gamma)$  acts as a spatial-frequency filter.

For example, if we let  $W(\varphi', z') = 1$  in  $-\Phi < \varphi' < \Phi$  and  $-Z < z' < Z$  and zero otherwise, then

$$\tilde{W}_n(\gamma) = 4Z\rho_0\Phi \times \frac{\sin(\gamma Z)}{\gamma Z} \frac{\sin(n\Phi)}{n\Phi}. \quad (4.24)$$

This is a product of two sinc functions. For simplicity, the main-lobe of the sinc function is regarded as the bandwidth. The first zero of the sinc function on  $\gamma$  is at  $\gamma = G = \pi/Z$ .

Therefore, the spatial Nyquist frequency equals  $2 \times G/(2\pi) = 1/Z$ , and then the spatial sampling period along the  $z_0$ -direction should be  $\Delta z_0 \leq Z$ . Because  $n$  is an integer, the



first zero of the sinc function for  $n$  is around  $n = M = [\pi/\Phi]$ , where  $[\ ]$  stands for integer rounding. Therefore, the maximum frequency of the bandwidth for  $n$  is  $M/(2\pi)$ . According to the circular sampling theorem [81,82], the angular Nyquist frequency equals  $2M$ , and then the angular sampling period along the  $\varphi_0$ -direction should be  $\Delta\varphi_0 \leq 2\pi/N$ , where  $N \geq 2M + 1$ , i.e.,  $\Delta\varphi_0 < 2\pi/2M \approx \Phi$ . For a small aperture with a diameter of  $\delta$ ,  $2\Phi \approx \delta/\rho_0$ , so the spatial sampling period along the  $\varphi_0$ -direction should be  $\rho_0\Delta\varphi_0 < \delta/2$ .

### 3. Spherical geometry

The polar spherical coordinates are adopted in this case. Denote  $\theta$  as the polar angle from the  $z$ -axis and  $\varphi$  as the azimuth angle in the  $x$ - $y$  plane from the  $x$ -axis. Assume the measurement surface is a spherical surface  $\mathbf{r}_0 = (r_0, \theta_0, \varphi_0)$ . The sample under study lies inside the sphere. To conform to the Fourier transform Eqs. (4.1) and (4.2), we can change the Cartesian coordinates to the polar spherical coordinates:  $\mathbf{k} = (k, \theta_0, \varphi_0)$  and  $\mathbf{r} = (r, \theta, \varphi)$ , with the following relationships:  $u = k \sin \theta_0 \cos \varphi_0$ ,  $v = k \sin \theta_0 \sin \varphi_0$ ,  $w = k \cos \theta_0$ ,  $x = r \sin \theta \cos \varphi$ ,  $y = r \sin \theta \sin \varphi$ , and  $z = r \cos \theta$ . Then, the inverse Fourier transform Eq. (4.2) can be rewritten as

$$p_0(r, \theta, \varphi) = \frac{1}{(2\pi)^3} \int_{\Omega_0} d\Omega_0 \int_0^{+\infty} k^2 dk \tilde{p}_0(k, \theta_0, \varphi_0) \exp(-i\mathbf{k} \cdot \mathbf{r}), \quad (4.25)$$

where  $d\Omega_0 = \sin \theta_0 d\theta_0 d\varphi_0$ ,  $\theta_0 : 0$  to  $2\pi$  and  $\varphi_0 : 0$  to  $2\pi$ .

Further, by substituting the following identity into Eq. (4.25) [83]:

$$\exp(-i\mathbf{k} \cdot \mathbf{r}) = 4\pi \sum_{l=0}^{+\infty} \sum_{m=-l}^{+l} (-i)^l j_l(kr) Y_l^m(\theta_0, \varphi_0) Y_l^{m*}(\theta, \varphi) , \quad (4.26)$$

where  $j_l(\cdot)$  is the spherical Bessel function of the first kind, and  $Y_l^m(\cdot)$  is the spherical harmonics, and expanding the function  $\tilde{p}_0(k, \theta_0, \varphi_0)$  in spherical harmonics as:

$$\tilde{p}_0(k, \theta_0, \varphi_0) = \sum_{l=0}^{+\infty} \sum_{m=-l}^{+l} \tilde{p}_{0l}^m(k) Y_l^{m*}(\theta_0, \varphi_0) , \quad (4.27)$$

we get

$$p_0(r, \theta, \varphi) = \frac{1}{2\pi^2} \sum_{l=0}^{+\infty} \sum_{m=-l}^{+l} (-i)^l Y_l^{m*}(\theta, \varphi) \int_0^{+\infty} k^2 dk j_l(kr) \tilde{p}_{0l}^m(k) . \quad (4.28)$$

The corresponding forward transform becomes

$$\tilde{p}_{0l}^m(k) = 4\pi \int_{\Omega} d\Omega (+i)^l Y_l^m(\theta, \varphi) \int_0^{+\infty} r^2 dr j_l(kr) p_0(r, \theta, \varphi) , \quad (4.29)$$

where  $d\Omega = \sin\theta d\theta d\varphi$ ,  $\theta : 0$  to  $2\pi$  and  $\varphi : 0$  to  $2\pi$ .

We first consider the idealized measurement condition. The pressure  $\tilde{p}_d(\mathbf{r}_0, k)$  can be expanded in spherical harmonics as

$$\tilde{q}_{dl}^m(k) = \int_{\Omega_0} d\Omega_0 Y_l^m(\theta_0, \varphi_0) \tilde{p}_d(\theta_0, \varphi_0, k) . \quad (4.30)$$

The corresponding inverse transform is

$$\tilde{p}_d(\theta_0, \varphi_0, k) = \sum_{l=0}^{+\infty} \sum_{m=-l}^{+l} \tilde{q}_{dl}^m(k) Y_l^{m*}(\theta_0, \varphi_0) . \quad (4.31)$$

Using the following additional theorem for the spherical harmonics [24]:

$$P_l(\mathbf{n} \cdot \mathbf{n}_0) = \frac{4\pi}{2l+1} \sum_{m=-l}^{+l} Y_l^m(\theta_0, \varphi_0) Y_l^{m*}(\theta, \varphi) , \quad (4.32)$$

where  $\mathbf{n} = (\theta, \varphi)$  and  $\mathbf{n}_0 = (\theta_0, \varphi_0)$  are unit vectors and  $P_l(\cdot)$  is the Legendre polynomial function, from on the exact Fourier-domain reconstruction formula Eq. (2.12), we get the following relationship between  $\tilde{q}_{dl}^m(k)$  of the measurement and  $\tilde{p}_{0l}^m(k)$  of the initial source as:

$$\tilde{q}_{dl}^m(k) = \tilde{p}_{0l}^m(k) \times \frac{(-i)^l}{4\pi} k^2 h_l^{(1)}(kr_0), \quad (4.33)$$

where  $h_l^{(1)}(\cdot)$  is the spherical Hankel function of the first kind.

Next, we consider the actual measurement condition. Assume that the detector surface is a small section of the spherical measurement surface. The vector  $\mathbf{r}_0$ , which points to the center of the detector, represents the position of the detector. The vector  $\mathbf{r}'_0 = \mathbf{r}_0 + \mathbf{r}'$  points to an element on the surface of the detector. Denote  $\theta'$  as the angle between  $\mathbf{r}'_0 = (r_0, \theta'_0, \varphi'_0)$  and  $\mathbf{r}_0 = (r_0, \theta_0, \varphi_0)$ . Assume the weighting factor is dependent only on  $\theta'$ , i.e.,  $W(\mathbf{r}') = W(\theta')$ . Then, the measured signal can be expressed by a surface integral over the detector aperture as

$$\tilde{p}'_d(\mathbf{r}_0, k) = \tilde{H}(k) \int \int_{\mathbf{r}'} \tilde{p}_d(\mathbf{r}_0 + \mathbf{r}', k) W(\theta') d^2 \mathbf{r}', \quad (4.34)$$

where  $d^2 \mathbf{r}' = d^2 \mathbf{r}'_0 = r_0^2 d\Omega'_0$ .

Similarly,  $\tilde{p}'_d(\mathbf{r}_0, k)$  can be expanded in spherical harmonics:

$$\tilde{q}_{dl}^m(k) = \int_{\Omega_0} d\Omega_0 Y_l^m(\theta_0, \varphi_0) \tilde{p}'_d(\mathbf{r}_0, k). \quad (4.35)$$

The function  $W(\theta')$  can be expanded in Legendre polynomials as

$$W(\theta') = \sum_{l'=0}^{+\infty} C_{l'} P_{l'}(\cos \theta'), \quad (4.36)$$

where the coefficients can be computed by

$$C_{l'} = \frac{2l'+1}{2} \int_0^\pi P_{l'}(\cos \theta') W(\theta') \sin \theta' d\theta'. \quad (4.37)$$

Further, by considering the identity [24]:

$$P_{l'}(\cos \theta') = \frac{4\pi}{2l'+1} \sum_{n=-l'}^{+l'} Y_{l'}^{n*}(\theta_0, \varphi_0) Y_{l'}^n(\theta'_0, \varphi'_0), \quad (4.38)$$

we can expand  $W(\theta')$  in spherical harmonics:

$$W(\theta') = \sum_{l'=0}^{+\infty} \tilde{W}_{l'} \sum_{n=-l'}^{+l'} Y_{l'}^{n*}(\theta_0, \varphi_0) Y_{l'}^n(\theta'_0, \varphi'_0) / r_0^2, \quad (4.39)$$

where

$$\tilde{W}_{l'} = 2\pi r_0^2 \int_0^\pi P_{l'}(\cos \theta') W(\theta') \sin \theta' d\theta'. \quad (4.40)$$

Then, by substituting Eqs. (4.34) and (4.39) into (4.35), we get

$$\begin{aligned} \tilde{q}'_m(k) &= \tilde{H}(k) \sum_{l'=0}^{+\infty} \tilde{W}_{l'} \sum_{n=-l'}^{+l'} \\ &\times \int_{\Omega_0} d\Omega'_0 Y_{l'}^n(\theta'_0, \varphi'_0) \tilde{p}_d(\mathbf{r}'_0, k) \\ &\times \int_{\Omega_0} d\Omega_0 Y_l^m(\theta_0, \varphi_0) Y_{l'}^{n*}(\theta_0, \varphi_0). \end{aligned} \quad (4.41)$$

In Eq. (4.41) the integral over  $\Omega_0$  gives  $\delta_{ll',mn}$  and then the summation  $\sum_{l'=0}^{+\infty} \sum_{n=-l'}^{+l'}$  reduces

to one term:  $l' = l$  and  $n = m$ , and finally the integral over  $\Omega'_0$  gives  $\tilde{q}'_m(k)$  according to the definition of Eq. (4.30). In sum, Eq. (4.41) is simplified to

$$\tilde{q}'_m(k) = \tilde{q}_m(k) \times \tilde{W}_l \tilde{H}(k). \quad (4.42)$$

The factor  $\tilde{W}_l$  acts as a spatial-frequency filter.

For example, if we let  $W(\theta') = 1$  when  $\theta'$  from 0 to  $\Theta$  and zero otherwise, then for  $l \neq 0$ ,

$$\tilde{W}_l = 2\pi r_0^2 \frac{\cos \Theta P_l(\cos \Theta) - P_{l+1}(\cos \Theta)}{l}, \quad (4.43)$$

and for  $l = 0$ ,

$$\tilde{W}_0 = 2\pi r_0^2 (1 - \cos \Theta). \quad (4.44)$$

Assume  $2\Theta = \pi/N$ . When  $N \geq 20$ , the ratio  $\tilde{W}_l/\tilde{W}_0$  as a function of  $l/N$  approaches a curve of  $2J_1(\xi)/\xi$  with  $\xi = \pi l/(2N)$  as the solid line in Fig. 4.1. For simplicity, the main-lobe of the ratio is regarded as the bandwidth. The first zero is at  $l = 3.8317 \times 2N/\pi \approx 2.4N$ . According to the circular sampling theorem [81,82], the angular Nyquist sampling frequency equals  $4.8N$ , and then the angular sampling period should be less than  $2\pi/(4.8N + 1) \approx \pi/(2.4N) = 2\Theta/2.4 \approx 0.8\Theta$ . For a small aperture with a diameter  $\delta$ ,  $2\Theta \approx \delta/r_0$ , so the spatial sampling period should be less than  $r_0 \times 0.8\Theta < 0.4\delta$ .

#### 4. Summary and discussions

The spatial sampling in the PA measurements for various geometries, including planar, cylindrical and spherical surfaces, have been studied in the above three sections. In general, the main-lobe of the spatial spectrum of the sensing aperture of the detector cuts off at about half the diameter of the rectangular-shaped surface or at four-tenths of

the disc-shaped surface. Therefore, in principle, if the spatial sampling period is less than half the diameter of the sensing aperture of the detector, aliasing due to spatially discrete sampling can be avoided or significantly reduced. Otherwise, significant aliasing may be present in the sampled data as a result of under-sampling (sampling at a frequency that is less than the Nyquist frequency). The aliasing effect on the PA reconstruction is actually dependent on the measurement geometry as well as the spectrum of the object under study. Two general cases are discussed below.

If the detection scan is along a straight line, such as in a planar scan or a  $z$ -scan in a cylindrical scan, the aliasing effect on the reconstruction is similar no matter where the object is in relation to the scan line, because the spectrum of the object along the direction of the scan line is independent of the distance from the object to the scan line. For example, for a line object with a length of  $a$  that is parallel to the scan line, its spatial spectrum is a sinc function as  $\sin(ua/2)/(ua/2)$ . The main-lobe of this sinc function cuts off at  $U_a = 2\pi/a$ , which contains the most frequency information about the object. The actual measurement cuts off the spatial-frequency bandwidth at  $U_\delta = 2\pi/\delta$ , where  $\delta$  is the diameter of the sensing aperture of the detector. If  $a < \delta$ ,  $U_a > U_\delta$ , that is to say, the whole spatial-frequency bandwidth of the measurement contains the frequency information of the object, the spatial sampling period must be less than  $\delta/2$  to avoid aliasing. If  $a > \delta$ ,  $U_a < U_\delta$ , that is to say, in addition to the whole region below  $U_a$ , the spatial-frequency bandwidth of the measurement contains a frequency range from  $U_a$  to  $U_\delta$  that only provides some minor information about the object, the spatial sampling

period can be larger than  $\delta/2$  but must be less than  $a/2$  for aliasing to be significantly reduced.

If the detection scan is along a circle, such as a spherical or cylindrical scan, the aliasing effect on the reconstruction is related to the distance from the object to the center of the scan circle. For example, with an arc object parallel to the scan circle, its spatial spectrum along the circular direction is a sinc function as  $\sin[la/(2r)]/[la/(2r)]$ , where  $a$  and  $r$  are the arc length and the distance from the arc to the scan center, respectively. The main-lobe of this spectrum cuts off at an angular frequency at  $l = L_a = 2\pi r/a$ , which contains the most angular frequency information about the object. Obviously, when the object is farther away from the scan center, i.e.,  $r$  is larger, the main-lobe has more  $l$  terms and a higher cutoff frequency. For a small aperture with a diameter of  $\delta$ , the actual measurement cuts off the spatial-frequency bandwidth at around  $l = L_\delta = 2\pi r_0/\delta$ , where  $r_0$  is the radius of the scan circle. In the case of  $r/a > r_0/\delta$ , i.e.,  $L_a > L_\delta$ , the spatial sampling period must be less than  $\delta/2$  to avoid aliasing. In the case of  $r/a < r_0/\delta$ , i.e.,  $L_a < L_\delta$ , the spatial sampling period can be larger than  $\delta/2$  but must be less than  $a/2$  to reduce aliasing. However, a sampling period larger than  $\delta/2$  has some risks. For example, with a spatial sampling period of  $\delta$ , the aliasing may be minor for an object located inside  $r < r_1$  if  $r_1/a = r_0/(2\delta)$ , but the aliasing will be significant for an object that is outside  $r > r_1$ .

### C. Aliasing artifacts

In this section, we use some numerical simulations based on the method described in Chapter II to illustrate the aliasing effect on PA reconstruction. We consider uniform spherical absorbers surrounded by a non-absorbing background medium. For convenience, we use the centers of the absorbers to denote their positions. The simulated PA signal is in a temporal-frequency range below 4 MHz, and the data sampling frequency is 20 MHz, which is sufficient to avoid aliasing related to the temporally discrete sampling. Two general cases are tested below.

#### 1. *Linear scan*

One case involves a detection scan along a straight line. Without loss of generality, we can take the planar measurement area as an example. Assume the measurement surface is  $40 \text{ mm} \times 40 \text{ mm}$ . Two sides of the measurement area are parallel to the  $x$ -axis and  $y$ -axis of the Cartesian coordinates system, respectively, and the center of the measurement area is located at the center of the coordinates system. For simplicity, assume that the detector surface is a rectangle with a diameter of 2 mm. According to the theoretical results in Sec. B, the spatial sampling periods along the  $x$ - and  $y$ - axes should be less than 1 mm. In other words, the PA signal should be uniformly sampled from at least 41 positions in a length of 40 mm.

We consider a pair of spherical absorbers with a diameter of 1.5 mm. The amplitudes of the initial acoustic pressures of these two absorbers are 1 and 0.2, respectively, and the centers of the absorbers are located at  $(-5, 0, 10)$  and  $(5, 0, 10)$  in



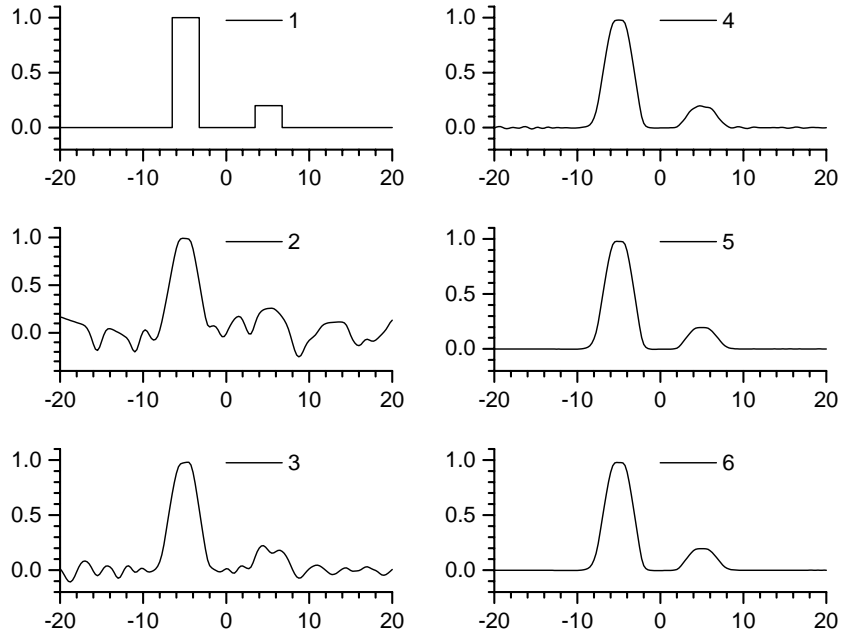


FIG. 4.2. Pressure profiles along the line ( $y = 0$ ,  $z = 10$  mm) that is parallel to the  $x$ -axis. Vertical axis is the amplitude in arbitrary unit. Horizontal axis is in mm. Curve 1: original profile. Curves 2 to 6: reconstructions from the measurements with sampling periods, including 4 mm, 2 mm, 1 mm, 0.5 mm and 0.4 mm, respectively.

unit of mm, respectively. Curve 1 in Fig. 4.2 shows the initial pressure profile along the line through the centers of the absorbers.

We computed the reconstructions from the measurements with various spatial sampling periods, including 4 mm, 2 mm, 1 mm, 0.5 mm, and 0.4 mm, which correspond to the  $11 \times 11$ ,  $21 \times 21$ ,  $41 \times 41$ ,  $81 \times 81$  and  $101 \times 101$  detection positions uniformly distributed on the measurement area, respectively. The profiles of these reconstructions along the line through the centers of the absorbers are plotted as curves 2–6 in Fig. 4.2, respectively. When the sampling periods are much greater than 1 mm (i.e., under-sampling), as, for example, curves 2 and 3 in Fig. 4.2, the reconstructions

contain significant artifacts that result from the aliasing. The aliasing in curve 2 is so serious that the object with low amplitude is buried in aliasing noise. Curve 4 is in good agreement with the original profile because it is from a measurement with a sufficient sampling period of 1 mm, although the reconstruction is blurred by the limited bandwidth of the PA signal. Curves 5 and 6 have smaller sampling periods, 0.5 mm and 0.4 mm, respectively, and their spatial-frequency bandwidths contain the first side-lobe of the sinc function shown in Eq. (4.11). The reconstructions for curves 5 and 6 are a little better than that for curve 4, but the improvement is not significant. This is because the amplitude of the side-lobe of the spectrum is much smaller than the value of the main-lobe.

## *2. Circular scan*

Another case is when the detection scan is along a circle. We take the cylindrical measurement surface as an example. Assume the measurement area has a length of 90 mm and a radius of 25 mm. We assume that the  $z$ -axis of the cylindrical coordinates system is parallel to the length of the measurement surface and the origin is located at the center of the cylindrical measurement surface. We also assume that the aperture of the detector is a section of the measurement surface, and its aperture sizes along the  $\varphi_0$ -direction and the  $z$ -axis are  $\pi$  mm and 3 mm, respectively. According to the theoretical results in Sec. B, the spatial sampling periods along the  $\varphi_0$ -direction and the  $z$ -axis should be less than  $\pi/2$  mm and 1.5 mm, respectively. In other words, the PA signal

should be uniformly sampled at a minimum of 101 positions along the  $\phi_0$ -direction and 61 positions along the  $z$ -axis, respectively.

We consider a spherical absorber with a diameter of 1.5 mm. Assume that the amplitude of the initial acoustic pressure of the absorber is 1, the profile of which is the same as the left object in curve 1 of Fig. 4.2. In the simulation, the spatial sampling period along the  $z$ -axis is 1.5 mm, so the aliasing resulting from the discrete sampling along this direction is negligible. We assume that the center of the spherical absorber is located at the  $x$ -axis.

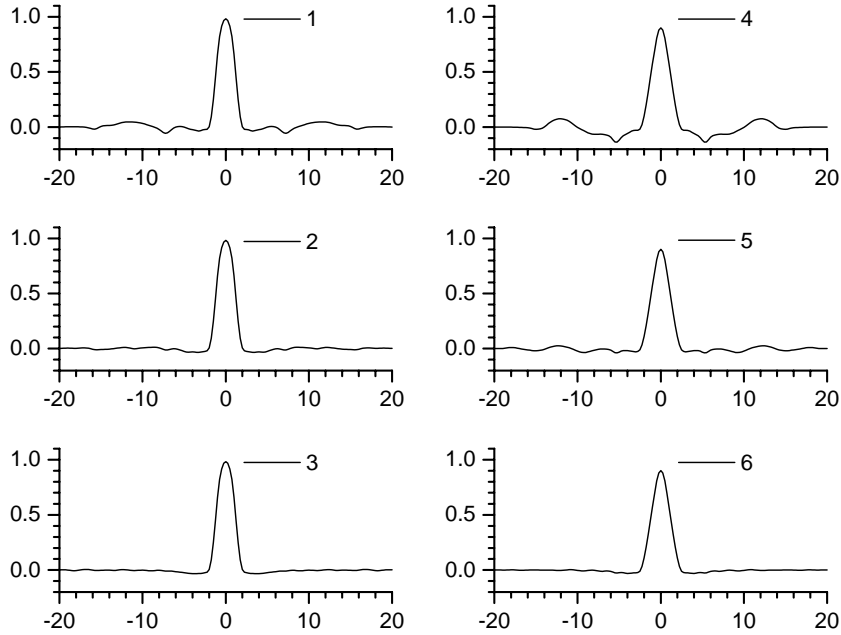


FIG. 4.3. Pressure profiles. Curves 1 to 3: reconstructions with sampling periods, including  $\pi$  mm,  $\pi/2$  mm, and  $\pi/4$  mm, respectively, along the line ( $x = 8$  mm,  $z = 0$ ), when the absorber is at ( $x = 8$  mm,  $y = z = 0$ ). Curves 4 to 6: reconstructions with sampling periods, including  $\pi$  mm,  $\pi/2$  mm, and  $\pi/4$  mm, respectively, along the line ( $x = 16$  mm,  $z = 0$ ), when the absorber is at ( $x = 16$  mm,  $y = z = 0$ ).

We then compute two series of reconstructions with the absorber located at position 1 ( $x = 8$  mm) and position 2 ( $x = 16$  mm), respectively. Each series is from measurements with spatial sampling periods, including  $\pi$  mm,  $\pi/2$  mm, and  $\pi/4$  mm, which correspond to 51, 101, and 201 detection positions along the  $\varphi_0$ -direction, respectively. The profiles of the reconstructions are plotted as curves 1–3 for position 1 and 4–6 for position 2 in Fig. 4.3, respectively. Both curves 1 and 4 have significant aliasing. However, curve 4 (the object at  $x = 16$  mm) has stronger artifacts than curve 1 ( $x = 8$  mm). This indicates that when the object is farther away from the center of the scan circle, more aliasing artifacts occur in reconstruction, which is consistent with the theoretical results presented in the previous section. The aliasing effects on reconstruction curves 2, 3, 5, and 6 are negligible, since the spatial sampling periods are equal to, or less than half, the diameter of the sensing aperture.

In summary, the above numerical experiments have demonstrated that half of the diameter of the sensing aperture is a sufficient spatial sampling period to significantly reduce aliasing, which is consistent to the theoretical results. Smaller sampling periods, such as one-quarter of the diameter of the sensing aperture, do not provide significant improvement in image quality. Further decreases in the spatial sampling periods do tremendously expand the number of data acquisition positions required, which means an increase in the amount of raw data that must be included in the reconstruction as well as an increase in the data acquisition time if the measurement is performed by the scanning of a single detector or a small number of them.

### **D. Summary**

We have analyzed sampling strategies in PA measurement for three measurement geometries, including planar, spherical, and cylindrical surfaces. In practice, to significantly reduce aliasing, it is reasonable to let the discrete spatial sampling period be slightly smaller than half of the diameter of the sensing aperture of the detector. We conclude, however, that it is not necessary to let the sampling period be smaller than one quarter of the diameter of the sensing aperture because smaller sampling periods increase tremendously the number of the detection positions but do not provide significant improvement in image quality. Finally, our results indicate that the spatial resolution of PA reconstruction is physically limited by both the aperture size of the detector and the temporal-frequency bandwidth of the PA signal.

## **CHAPTER V**

### **BREAST IMAGING**

#### **A. Introduction**

Breast cancer is the most common cancer among women, accounting for one out of every three cancer diagnoses. In 2001, the statistical expectation was that approximately 192,200 new cases of invasive breast cancer—and about 40,000 in situ carcinomas—would be diagnosed [84]. The incidence of breast cancer increases with age: approximately 3 out of 4 women with a new diagnosis of breast cancer each year are older than 50.

Although breast cancer remains a leading cause of cancer deaths among women, the cure rate is much improved by early detection. X-ray mammography and ultrasonography are the current clinical tools for breast-cancer screening and detection. Mammography is the “gold standard”; however, it uses ionizing radiation and has difficulty in imaging pre-menopausal breasts, which are radiographically dense. Currently, ultrasonography is used only as an adjunct tool to x-ray mammography and tends to miss non-palpable tumors.

RF electromagnetic waves can generate a myriad of effects in biological specimens. Most of the effects are not harmful under controlled conditions and can therefore be used to make useful diagnostic measurements. The observed effects in tissue can be cataloged into thermal and nonthermal effects. The most investigated and documented effect of RF power on biological tissues is thermal: when electromagnetic

energy is transformed into kinetic energy in absorbing molecules, heating and subsequent thermoacoustic or photoacoustic emission occurs in the medium.

The dielectric properties of tissues determine their patterns of energy deposition upon irradiation by an electromagnetic field. Because the dielectric properties of normal and malignant tissues are found to vary appreciably over a range of frequencies [85] (Fig. 5.1), RF-based imaging is promising for early detection of tumors [86].

Throughout the RF region, all soft tissues of high water content have qualitatively similar properties. The most striking feature is the large increase in the relative dielectric constant at frequencies below 0.1 GHz and the large increase in the conductivity at frequencies above 1 GHz [87]. At frequencies below 0.1 GHz, the large increase in the relative dielectric constant is due to the charging of cell membranes, with smaller contributions coming from the protein constituents and possibly ionic diffusion along surfaces in the tissue [87]. At frequencies above 0.1 GHz, the changes in the

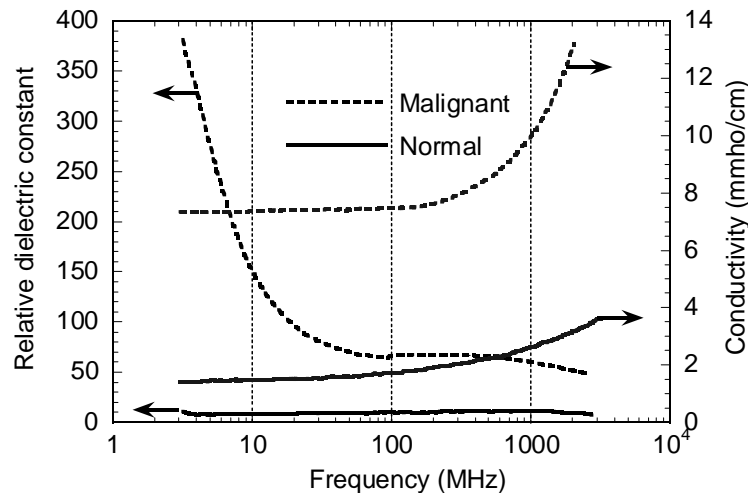


FIG. 5.1. Properties of human breast tissues.

relative dielectric constant and conductivity with frequency probably reflect relaxation of the tissue proteins and protein-bound water as well as other sources [87]. At frequencies above ~5 GHz, the dipolar relaxation of tissue water primarily determines the change in the dielectric properties [87]. Because of the free water and sodium in the malignant tissue, conductivity increases significantly with frequency. In addition, the “static” permittivity of the free water contributes predominantly to the permittivity of tissue at UHF frequencies.

As discussed in Chapter I, the RF absorption or heating results from both ionic conductivity and vibration of the dipole molecules of water and proteins [28]. However, the absorption is a complex function of the frequency and the dielectric property of the tissue. In general, the absorption coefficient, which measures the probability of RF absorption per unit of infinitesimal length, can be calculated by [23]

$$\alpha = \omega \sqrt{(\mu\epsilon/2) \left[ \sqrt{1 + (\sigma/(\omega\epsilon))^2} - 1 \right]}, \quad (5.1)$$

where  $\omega$  is the angular frequency,  $\mu$  is the permeability,  $\epsilon$  is the permittivity, and  $\sigma$  is the conductivity. The reciprocal of the absorption coefficient is the 1/e penetration depth  $\delta = 1/\alpha$ . Eq. (5.1) shows that the ionic conductivity property dominates the absorption at very low frequencies and the permittivity property dominated the absorption at very high frequencies.

The 1/e penetration depths based on the data in Fig. 5.1 are plotted in Fig 5.2, which clearly shows that there is a large contrast in microwave absorption between the normal and malignant breast tissues in a wide range of frequencies [34]. The contrast



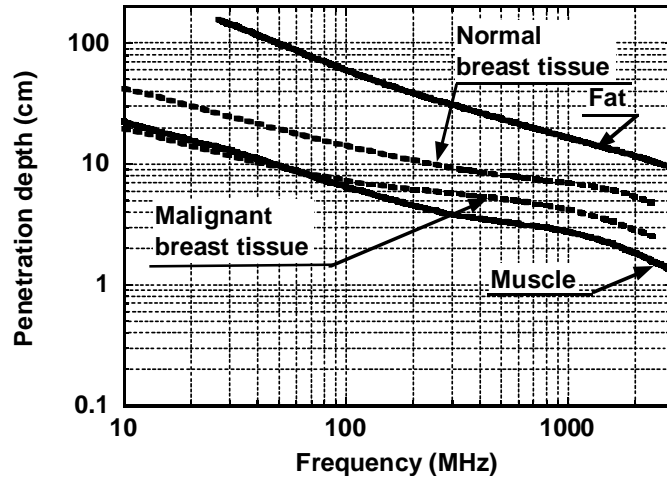


FIG. 5.2. Penetration depths versus frequencies.

between tumor tissue and normal tissue is mainly caused by the extra water and bound sodium in the tumor tissue [88]. This large contrast is the primary motivation for our research and will be exploited by our application of RF photoacoustic tomography. Most other soft tissues have penetration depths in between those for muscle and fat tissues. The wide range of values among various tissues makes it possible to achieve high image contrast. In addition, there is a tradeoff between the RF absorption and the penetration depth. At the frequency of our experimental setup, 3 GHz, the penetration depths for fat and muscle are 9 and 1.2 cm, respectively. Therefore, 3 GHz microwave is a good choice for imaging big-sized fatty tissues such as human breast.

In this chapter, we report an initial study of RF-induced PAT and its application of breast imaging. First, we describe a prototype of RF-induced PAT imaging system we have built. Then, we show some experimental results on phantom samples. Finally, we present a preliminary study of breast cancer detection.

### B. Measurement method<sup>1</sup>

In the initial study, for simplicity, we use 2-D circular measurement geometry. Figure 5.3 shows the experimental setup. A plexiglass container is filled with mineral oil. An unfocused transducer is immersed inside it and fixed on a rotation device. A step motor drives the rotation device and then moves the transducer scan around the sample on a horizontal  $x$ - $y$  plane, where the transducer horizontally points to the rotation center. A sample is immersed inside the container and placed on a holder: it is made of a thin plastic material, which is transparent to microwaves. The transducer (V323, Panametrics) has a central frequency of 2.25 MHz and a diameter of 6mm.

The microwave pulses transmitted from a 3-GHz microwave generator have a pulse energy of 10 mJ and a pulse width of 0.3 or 0.5  $\mu$ s. A function generator (Protek, B-180) is used to trigger the microwave generator, control its pulse repetition frequency, and synchronize the oscilloscope sampling.

In our experiments, the pulse repetition frequency is 50 Hz and the oscilloscope sampling frequency is 20 or 50 MHz. Microwave energy is delivered to the sample by a rectangular waveguide with a cross section of 72 mm  $\times$  34 mm or a horn. A personal computer is used to control the steps. The signal from the transducer is first amplified through a pulse amplifier, then recorded and averaged 100~500 times by an oscilloscope (TDS640A, Tektronix), and finally transferred to a personal computer for imaging.

---

<sup>1</sup> ©2002 American Association of Physicists in Medicine. Reprinted, with permission from M.-H. Xu and L.-H. Wang, "Pulsed-microwave-induced thermoacoustic tomography: Filtered backprojection in a circular measurement geometry," *Med. Phys.* **29**, 1661–1669 (2002).

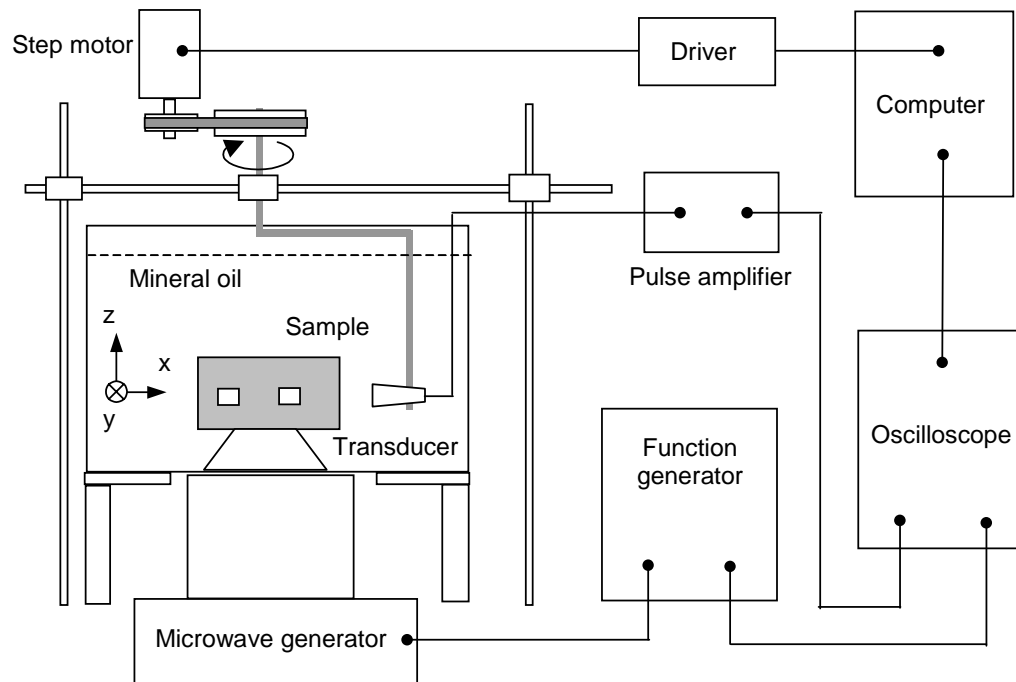


FIG. 5.3. Diagram of experimental setup.

### C. Phantom experiments<sup>2</sup>

#### 1. Image contrast

Image contrast is an important index for biological imaging. Figure 5.4(a) shows a tested sample, which was photographed after the experiment. The sample was made according to the following procedure. First, we cut a thin piece of homogeneous pork fat tissue and shaped it arbitrarily to form a base. Its thickness is 5 mm and its maximum diameter is 4 cm. Then we used different screwdrivers to carefully make two pairs of

---

<sup>2</sup> ©2002 IEEE. Reprinted, with permission, from M.-H. Xu and L.-H. Wang, "Time-domain reconstruction for thermoacoustic tomography in a spherical geometry," IEEE Trans. on Med. Imaging **21**, 814–822 (July 2002).

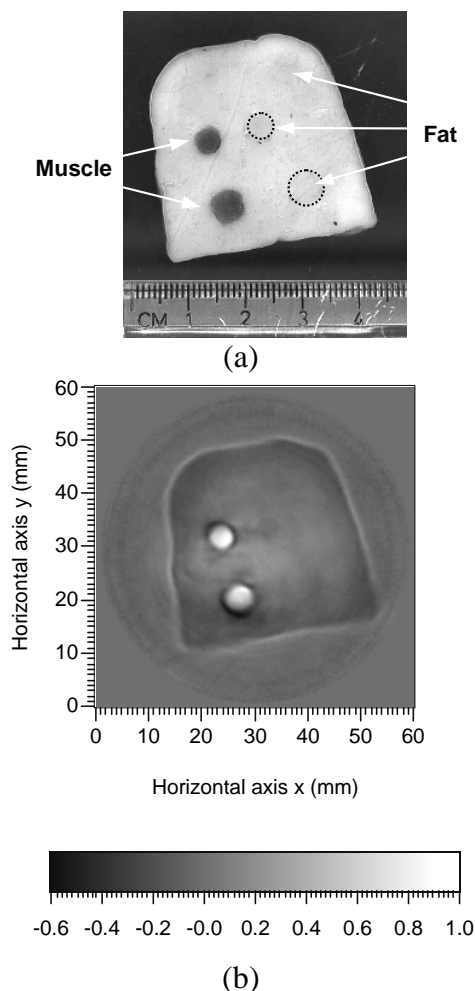


FIG. 5.4. (a) Photograph of the cross-section of a tissue sample; (b) Reconstructed image.

holes that were approximately 4 mm and 6 mm in diameter, respectively. Finally, one big and one small hole on the left side was filled with pork muscle, while the big and small hole on the right side were filled with pork fat of the same type as that which made up the base.

In the experiment, the transducer rotationally scanned the sample from 0 to 360 degrees with a step size of 2.25 degrees. We used the 160 series of data to calculate the image by the back-projection method. The reconstructed image is shown in Fig. 5.4(b).

The outline and size of the fat base as well as the sizes and locations of the two muscle pieces are in good agreement with the original sample in Fig. 5.4(a). The high contrast is due to the low microwave absorption capacity of fat (low water content: 10%) and the high absorption capacity of muscle (high water content: 70%). The two pieces of fat are not visible in the image Fig. 5.4(b), which means the minute mechanical discontinuity between the boundaries of muscle and fat does not contribute much to the thermoacoustic or photoacoustic signal. On the contrary, the discontinuity improves the strength of the echo sounds in pure-ultrasound imaging. This experiment demonstrates that water content in tissues is one important factor that affects the RF absorption.

## ***2. Spatial resolution***

Spatial resolution is another important index for biological imaging. We used samples with a set of small thermoacoustic or photoacoustic sources to test the resolution. One tested sample is shown in Fig. 5.5(a), which was also photographed after the experiment was completed. The sample was made according to the following procedure. First, we cut a thin piece of homogeneous pork fat tissue and made it into an arbitrary shape. Its thickness was 5 mm with a maximum diameter of 4 cm. Then we used a small screwdriver to carefully make a set of small holes about 2 mm in diameter. In the meantime, we prepared a hot solution with 5% gelatin, 0.8% salt and a drop of dark ink (to improve the photographic properties of the sample). Next, we used an injector to inject a drop of the gelatin solution into each small hole and subsequently blew out the air to make good coupling between the gelatin solution and the fat tissue.

After being cooled in room temperature for about 15 minutes, the gelatin solution was solidified. Finally, the sample was buried 1-cm deep inside a fat base [Fig. 5.5(b)]. During the experiment, the transducer rotationally scanned the sample from 0 to 360 degrees with a step size of 2.25 degrees.

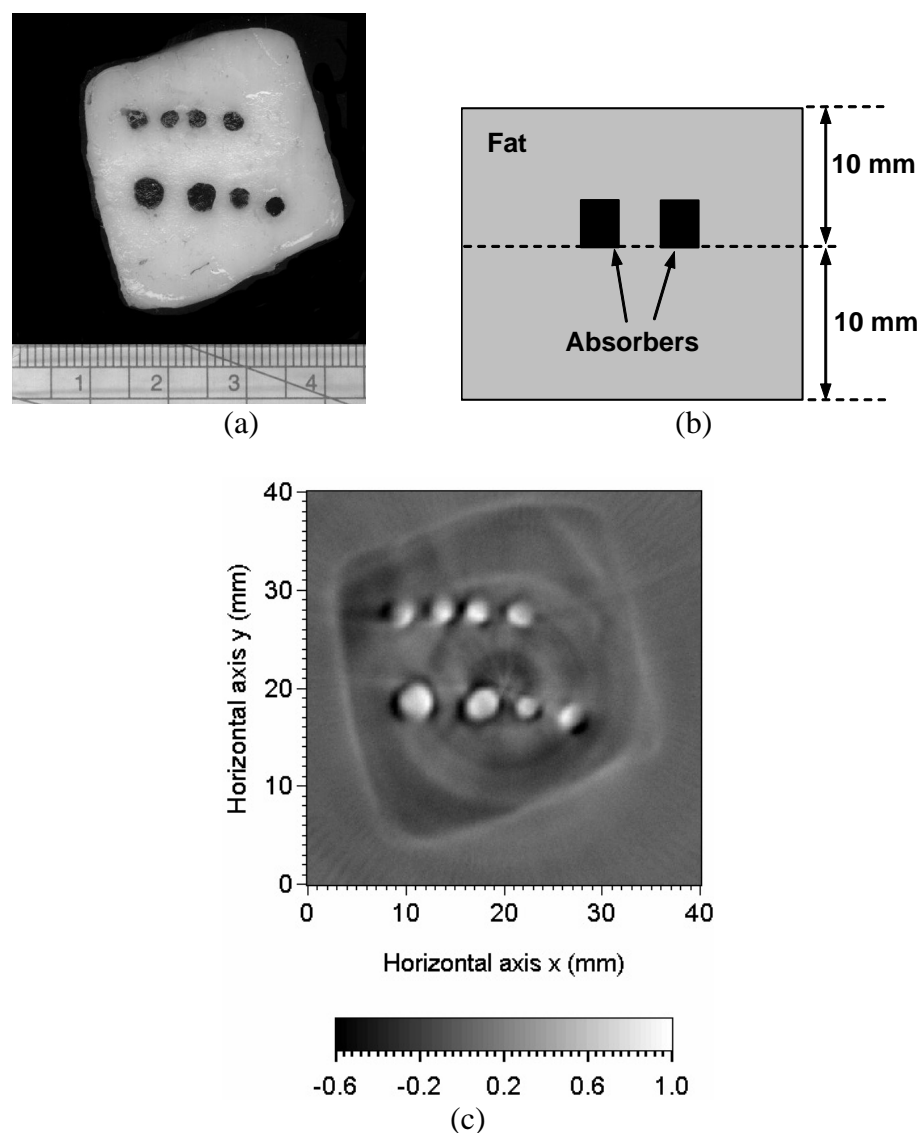


FIG. 5.5. (a) Photograph of the cross-section of a tissue sample; (b) Side-view of the sample buried 1-cm deep inside a fat base; (c) Reconstructed image.

The reconstructed image produced by the back-projection method is shown in Fig. 5.5(c), which agrees with the original sample very well. In particular, the relative locations and sizes of those small thermoacoustic or photoacoustic sources are clearly resolved and perfectly match the original ones.

We further quantified the line spread function (LSF) of the imaging system with pulse duration of 0.3  $\mu$ s. A metal wire with a diameter of 0.2 mm was buried in pork fat and then imaged by our imaging system with a scan radius of 75 mm. The photoacoustic image of the embedded wire is shown in Fig. 5.6(a). Fig. 5.6(b) shows the profile of the LSF across the wire, where the ringing is caused primarily by the bandwidth of the detection system. Its full width at half maximum (FWHM) is about 0.5 mm. We can, therefore, claim the spatial resolution of our experimental system reaches 0.5 mm, which agrees with the theoretical spatial-resolution limit for 3 MHz photoacoustic signals whose half wavelength is  $<0.5$  mm in soft biological tissues. It is worth noting that the claimed 0.5-mm resolution is a worst-case estimation of the true resolution because of

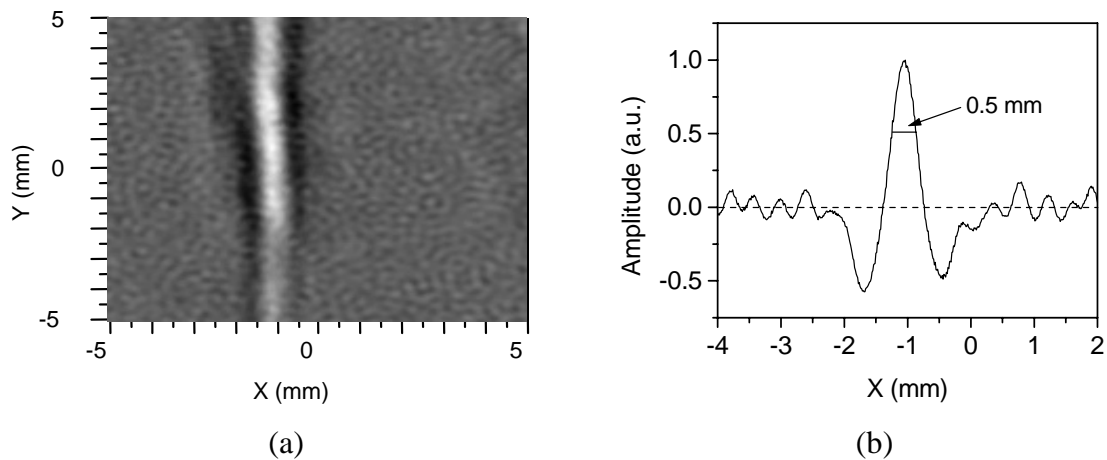


FIG. 5.6. (a) Photoacoustic image of a thin wire; (b) Profile across the wire.

the finite thickness of the wire (0.2 mm diameter).

Of course, the detecting transducer has a finite physical size. If it is close to the photoacoustic sources, it cannot be approximated as a point detector. Its size will blur the images and decrease the spatial resolution. Therefore, in experiments, the transducer must be placed some distance away from the tissue samples.

### ***3. Images of thick samples***

The advantage of using microwave is its long penetration depth in soft tissue. A microwave can reach a tumor buried inside tissue and heat it to generate photoacoustic waves. One tested sample is shown in Fig. 5.7. The experiment was conducted according to a procedure similar to the one above.

Figure 5.7(a) shows the diagram of the measurement. Three small absorbers were buried inside a big fat base. The big pork fat tissue had a maximum diameter of 7 cm. Screwdrivers were used to carefully make three holes about 5 mm in diameter with a depth of 2.5 cm. Next, an injector was used to inject a drop of the same gelatin solution as above into each small hole, and, subsequently, air was blown out to improve the coupling between the gelatin solution and the fat tissue. These gelatin sources were about 5 mm in diameter. After being cooled at room temperature, the gelatin solutions solidified. The photograph of the sample at this stage is shown in Fig. 5.7(b). Finally, the holes were filled with fat, and the gelatin sources were buried in the fat tissue. During the experiment, a microwave was transmitted out to the sample from below. The transducer rotationally scanned the sample, including the gelatin sources, from 0 to 360



degrees in a plane as Fig. 5.7(a) shows. The distance between the transducer and the rotation center was 7 cm. The reconstructed image produced by our back-projection method, which agrees well with the original sample, is shown in Fig. 5.7(c). The relative locations and sizes of those photoacoustic sources perfectly match the buried objects in the original sample.

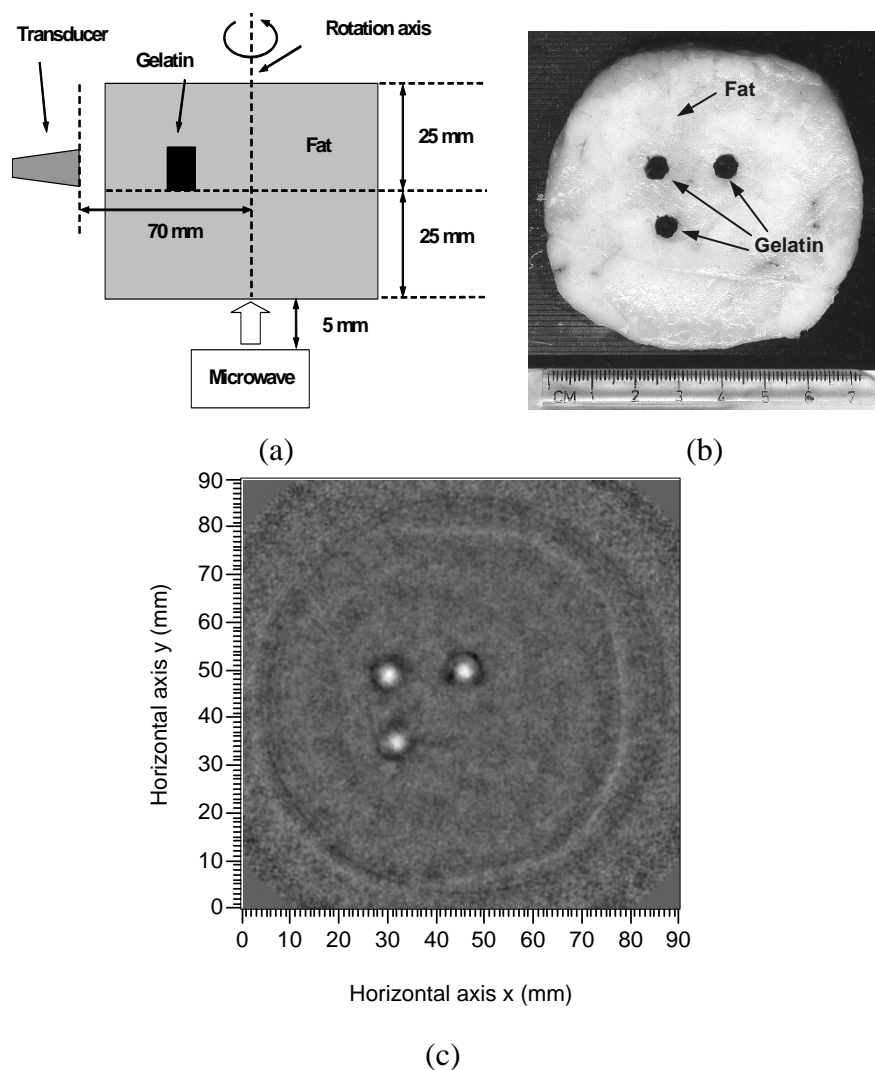


FIG. 5.7. (a) Diagram of the measurement; (b) Cross section of the tissue sample; (c) Reconstructed image.

### D. Breast cancer imaging

Finally, we took the prototype of PAT system to the University of Texas M.D. Anderson Cancer Center and conducted a preliminary study of breast imaging. In our initial study, we investigated big-sized tumors in breast mastectomy specimens. Four excised breast specimens were imaged. The tumor regions in these specimens can be located in the PAT images as expected.

In experiments, we followed the following procedure.

First, a mammogram before the mastectomy surgery of the breast was taken at the Cancer Center. Fig. 5.8(a) shows the mammogram of the biggest specimen in all the four samples we investigated. Generally, a mammogram is formed by the different attenuations of the x-ray beam within a patient's breast. Objects with increased attenuation produce shadows. The image contrast produced by an object depends on its attenuation of the x-ray beam. To improve the contrast, the breast is often taken with standard compression.

After the surgery performed by Dr. Hunt, the excised specimen was placed in a plastic cylindrical container with a diameter of 10 cm [Fig. 5.8(b)]. The nipple of the specimen faced the bottom of the container to simulate the proposed *in vivo* geometry. The thickness of the specimen in the container was ~6 cm. The container had minimal effect on the transmission of RF, ultrasound, and x-ray.

Then, another radiograph of the specimen was taken from the top of the cylindrical container [Fig. 5.8(c)]. In this case, the tumor region is not clear imaged. This

is because the 6-cm thickness of the specimen in the container seriously blurred the x-ray image.

Next, a conventional B-mode gray-scale sonogram of the specimen [Fig. 5.8(d)] was taken by Dr. Fornage using a real-time scanner (HDI 5000, Philips-ATL, Bothell, WA) equipped with a 5–12 MHz broadband linear array electronic transducer. The tumor region was marked by two lines. In sonogram, the contrast is based on the tissues' mechanical properties.

Finally, the specimen was imaged using our photoacoustic imaging system. A circular scan was carried out by a cylindrically focused ultrasound detector (2.25 MHz center frequency and 0.9 mm diameter) with a step size of  $2\frac{1}{4}$  degrees. The scan radius was 7.5 cm. The reconstructed image [Fig. 5.8(e)] was computed by the back-projection method. We adjusted the image contrast and set a threshold level to depress the background. The tumor region clearly shows up (marked by a circle), the location of which agrees with the original sample's. Of course, the normal breast tissues also have certain RF absorption. In principle, based on the pathological characteristics, the tumor region can be differentiated from the normal tissues.

After these imaging experiments, the specimen was rendered to the Department of Pathology for histopathological diagnosis. This lesion was diagnosed as invasive lobular carcinoma with a size of ~1.5 cm.

The rectangle in Fig. 5.8(d) marks the wave-guide aperture. The wave-guide for this experiment was not large enough to cover the entire specimen. Since then, we have upgraded our system with a larger wave-guide to overcome this problem.

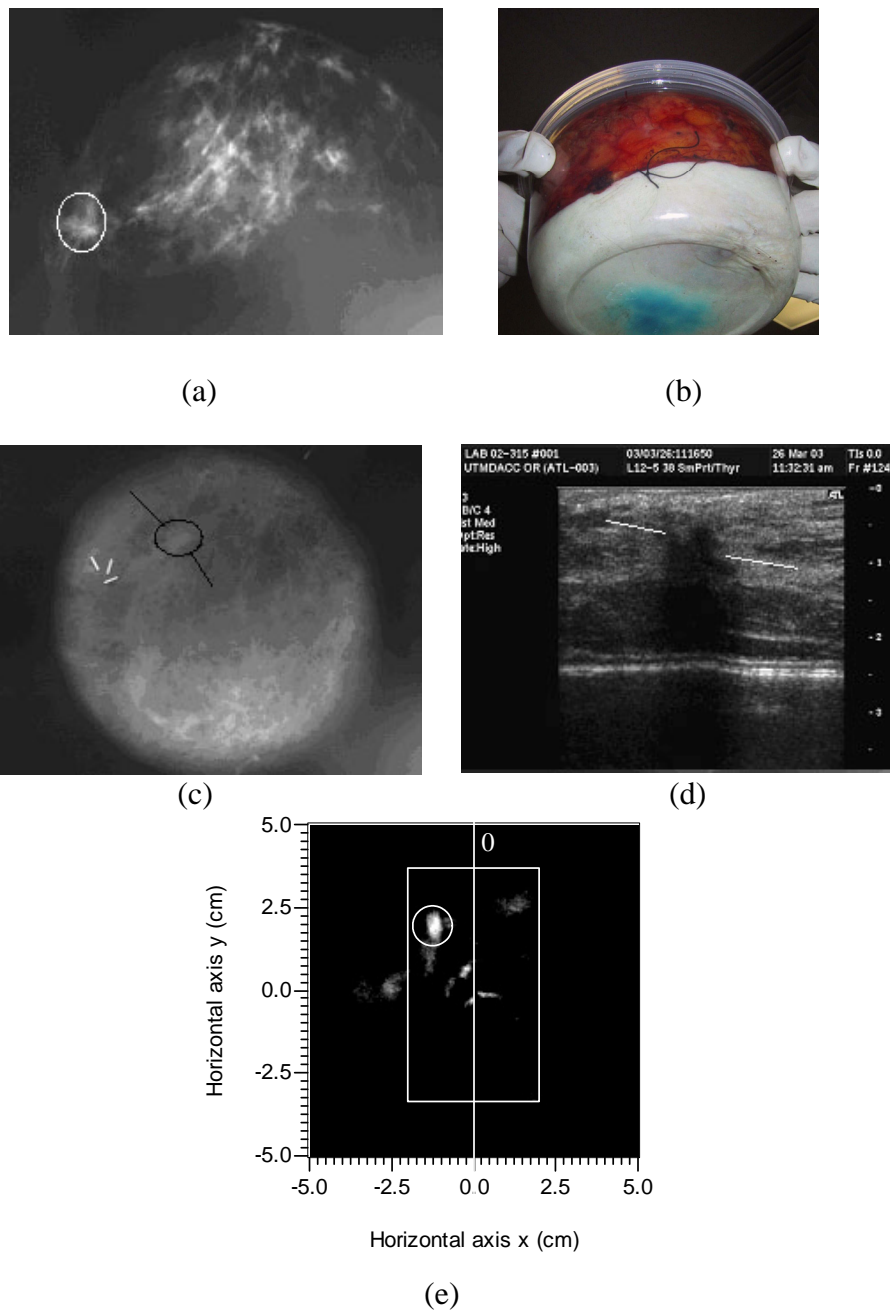


FIG. 5.8. (a) Pre-operative mammogram showing suspicious density in the breast, which was taken with standard compression. (b) The mastectomy specimen placed in a plastic cylindrical container with a diameter of 10 cm (c) Radiograph of the mastectomy specimen in the container. (d) Sonogram of the specimen in the container. (e) Photoacoustic image of the specimen in the container. The rectangle marks the wave-guide aperture. The tumor is marked by a circle in (a), (c) and (e) and by two white lines in (d).

### **E. Summary**

We have built a prototype of RF-induced photoacoustic or thermoacoustic imaging system. Then, we have conducted a series of experiments on physical phantom samples under circular measurement geometry. The reconstructed images calculated by the back-projection method agree with the original ones very well. Results indicate that this technique using reconstruction theory is a powerful imaging method that results in good contrast and good spatial resolution (0.5 mm).

Finally, we have conducted a preliminary study of breast cancer detection. Four excised breast specimens have been tested. The tumor regions have been clearly located. This initial study shows that the RF-induced photoacoustic tomography has great potential in the application of breast cancer detection.

## CHAPTER VI

### SUMMARY AND CONCLUSIONS

PAT is based on the generation of acoustic waves by safe deposition of electromagnetic energy, such as light and radio-frequency wave, into biological tissues. Computer-based PAT is a novel imaging modality, which uses all the PA signals measured by unfocused small-aperture ultrasound detectors at various locations on a surface that encloses the sample under study. This technology combines the advantages of electromagnetic absorption contrast and ultrasonic resolution.

We have developed time-domain reconstruction algorithms for PAT. For three common measurement geometries, including spherical, planar, and cylindrical surfaces, we have derived a universal exact time-domain back-projection reconstruction formula, which is computed with temporal back projections and coherent summations over spherical surfaces using a solid-angle factor weighting the contributions to the reconstructions from the detection elements at different locations. This back-projection formula can be straightforwardly extended to the limited-angle view case, in which the reconstruction may be incomplete and reconstruction artifacts may occur. The solid-angle weighting factor, however, can compensate for the variations in the detection views. In addition, this back-projection formula can be extended to general geometry with good approximation in the detection of small (compared with the measurement geometry) but deeply buried objects.

We have investigated the spatial resolution of PAT. It is found that the point-spread function as a function of bandwidth is space-invariant for any measurement geometry when the reconstruction is linear and exact. The obtainable spatial resolution is actually diffraction-limited by the photoacoustic waves. We also have demonstrated that the finite aperture of the detector extends the point-spread function for different geometries. The detector aperture blurs lateral resolution greatly at different levels for different geometries but the effect on axial resolution is slight. The results offer clear instruction for designing appropriate photoacoustic imaging systems with predefined spatial resolution.

We have studied the optimal sampling strategy of PAT for three common measurement geometries. According to the sampling theorem, the discrete spatial sampling period must be slightly smaller than half of the diameter of the sensing aperture of the detector; otherwise, significant aliasing artifacts may be introduced in the measurement and reconstruction. However, it is not necessary to let the sampling period be much smaller, since smaller sampling periods increase tremendously the number of the detection positions but do not provide significant improvement in image quality.

We have built a prototype of RF-induced PAT system. Phantom experiments have demonstrated PAT is a powerful imaging method that results in good contrast and good spatial resolution ( $\sim 0.5$  mm with  $0.3 \mu\text{s}$  pulse duration). Actually, the spatial resolution is scalable with ultrasound frequency. We also have conducted a preliminary study of breast imaging. This initial study shows that the RF-induced photoacoustic tomography has great potential in the application of breast cancer detection.

## REFERENCES

- [1] A. G. Bell, Am. J. Sci. **20**, 305 (1880).
- [2] C. K. N. Patel and A. C. Tam, Rev. Mod. Phys. **53**, 517 (1981).
- [3] G. A. West, J. J. Barrett, D. R. Siebert, and K. V. Reddym, Rev. Sci. Instrum. **54**, 797 (1983).
- [4] D. A. Hutchins and A. C. Tam, IEEE Trans. Ultrason. Ferroelectr. Freq. Control. **33**, 429 (1986).
- [5] A. C. Tam, Rev. Mod. Phys. **58**, 381 (1986).
- [6] M. W. Sigrist, J. Appl. Phys. **60**, R83 (1986).
- [7] A. Rosencwaig, *Photoacoustics and Photoacoustic Spectroscopy* (Wiley, New York, 1980).
- [8] V. P. Zharov, V. S. Letokhov, *Laser Optoacoustic Spectroscopy*, Springer Series in Optical Science, Vol. **37** (Springer-Verlag, New York, 1986).
- [9] *Principles and Perspectives of Photothermal and Photoacoustic Phenomena*, edited by A. Mandelis (Elsevier Science, New York, 1992).
- [10] K. H. Michaelian, *Photoacoustic Infrared Spectroscopy* (Wiley-Interscience, Hoboken, New Jersey, 2003).
- [11] J. F. McClelland, R. W. Jones, and S. J. Bajic, *FT-IR Photoacoustic Spectroscopy*, in *Handbook of Vibrational Spectroscopy*, edited by J. M. Chalmers and P. R. Griffiths (John Wiley & Sons, New York, 2002).
- [12] V. E. Gusev and A. A. Karabutov, *Laser Optoacoustics* (AIP, New York, 1993).



- [13] *Biomedical Optoacoustics*, edited by A. A. Oraevsky, Proc. SPIE **3916** (SPIE, Bellingham, Washington, 2000).
- [14] *Biomedical Optoacoustics II*, edited by A. A. Oraevsky, Proc. SPIE **4256** (SPIE, Bellingham, Washington, 2001).
- [15] *Biomedical Optoacoustics III*, edited by A. A. Oraevsky, Proc. SPIE **4618** (SPIE, Bellingham, Washington, 2002).
- [16] *Biomedical Optoacoustic IV*, edited by A. A. Oraevsky, Proc. SPIE **4960** (SPIE, Bellingham, Washington, 2003).
- [17] F. A. Duck, *Physical Properties of Tissue* (Academic, London, 1990).
- [18] W. F. Cheong, S. A. Prahl and A. J. Welch, IEEE J. Quantum Elect. **26**, 2166 (1990).
- [19] L. E. Larsen and J. H. Jacobi, *Medical Applications of Microwave Imaging* (IEEE, New York, 1986).
- [20] P. M. Meaney, M. W. Fanning, D. Li, S. P. Poplack and K. D. Paulsen, IEEE Trans. Microwave Theory Tech. **48**, 1841 (2000).
- [21] P. N. T. Wells, Rep. Prog. Phy. **62**, 671 (1999).
- [22] G. J. Diebold, T. Sun, and M. I. Khan, Phys. Rev. Lett. **67**, 3384 (1991).
- [23] J. D. Jackson, *Classical Electrodynamics*, 2nd ed. (John Wiley & Sons, New York, 1999).

- [24] G. B. Arfken and H. J. Weber, *Mathematical Methods for Physicists*, 4th ed. (Academic, San Diego, California, 1995).
- [25] P. M. Morse and H. Feshbach, *Methods of Theoretical Physics* (McGraw-Hill, New York, 1953).
- [26] P. M. Morse and K. U. Ingard, *Theoretical Acoustics* (McGraw-Hill, New York, 1968).
- [27] V. E. Gusev, and A. A. Karabutov, *Laser Optoacoustics* (AIP, New York, 1993).
- [28] C. C. Johnson and A. W. Guy, Proc. IEEE **60**, 692 (1972).
- [29] K. R. Foster, IEEE Trans. Plasma Sci. **28**, 15 (2000).
- [30] The Institute of Electrical and Electronics Engineers, *IEEE Standard for Safety Levels with Respect to Human Exposure to Radio Frequency Electromagnetic Fields, 3kHz to 300 GHz: IEEE Std C95.1* (IEEE, Inc., New York, 1999).
- [31] The American National Standards Institute, *American National Standard for the Safe Use of Lasers in Health Care Facilities: Standard Z136.1-2000* (ANSI, Inc., New York, 2000).
- [32] R. A. Kruger, and P. Liu, Med. Phys. **21**, 1179 (1994).
- [33] G. Ku, and L.-H. Wang, Med. Phys. **27**, 1195 (2000).
- [34] G. Ku and L.-H. Wang, Med. Phys. **28**, 4 (2001).
- [35] M.-H. Xu, G. Ku, and L.-H. Wang, Med. Phys. **28**, 1958 (2001).
- [36] R. A. Kruger, P. Liu, Y. R. Fang and C. R. Appledorn, Med. Phys. **22**, 1605 (1995).

- [37] R. Y. Fang, R. A. Kruger, C. R. Appledorn, and P. Liu, Prog. Nat. Sci. **S6**, S-598 (1996).
- [38] R. A. Kruger, D. R. Reinecke and G. A. Kruger, Med. Phys. **26**, 1832 (1999).
- [39] P. Liu, Phys. Med. Biol. **43**, 667 (1998).
- [40] C. G. A. Hoelen and F. F. M. de Mul, Appt. Opt. **39**, 5872 (2000).
- [41] C. G. A. Hoelen, F. F. M. de Mul, R. Pongers and A. Dekker, Opt. Lett. **23**, 648 (1998).
- [42] K. P. Köstli, M. Frenz, H. P. Weber, G. Paltauf, and H. Schmidt-Kloiber, Appl. Opt. **40**, 3800 (2001).
- [43] G. Paltauf, J. A. Viator, S. A. Prahl and S. L. Jacques, J. Acoust. Soc. Am. **112**, 1536 (2002).
- [44] Y. V. Zhulina, Appl. Opt. **39**, 5971 (2000).
- [45] M.-H. Xu and L.-H. Wang, IEEE Trans. Med. Imaging **21**, 814 (2002).
- [46] Y. Xu, M.-H. Xu and L.-H. Wang, IEEE Trans. Med. Imaging **21**, 829 (2002).
- [47] Y. Xu, D. Feng, and L.-H. Wang, IEEE Trans. Med. Imaging **21**, 823 (2002).
- [48] K. P. Köstli, D. Frauchiger, J. J. Niederhauser, G. Paltauf, H. P. Weber and M. Frenz, IEEE J. Sel. Top. Quant. Electron. **7**, 918 (2001).
- [49] K. P. Köstli, M. Frenz, H. Bebie, and H. P. Weber, Phys. Med. Biol. **46**, 1863 (2001).
- [50] M.-H. Xu, Y. Xu and L.-H. V. Wang, IEEE Trans. Bio.-Med. Eng. **50**, 1086 (2003).

- [51] M.-H. Xu and L.-H. V. Wang, unpublished (2003).
- [52] R. A. Kruger, P. Liu, Y. R. Fang and C. R. Appledorn, *Med. Phys.* **22**, 1605 (1995).
- [53] R. Y. Fang, R. A. Kruger, C. R. Appledorn, and P. Liu, *Prog. Nat. Sci.* **S6**, S-598 (1996).
- [54] R. A. Kruger, D. R. Reinecke and G. A. Kruger, *Med. Phys.* **26**, 1832 (1999).
- [55] R. A. Kruger, K. K. Kopecky, A. M. Aisen, D. R. Reinecke, G. A. Kruger, and W. L. Kiser Jr, *Radiology* **211**, 275 (1999).
- [56] R. A. Kruger, K. D. Miller, H. E. Reynolds, W. L. Kiser Jr, D. R. Reinecke, and G. A. Kruger, *Radiology* **216**, 279 (2000).
- [57] R. A. Kruger, K. M. Stantz, and W. L. Kiser Jr, *Proc. SPIE* **4682**, 521 (2002).
- [58] R. A. Kruger, W. L. Kiser Jr, D. R. Reinecke and G. A. Kruger, *Med. Phys.* **30**, 856 (2003).
- [59] R. A. Kruger, W. L. Kiser Jr, D. R. Reinecke , G. A. Kruger, and K. D. Miller, *Mol. Imaging* **2**, 113 (2003).
- [60] A. A. Karabutov, E. V. Savateeva, and A. A. Oraevsky, *Laser Phys.* **13**, 711 (2003).
- [61] R. O. Esenaliev, A. A. Karabutov, and A. A. Oraevsky, *IEEE J. Sel. Top. Quant. Electron.* **5**, 981 (1999).
- [62] A. A. Oraevsky, A. A. Karabutov, S. V. Solomatin, E. V. Savateeva, V. G. Andreev, Z. Gatalica, H. Singh, and R. D. Fleming, *Proc. SPIE* **4256**, 6 (2001).
- [63] M.-H. Xu and L.-H. V. Wang, *Med. Phys.* **29**, 1661(2002).

- [64] D. Feng, Y. Xu, G. Ku, and L.-H. Wang, *Med. Phys.* **28**, 2427 (2001).
- [65] X. Wang, Y. Xu, M. Xu, S. Yokoo, E. S. Fry, and L.-H. Wang, *Med. Phys.* **29**, 2799 (2002).
- [66] X. Wang, Y.-J. Pang, G. Ku, X.-Y. Xie, G. Stoica and L.-H. V. Wang, *Nature Biotech.* **21**, 803 (2003).
- [67] X. Wang, Y. Pang, G. Ku, G. Stoica and L.-H. V. Wang, *Opt. Lett.* **28**, 1739(2003).
- [68] G. Paltauf, H. Schmidt-Kloiber, K. P. Köstli, and M. Frenz, *Appl. Phys. Lett.* **75**, 1048 (1999).
- [69] K. P. Köstli, M. Frenz, H. P. Weber, G. Paltauf, and H. Schmidt-Kloiber, *Appl. Opt.* **40**, 3800 (2001)
- [70] J. J. Niederhauser, D. Frauchiger D, H. P. Weber, and M. Frenz, *Appl. Phys. Lett.* **81**, 571 (2002).
- [71] K. P. Köstli, D. Frauchiger, J. J. Niederhauser, G. Paltauf, H. P. Weber and M. Frenz, *IEEE J. Sel. Top. Quant. Electron.* **7**, 918 (2001).
- [72] K. P. Köstli and P. C. Beard, *Appl. Opt.* **42**, 1899 (2003).
- [73] P. C. Beard and T. N. Mills, *Proc. SPIE* **4256**, 34 (2001).
- [74] A. Kharine, S. Manohar, R. Seeton, R. G. M. Kolkman, R. A. Bolt, W. Steenbergen, and F. F. M. de Mul, *Phys. Med. Biol.* **48**, 357 (2003).
- [75] M.-H. Xu and L.-H. V. Wang, *Phys. Rev. E* **67**, 056605 (1-15) (2003).
- [76] D. Finch, S. K. Patch, and Rakesh, *SIAM J. Math. Anal.* **35**, 1213 (2003).

- [77] Y. Xu and L.-H. Wang, IEEE Trans. Ultrason. Ferroelectr. Freq. Control **50**, 1134 (2003).
- [78] Y. Xu, L.-H. V. Wang, G. Ambartsoumian, and P. Kuchment, Med. Phys. **31**, 724 (2004).
- [79] M. Abramowitz and I. A. Stegun, *Handbook of Mathematical Functions with Formulas, Graphs, and Mathematical Tables* (Dover Publications, New York, 1965).
- [80] *Handbook of Medical Imaging*, edited by J. Beutel, H. Kundel, and R. Metter (SPIE Press, Washington, D.C., 2000).
- [81] H. Stark, J. Woods, J. Opt. Soc. Am. **69**, 1519 (1979).
- [82] H. Stark, J. Woods, I. Paul, and R Hingorani, IEEE. Trans. Signal Process. **29**, 237 (1981).
- [83] G. Goertzel and N. Tralli, *Some Mathematical Methods of Physics* (McGraw-Hill, New York, 1960).
- [84] R. T. Greenlee, M. B. Hill-Harmon, T. Murray, and M. Thun, CA Cancer J. Clin. **51**, 15 (2001).
- [85] S. S. Chaudhary, R. K. Mishra, Arvind Swarup & Joy M. Thomas, Indian Journal of Biochemistry & Biophysics **21**, 76 (1984).
- [86] Curtis C. Johnson, Arthur W. Guy, Proceedings of the IEEE **60**, 692(1972).
- [87] K. R. Foster, J. L. Schepps, Journal of Microwave Power **16**, 107(1981).

- [88] *The Physiopathology of Cancer*, edited by F. Homburger and W. H. Fishman  
(Hoeber-Harper, New York, 1953).

## **VITA**

Minghua Xu received his Ph.D. in Acoustics from Nanjing University (China) in December 1999. He later researched under Dr. Lihong V. Wang of Texas A&M University in the fall of 2000. The research focused on the development of Photoacoustic Tomography for the biological samples. He received his Ph.D. in Biomedical Engineering in August 2004.

C/O Minghua Xu

233 Zachry Engineering Center

TAMU 3120

College Station, TX 77843-3120